AN INTEGRATED GRAVITY, MAGNETIC AND SEISMIC INTERPRETATION OF THE CARBONIFEROUS BAY ST. GEORGE SUBBASIN, WESTERN NEWFOUNDLAND

GERALD JOSEPH KILFOIL

An Integrated Gravity, Magnetic and Seismic Interpretation of the Carboniferous Bay St. George Subbasin, Western Newfoundland

by

Gerald Joseph Kilfoil

A thesis submitted to the School of Graduate Studies
in partial fulfillment of the requirements
for the degree of
Master of Science

Department of Earth Sciences
Memorial University of Newfoundland
October 1988

St. John's, Newfoundland

Abstract

Gravity, magnetic and reflection seismic data were compiled and interpreted to determine the basement and internal structure in the Carboniferous Bay St. George Subbasin of Western Newfoundland. Gravity data, compiled from portions of several datasets for onshore regions, were complemented by those from a recent underwater gravimetry survey of St. George's Bay. Magnetic data from published aeromagnetic maps, a private aeromagnetic survey and a sea magnetometer survey were integrated into a single data set by application of corrections and offsets to bring each to a similar datum. Reflection seismic data of 1971 and 1973 vintage cover an area of the outer St. George's Bay.

The geophysical interpretation strongly supports the hypothesis of a subbasin opened by northeast-directed right-lateral wrench tectonics. In addition, less prominent structural features are discussed in the text and a basement structure map is produced. Evidence in support of structure within the sedimentary section is also discussed.

Sedimentation in the early history of the subbasin was controlled by vertical displacements along the northeast directed strike-slip faulting of the Cabot Fault system that initiated the basin opening during Famenian time. The Long Range Fault, which borders the subbasin to the southeast, is readily identified from the contoured datasets

by its strong geophysical signature. A fault identified as trending northeast along the southeast St. George's Bay coastline exhibits a similar but less prominent geophysical character. The latter fault bounded the early subbasin on its northwest margin during deposition of the Anguille Group.

North-northeast oriented faults, which are associated with vertical displacement of Lower Paleozoic rocks on the Port au Port Peninsula, are extrapolated offshore on the basis of a series of magnetic highs whose maxima define an east-west trend south of the peninsula's southern coastline.

Basement picks on the reflection profiles delimit the offshore subbasin as a half-graben dipping monoclinally to the southeast and interrupted locally by strike-slip faults. Gentle gravity gradients to the southeast attest to the agreement of datasets and enable depth mapping in the inner reaches of the bay. Results of the present interpretation show the subbasin as transected by several east-west dextral strike slip faults spaced on the order of 10 km, and laterally displacing features resulting from the earlier faulting by distances of the order of 5 km. Vertical displacements along these faults is minimal with the single exception of a fault at 5365N (UTM km) where a northward throw of greater than 2.0 km has been identified from offsets in the basement seismic reflector. Timing of secondary faulting is uncertain, but is considered to largely post-date deposition of the Missippian-aged Codroy Group, with possibilities of initiation as early as the Mississippian/Pennsylvanian time boundary.

Gravity and magnetic data profiles, selected where best constrained by the seismic interpretation and geology, were modelled using available physical parameters and developed modelling techniques to obtain estimates of depth to basement, configurations of major lithologic units and the extent of large evaporite structures within the Carboniferous strata.

Table of Contents

List of Figures

List of Tables

1. Introduction

The present project was undertaken as part of a multi-disciplinary study to define the structure and extent of Carboniferous sedimentary rocks in Newfoundland. The aim of this study is to interpret recently acquired geophysical data over the Bay St. George Subbasin within the framework of existing geological constraints.

The Bay St. George subbasin has been the target of several small localized geophysical surveys over the past thirty years. Results of an early gravity study of the St. George's Bay lowlands onshore were reported by Verrall (1954). Data were collected along traverses extending inland from the coast along accessible roads and river cuts, so tend to be irregularly spaced, with large data gaps. These data were reduced to an arbitrary reference but show the variability and local steep gradients observed in the present study. Aeromagnetic surveys were flown over the onshore region during the late 1950's and early 1960's. The inner portion of St. George's Bay was covered by an aeromagnetic survey during 1969 by Lockwood Geophysical Services. The results of this survey are reported and interpreted in Spector (1969).

Peavy (1985) presents the interpretation of gravity and magnetic data for an onshore portion of the Bay St. George Subbasin. Data used in his study are incorporated in data sets included in the present study in which the emphasis is placed on the interpretation of geophysical data for the portion of the subbasin which underlies St.

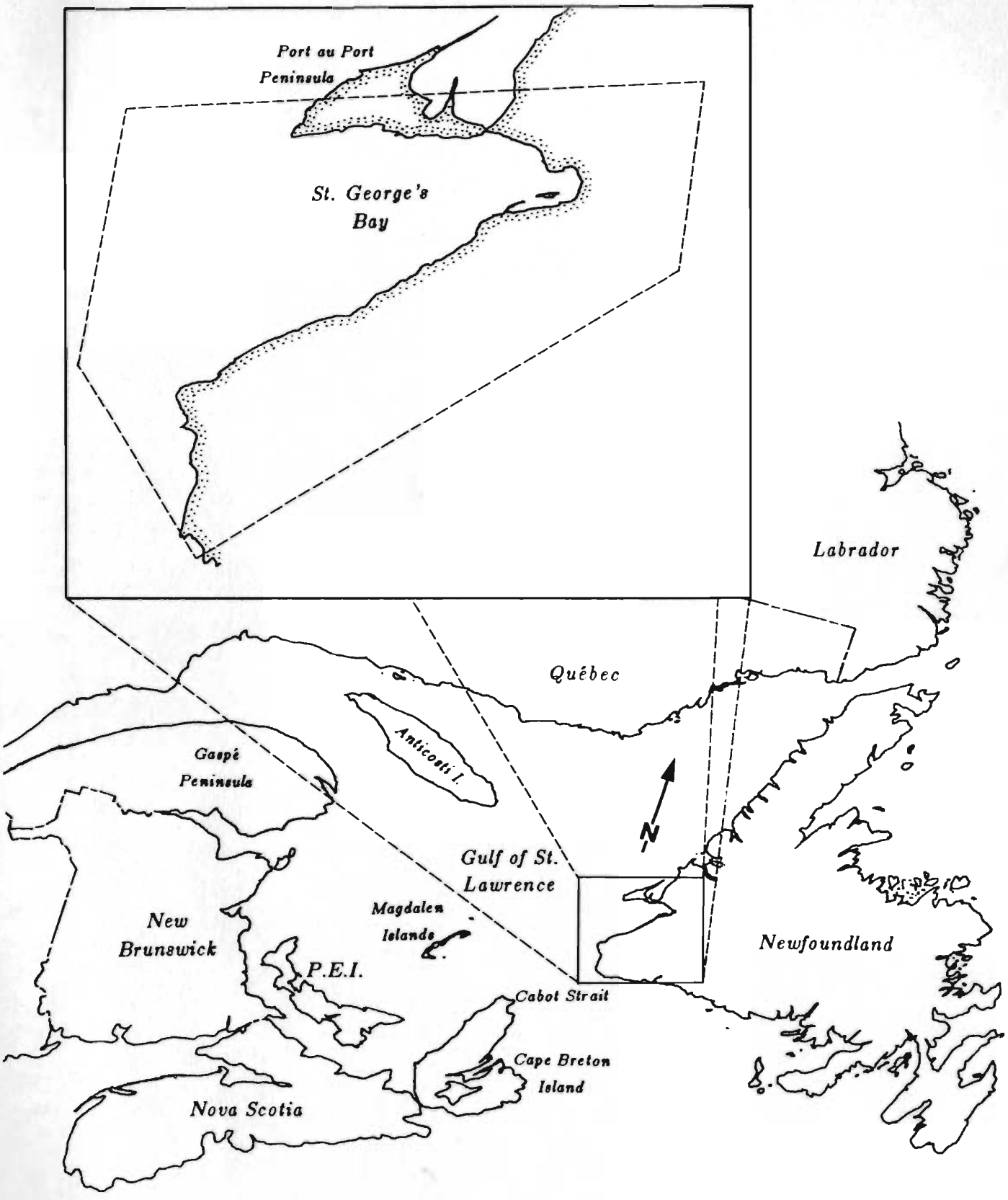

Figure 1.1. Location map with expanded view of the Bay St. George Subbasin within the Atlantic Provinces. The dashed lines of upper diagram define the approximate boundaries of the present area of study.

George's Bay and extends westward beyond the Port au Port Peninsula, as this area has received little prior attention.

The Bay St. George subbasin forms the eastern portion of the larger Maritimes Basin (Bradley, 1980) which extends from southern New Brunswick to Newfoundland in length, and covers the southern Gulf of St. Lawrence, P.E.I., parts of mainland Nova Scotia and most of Cape Breton Island along its breadth (see Figure 1.1). The Maritimes Basin is divided into several elongate subbasins each having received thick sediment deposits during Carboniferous time and each separated from adjacent subbasins by regions of shallower basement or ridges, the latter having accumulated only a thin veneer of sediments with basement exposures locally. Other exposures of Carboniferous sediment in Newfoundland are found in the Deer Lake and White Bay subbasins located to the northeast.

The geology for the onshore portion of the subbasin has been mapped and is compiled in a report by Knight (1983), which defines the lateral extent of Carboniferous sediments onshore. Geophysical interpretation of Peavy (1985) has placed constraints on the vertical extent of sediments for the onshore region. However, little is known of the structure and extent of Carboniferous aged rocks in the subbasin offshore.

Gravity and magnetic data covering the entire subbasin onshore and offshore were compiled from several sources. Compiled datasets extend beyond the known basin margins onshore. Available seismic data for an area offshore were interpreted and used to constrain the modelling and guide the interpretation of the potential field datasets.

Gravity data covering the entire subbasin onshore and adjacent areas were collected by personnel from Memorial University during 1983 and 1984 field seasons. Underwater gravity data were collected for the offshore portion of the subbasin by personnel from the Atlantic Geoscience Center, Earth Physics Branch and Memorial

University aboard the CSS Dawson in 1984. These data were augmented by data points from a regional survey of Weaver (1967) and the Trans Canada Highway survey of Weir (1971). Gravity stations were spaced, on average, 4 to 5 km apart for regions onshore, whereas a 6 km grid spacing was used in offshore regions. Magnetic data were digitized from published Geological Survey of Canada 1:63360 aeromagnetic maps for areas onshore. Magnetic anomalies were obtained by filtering and removal of the IGRF background field. Offshore, magnetic data were compiled from two sources. The first consists of sea magnetometer data recorded by Bedford Institute, Dartmouth, aboard two cruises of the CSS Hudson during 1968 and 1969, over the area which lies west of the Port au Port Peninsula. Total field and IGRF-removed magnetic anomaly values as well as spatial and temporal data were made available by Bedford Institute in digital tape format. The inner portion of St. George's Bay was covered by an aeromagnetic survey conducted by British Newfoundland Exploration Company, Ltd. in 1969. Contours of the regional field were digitized from maps of the project report (Spector, 1969) and included here. Seismic data covering the central offshore region obtained by Mobil Oil in 1971 and 1973 were made available courtesy of BP Canada in the form of prepared seismic sections. Potential field data were enhanced by regional-residual separation using trend-surface analysis.

Physical parameters for the various lithologic units, such as average rock densities and magnetic susceptibilities, were largely extracted from Peavy (1985) and other literature sources. Density estimates for two sedimentary units not included in the study by Peavy (1985) were determined in the present study.

Computer programs were developed to perform least-squares inversion of gravity and magnetic anomaly values, and extensively tested on synthetic data. Inverse programs were used in conjunction with forward modelling techniques to obtain estimates of

depth to basement and subsurface structure, as well as improved estimates of physical parameters. Programs were written in FORTRAN and make use of the IMSL subroutine package. All data reduction, map preparation and computer modelling were carried out under VMS operating system on a VAX 11/780 computer and support facilities at Memorial University of Newfoundland.

The geophysical interpretation strongly favours the hypothesis of a subbasin opened by northeast-directed right-lateral wrench tectonics, and subsequently reconfigured by a series of east-west strike slip displacements. The less prominent structural features which result from the later movements are delineated from the potential field and seismic datasets and used to produce a map of basement structure. Several large anticlinal structures are evident within the Mississippian sediments filling the half-graben of the subbasin offshore. The coincidence of large amplitude gravity lows with the characteristic strong intra-sediment seismic reflectors indicates that these anticlines are cored by evaporites.

2. Geology

The Bay St. George subbasin is the landward continuation in Newfoundland of the Maritimes Carboniferous Basin. The Maritimes Basin formed as a pull-apart basin in the dextral strike-slip régime of the post-Acadian Cabot Fault system (Bradley, 1982), expressed in Newfoundland as the Long Range Fault. Mapped surface boundaries of lithologic units within the subbasin (after Knight, 1982) and of immediately adjacent areas (Williams, 1985) are shown on Map 1 (see appended map holder).

2.1. Sedimentary Rocks

Late Devonian and Carboniferous sediments comprising the subbasin fill have been recognized by Knight (1983) and previous workers to overlie Precambrian basement. These are subdivided into three groups each distinguishable by its character and mode of deposition. For a detailed account of the Carboniferous stratigraphy, proposed depositional and tectonic history and economic potential, the reader is referred to Knight (1983). A brief summary of lithologies, estimated thicknesses and age correlations of stratigraphic units are provided here as Table 2.1 for quick reference. The three Carboniferous sediment groups are:

Anguille Group (Late Devonian to Early Mississippian) comprised of nonmarine sequences of siliciclastics: mostly red to grey fluvial and deltaic shales to coarse sandstones with conglomerates locally.

Codroy Group (Upper Mississippian) comprised of both marine and nonmarine sequences of siliciclastics, evaporites and calcareous sediments.

Barachois Group (Lower Pennsylvanian) comprised of red to grey siltstone-sandstone sequences of fluvial origin with minor mudstones and coals.

The next three sections discuss each of the Carboniferous sediment groups in

List of Abbreviations			
cg - conglomerate	ls - limestone	peb - pebbly(es)	c - coarse
ss - sandstone	dol - dolomite(ic)	mic - micaceous	rd - red
slst - siltstone	evap - evaporites	ark - arkosic	gn - green
sh - shale	gyp - gypsum	arg - argillaceous	gy - grey
mdst - mudstone	anh - anhydrite	fluv - fluvial	brn - brown
lut - lutite	hal - halite	x-b - cross bedded	bk - black
carb - carbonate	pot - potash salts	plan - planar	seq - sequence(s)
	clch - caliche	lam - laminated	

Table 2.1 (opposite page). Summary of Carboniferous rock units by lithology, approximate thickness and age (after Knight, 1983). Abbreviations used as lithologic descriptors are tabulated above.

Table 2.1
Carboniferous Rocks of Bay St. George Subbasin
(from Knight, 1983)

Group/Unit	Lithology	Thickness (m)	Age	
Barachois Group Undivided Barachois	gy peb ss; gy-bk mdst, sh, coal.	1500-1600	Westphalian (Pennsylvanian)	
Searston Fm.	rd slst; gn-rd peb ss; minor bk sh, mdst; minor brn cg.	2500	Namurian	
Codroy Group Robinson's Rv. Fm. -Overfall Brook Member	rd-brn massive to x-b ark to arg ss; minor cg, slst, mdst.	>345	Viséan	Mississippian
-Mollichignick Member	rd slst, mic ss, ark to arg peb ss near margins; coarse up seqs; marine carb near middle.	2275		
-Highlands Member	rd-gy ss to slst; cg to N and E; fining up seqs; x-b and plan ss; minor clch, lam ls.	1000-1400 884 onshore		
-Jefferies Village Member	rd-gy sh, mdst, slst, ss, minor cg interbed with carb and evap: gyp, anh, hal, pot; coarsens up near top.	1400-2000		
Codroy Road Fm.	rd slst to ss, lam ss; near top gy sh, evap: gyp, anh; minor carb and gy-bk slst.	120-300		
Ship Cove Fm.	lam ls; minor gyp nodules, rd-gy sh, mdst.	18-20		
Anguille Group Spout Falls Fm.	rd-gy fluv ss, slst, calc-ark-mic ss; well bedded; minor cg near margins.	780-2250	Tournaisian	
Friars Cove Fm.	cg to c ss; gy ss-cg-sh; x-b c ss at top; minor thick bk sh seqs; ss peb of Cam-Ord origin.	500-1300		
Snakes Bight Fm.	bk lut, gy ss, sh; thin slst to thick ark ss (flysch); minor dol, mdst, concretions.	785-1000		
Kennels Brook Fm.	gn-gy peb ss to cg; rd ss to rd-gn slate; fining up seqs; minor brn mdst, ls.	>3200	Famennian (Devonian)	

greater detail following mainly the interpretation of Knight (1983).

2.1.1. Anguille Group

The Anguille Group, oldest and thickest of the relatively undeformed Carboniferous sediment units, is exposed in an anticlinal structure and largely confined to a narrow basin in Southwest Newfoundland (Belt, 1968), which probably opened slightly later than, and as an eastward extension of subbasins to the west within the Maritimes Basin (Bradley, 1982). Knight (1983) interprets sedimentation in the Anguille Group as occurring in a deep lake within a narrow, elongate, fault-bounded, primitive subbasin with present outcrop suggesting maximum dimensions of 30 by 100 km. Sedimentary infill was derived primarily from uplands to the southeast of the early manifestations of Long Range Fault. A northeast trending marginal fault to the northwest, parallel to the Snakes Bight Fault onshore (see Map 1), is assumed to now lie concealed beneath Codroy strata in the St. George's Bay offshore. The early subbasin is also believed to have been fault bounded to the northeast by a fault trending east along the northern extent of Anguille Group outcrop (Belt, 1969), oblique to the two marginal faults. Although the early subbasin may be envisioned as a graben type feature, its evolution is complicated by right lateral strike-slip movements along the faults defining its margins to the southeast and northwest. The bulk of strike slip displacement along the Long Range Fault system is interpreted as syn-depositional with the Anguille Group. Knight (1983) describes the 120 km of interpreted right lateral displacement along the system to have been divided into two pulses resulting in distinct phases of basin pull-apart during deposition of the Anguille Group. The earlier basin was confined to the south of present outcrop and was filled with coarse sediments of Famenian age. The second phase of northward basin extension resulted in deposition of thick upper Anguille Group strata during Tournaisian time.

The basal Late Devonian Kennels Brook Formation consists of a thick fluvial molasse: redbeds with minor lacustrine sediments that may have extended beyond the margins of the early subbasin. These arkosic strata are correlated with similar pre-Horton strata in other parts of the Maritimes Basin. The thickness of the Kennels Brook unit and the underlying basement rock type are unknown since the basal contact is nowhere exposed in the Anguille region. A drill hole sited near the hinge of the Anguille anticline penetrated 2200 m entirely within the unit. The top of the Kennels Brook Formation is marked by the onset of lacustrine sedimentation. The conformable overlying Snakes Bight Formation is comprised of deep water sequences characterized by turbidites and alluvial fans shallowing to basinal muds. The Friars Cove Formation strata reveal a shallow fluvial environment of grey delta sands and extensive marsh sediments. The overlying thick, sand-dominated alluvial plain redbeds of the Spout Falls Formation were restricted to the northerly parts of the early subbasin while lacustrine conditions persisted in the southern portion. Such distribution of sedimentary facies would indicate a shift of the depocenter from southwest to northeast as a result of a second pulse of basin opening and northward extension (Knight, 1983). The later basinal extension is manifested by deposition of the Friars Cove and Spout Falls Formations. An interfingering of these two formations in the southwest of the basin suggests that they are diachronous and possibly lateral equivalents.

In addition to clasts of basement rocks, Friars Cove and Spout Falls Formations contain carbonate detritus, which correlates with Early Paleozoic rocks exposed on the Port au Port Peninsula, that was derived from uplifting and retreating Humber Arm Allochthon highlands to the northwest. By Late Anguille time, the front of northwest highlands had retreated to near its present position just south of the Port au Port. Latest Anguille deposition of the Spout Falls Formation overstepped the early basin

margins, blanketing the denuded Grenville basement to the north and west with a relatively thin (150-200 m) veneer of redbeds (I. Knight, per. comm. 1986). Anguille age fanglomerates containing detritus derived from highlands to the north exist locally along the northern and eastern margins of the present subbasin.

2.1.2. Codroy Group

The Codroy Group is correlated with and closely resembles the Windsor Group of Nova Scotia and similarly reflects both marine and nonmarine depositional environments. Clastic sedimentation in the Codroy is not unlike that of the latest Anguille except for the marine rather than terrestial environment of deposition (Bradley, 1982), as Codroy age fine marine facies grade laterally into similar fanglomerates near basin margins (Belt, 1968). Well cemented and highly competent Anguille sediments contrast with less competent Codroy evaporite sequences. Codroy strata were deposited over a much wider area than the narrow Anguille basin.

A widespread shallow marine transgression marks the lower boundary of the Codroy Group which overstepped the Anguille basin margins with unconformable to locally conformable deposition of laminated limestone of the Ship Cove Formation. The presence of extremely fine limestone lamina, correlatable over large areas, and the blue-green algal mats in the Ship Cove Formation indicate a subtidal to intertidal environment of very shallow, quiet hypersaline waters and low sedimentation rates (Geldsetzer, 1978). Biohermal buildups were confined to local basement highs where surface waters were of near-normal salinities. In the Bay St. George subbasin the Windsor Sea transgressed from north to south over intertidal flats (Knight, 1983).

The overlying Codroy Road Formation consists of a marine sequence of basal grey shales and siltstones, grading upwards into limestones and evaporites intercalated with fluvial redbeds. The depositional environment for the Codroy Road Formation was

shallow marine with limited biohermal buildup and increasing hypersalinity. Marine conditions dominated the south central subbasin region while a sabkha environment prevailed to the north. Alluvial plains flanked the subbasin to the south adjacent to the Long Range Fault. Thick evaporite sequences developed in subsiding paleotopographic lows or sinks, separated from circulating sea waters by basement or anhydrite arches.

Upsection, the Jefferies Village Member of the Robinsons River Formation records a change to normal marine salinities with increasing deposition of nonmarine siliciclastics and limestones, indicating increased subsidence rates (Geldsetzer, 1978). A second marine transgression produced an open shelf environment. This was followed by marine regression and deposition of alluvial fans near basin margins and fine redbeds along meandering rivers of westward paleoflow. The upper Jefferies Village Member is composed of coarsening upward sequences. This suggests uplift of source areas as revealed in sediments of the overlying Highlands Member. Several brief marine incursions are recorded in the strata of the Upper Codroy Group. Above the Highlands Member, sediments of the Mollichignick Member indicate a return to a stable floodplain environment. Subsequent coarsening upwards to the alluvial fans of the Overfall Brook Member indicates relative uplift of source areas and steepening of river gradients. These redbeds, overlying evaporites in the lower Codroy Group, thicken in local depressions formed by concurrently migrating evaporite sequences.

The sediments in the Lower Codroy Group record a tectonically inactive period of low subsidence rates and marine transgression, while those of the Upper Codroy Group indicate renewed tectonic activity and a return to dominantly clastic sedimentation. Detritus for the Codroy Group, as for the Anguille Group, was derived principally from highlands to the southeast, but with an increasing sediment proportion derived from uplifting highlands north of the subbasin, particularly in the northernmost reaches of the

subbasin.

2.1.3. Barachois Group

Strata of the Barachois Group indicate a persisting fluviatile environment with resulting red to grey and black fining upward sequences. Onshore, the Barachois Group consisting of the Searston Formation in the southwest Codroy Valley and the undivided Barachois Group situated northwest of the Anguille Mountains, with small outcrops near Stephenville, typify a meandering river system with associated floodplain deposits. Multistorey channel sandstone sequences, low channel sinuosity and lack of caliche deposits suggest a constant shifting of river channels over a stable floodplain. Relatively uniform deposition throughout the Searston Formation in the southeast onshore indicates a period of uninterrupted subsidence. Paleocurrent studies indicate an overall northwesterly flow direction away from highlands to the southeast. Grey to black silty mudstones and coal lenses are found in abandoned meander cut-offs and in local depressions adjacent to meandering streams, deposited during extended periods of stabilized river channels. These are associated with finer laminated redbeds characteristic of a swampy lowlands environment. Increasing presence of plant detritus and frequent flooding are diagnostic of a higher precipitation rate in source areas and a gradually higher humidity than the semi-arid conditions prevailing during deposition of the earlier Codroy and Anguille Groups. Coals and finer sediments become increasingly prominent in the Upper Barachois section and correlate with the lowermost dirty coals found in similar Carboniferous strata in New Brunswick and Nova Scotia. Thermal maturation indices place onshore Barachois sediments in the 85 to 135 °C temperature bracket, within the oil window (S. Soloman, per. comm. 1986). Thus, using reasonable values for geothermal gradients, which are likely quite high in close proximity to basin margins, a sediment overburden estimate of 2 to 4 km is interpreted (Soloman, 1986). As well, extrapolation

from compaction curves (Baldwin and Butler, 1985) using available density data for Barachois units (Peavy, 1985) indicates about 3 km of former sediment cover. Such data suggests that higher grade, more extensive coals were present among clastic sediments which originally were deposited above the present Barachois Group onshore but have since been uplifted and eroded, probably during the Alleghenian Orogeny. Compositional studies (Knight, 1983) show a source area for Barachois Group sediments correlating favourably with rocks now present southeast of the Long Range Fault adjacent to the two major areas of outcrop onshore. This concurs with earlier findings that little or no lateral displacement has occurred along the Long Range Fault since Late Carboniferous time (Sheridan and Drake, 1968; Wilson, 1962).

2.2. Evaporites

Evaporite sequences, notably gypsum, anhydrite and salt are present in several horizons of the marine-dominated Codroy Road and Robinsons River Formations. Outcrops of gypsum are found on the northern flanks of the Flat Bay and Anguille Anticlines onshore, but the relative structural complexity introduced by local folding and thrust faulting of units in the south renders only northern deposits as being economically viable. Gypsum occurs in four zones; the lower two are found near the base and top of the Codroy Road Formation, while the upper two are less well developed in the Jefferies Village Member of the Robinsons River Formation. A sizable deposit of gypsum from the lowermost horizon is mined at Flat Bay. Other large deposits occur in the Codroy Road strata in the northern onshore outcrop on the flanks of the Anguille Anticline. Outcrops of gypsum from the Jefferies Village Member with lesser thickness and thinly laminated dolomites are of subeconomic value. The Flat Bay deposit displays a transition with depth to anhydrite, indicating that near surface deposits are the result of hydration. Lateral gradation to salt deposits is suggested by minor halite-rich laminae

within gypsum deposits.

Salt sequences encountered in drilling negative gravity anomalies at St. Fintan's, Robinsons River and Fischells Brook were placed in the lower Jefferies Village Member, although possible flowage lends uncertainty to stratigraphic positioning (Knight, 1983). Drill holes have intersected salt rich layers 50 to 400 m thick with minor potassic rich horizons of carnallite and sylvite. The Robinsons River and St. Fintan's deposits are intercalated with clay, dolomite and anhydrite/gypsum rich bands, suggesting that these are bedded deposits which experienced little flowage history, and which have a lithology correlative to Windsor subzone A deposits elsewhere in the Maritimes Basin. The drill hole at St. Fintan's delineated a 120 m thick muddy salt section, while two sections of 184 m and 54 m salt thickness and separated by 100 m of salt-cut mud were identified in the Robinson's River drill hole (Knight, 1983). Intersection of thick nearly pure halite layers in drilling the Fischells Brook deposit suggests that flowage to a salt plug structure has occurred. This deposit contains in excess of 390 m of nearly pure halite, as evidenced by the fact that the hole was still in salt to this depth when drilling was terminated.

A potassic rich zone from 4.6 to 6.0 m thick with K_2O contents within the mineralized zone of up to 25% is reported to occur near the top of the Fischells Brook deposit (Knight, 1983). A similar style of mineralization occurs in economic potash zones within Windsor A age anticlinal structures in New Brunswick. However, the circular shape and restricted size of the associated gravity anomaly indicates that the Fischells Brook deposit is a diapiric structure of limited lateral extent.

2.3. Pre-Carboniferous Geology

The pre-Carboniferous basement in the Bay St. George subbasin is likely comprised of Precambrian age rocks of Williams' (1978) Humber Zone similar to those of the Indian

Head Complex, rather than a continuation of the relatively undeformed carbonate sequence of the Port au Port Peninsula offshore (Williams, per. comm. 1986). Cambrian rocks of the Degras Formation are found exposed along the south coast of the Port au Port (Williams. 1985) with gentle northwestward dips, such that a traverse southward into the offshore should encounter first a short section of the Kippens Formation followed by outcrop of the Indian Head Complex similar to that exposed in the Indian Head Range northeast of Stephenville (Williams, per. comm. 1986). Geologic trends and formation thicknesses measured onshore suggest that the carbonate rocks continue only a short distance offshore south of the Port au Port Peninsula. The southern limit of Early Paleozoic carbonates would be expected to continue its broad curvilinear trend toward the northwest to reappear onshore on the Gaspé Peninsula, Quebec (Williams, 1978). Knight (per. comm., 1986) interprets the basement to the immediate northwest of the onshore Anguille outcrop to have been reduced to a peneplane of Grenville rocks during the Tournaisian prior to deposition of the uppermost Anguille Group. In the hinge of the Flat Bay Anticline, conglomerates assigned to the Anguille Group rest unconformably on Indian Head basement (Knight, 1979). The Lower Paleozoic carbonate sequence should be thus limited in its southward extent (Williams; Knight, per. comm., 1986) in the Bay St. George subbasin, rather than underlying the Carboniferous as is postulated by Watts (1972) in interpretation of the East Magdalen Basin farther west.

Detrital correlations for early Anguille sediments indicate a partial contribution from Fleur de Lys Group rocks situated immediately to the northwest of the early subbasin at time of deposition. These rocks were transported northward (relative to the Anguille basin) dextrally 120 km along the coastal fault to their present location, northeast of Port au Port. Allochthonous rocks similar to those found in thrust sheets

to the north are considered (Williams, per. comm., 1986) as unlikely candidates for pre-Carboniferous basement rocks; rather the Bay St. George subbasin is largely underlain by Grenville basement of the Humber zone. However, considering the intense deformation experienced along the ancient promontory located east of Stephenville, the pre-Carboniferous basement geology is uncertain, particularly in the southeastern portion of the subbasin onshore (underlying Anguille sediments).

Onshore exposures of the Indian Head Complex reveal foliated dioritic to granodioritic gneisses in the northern Indian Head Range becoming more massive southward, east of Stephenville, with outcrops of anorthosites and layered gabbroic rocks, cut by foliated rocks of granitic composition (Williams, 1985). The northwestward trend of layers and foliations within these rocks contrasts sharply with the northeastward trend of unconformable Paleozoic rocks above and is considered to have been acquired during the Precambrian. Lenses and bands of magnetite occur within the foliated gabbros, and are the probable cause of variability in magnetic anomalies observed over the complex.

2.4. Structural Geology

Sediments in the subbasin were folded and faulted to their present configuration during the Late Pennsylvanian Hercynian Orogeny (Knight, 1983) by reactivation of northeast oriented strike-slip faults produced by earlier transpressional tectonics. Faults oriented northeast, subparallel to the Long Range Fault, show both a strike-slip and a (later) vertical displacement component. Minor northwest trending faults having little displacement developed as a conjugate to this principle fault set. A second prominent east-west fault set exhibits local displacements of northeasterly trending structures.

Northeast trends are evident in the orientation of two large doubly plunging folds, the Anguille and Flat Bay anticlines, and of the subparallel Barachois Synclinorium. St. David's Syncline, situated between the two major anticlines, exhibits a west-northwest

trend.

The Anguille Anticline is an asymmetrical fold, the hinge of which trends 030° and is dissected by the Snakes Bight Fault. The fault separates strata dipping from 40° NW to overturned on its northwest limb from beds dipping more gently to the southeast and folded in *en echelon* patterns in the southwest. Trends on these secondary folds intersect that of the anticline at a 30° angle. Near the northern extent of Anguille strata, the anticline is developed as an open fold. Here, the Snakes Bight Fault trends 068°. Dips on the northwest limb become steeper to the southwest, to overturned in the southwest corner of the onshore where thrust faulting has occurred locally.

Precambrian basement outcrops in the hinge of the Flat Bay Anticline. This structure differs from the Anguille Anticline, being a fairly open fold with beds steepening away from the hinge. Like the Anguille Anticline, however, the Flat Bay Anticline trends 037° and displays asymmetric character: beds steepen to 80° dip on its northwest limb.

The Barachois Synclinorium, situated to the southeast of the Flat Bay Anticline and to the west of the Long Range Fault, also shows a double plunge and an axial trend of 027°.

3. Data Sources/Manipulation

3.1. Gravity Data

Gravity data in the Bay St. George subbasin consist of those from an offshore underwater survey conducted during 1984 from the CSS Dawson, those from the areas onshore adjacent to St. George's Bay collected during the 1983 and 1984 summer field seasons and those from previously existing regional and highway surveys. Station locations from the various data sets are posted as Figure 3.1 for reference.

The positions of 73 gravity stations from a regional survey by Weaver (1967) were scaled from 1:500,000 maps. Estimation of horizontal and vertical positions are only of the expected accuracy of postings and elevation contours at the scale of these maps. The Weaver data were originally reduced using the the old Potsdam gravity reference system. Therefore, the Bouguer anomaly values for these stations were adjusted to be compatible with the present 1971 International Gravity Standardization Net (IGSN) (Morelli *et al.*, 1971) by adding an offset of -6.1 mGal (the average correction within the present study area) to their magnitudes as discussed in Appendix A-1. Some 245 gravity stations from Weir's (1971) Trans-Canada Highway survey traverse the basin roughly parallel to its strike. Corrections of -6.1 mGal were applied to a listing of Bouguer anomaly values from the Weir survey as above and these were incorporated into the data set along with their positional information. The Weir data were collected using a Sharpe gravimeter and are considered to have excellent positional and elevation control (Weir, 1971). The uncertainty associated with Bouguer anomaly values from each of the above two data sources has been estimated as ± 0.75 mGal (Miller and Weir, 1982), the uncertainty in applying the conversion formula, Equation A.1, developed by the Earth Physics Branch.

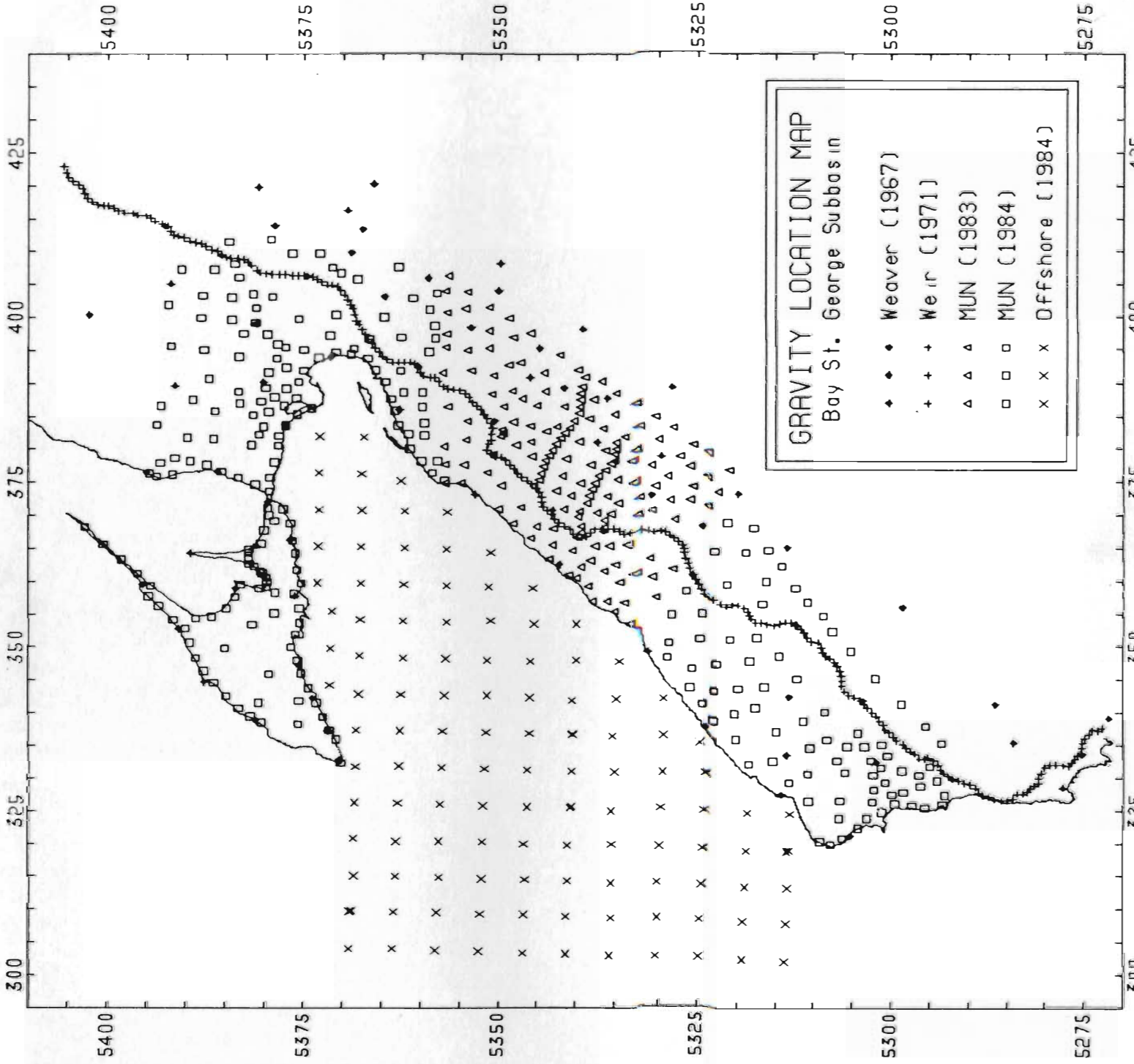

Figure 3.1. Posting map of gravity field stations. Various data types are distinguished by the symbols listed. Coordinates used here and in maps that follow are Universal Transverse Mercator (UTM) $\times 10^3$ of Zone 21.

More recently, personnel from Memorial University of Newfoundland have increased gravity data coverage to an average station spacing of 5 km throughout the onshore Carboniferous subbasin to the southeast of St. George's Bay as well as on the Port au Port Peninsula on its northern margin. The recent onshore data were collected in several stages by conducting traverses along all accessible roads, augmented by several helicopter traverses to more remote areas. Coverage is fairly uniform despite difficulties in data collection presented by extensive swampy or inaccessible regions. Gravity was measured at 417 stations occupied during 1983 and 1984 summer seasons with a Lacoste and Romberg land gravimeter. Wallace and Tiernan altimeters and sling psychrometers were employed at both the roving and base stations to determine elevations by aneroid barometry to ±2 m (see Appendix A-3). Traverses started and ended with readings at centrally located base stations of the Canadian National Gravity Network. Horizontal positioning of stations was established by reference to distinctive landforms or man-made features on 1:50,000 topographic maps of the area. Positions determined in this way are considered accurate to less than 50 m. Where possible, stations were occupied over Canadian Geodetic Survey horizontal/vertical control markers or other points of known elevation indicated on these maps. Formulae for data reduction are included in Appendix A-4. Overall uncertainty in determination of Bouguer anomalies for land stations is estimated as ±0.5 mGal, most of which is associated with the ±2.0 m station elevation uncertainty.

Corrections were not made for the effects of variable terrain at onshore stations. Terrain corrections were estimated by Peavy (1985) to be less than 0.5 mGal for stations located in the gently varying topography of the Carboniferous basin proper. For stations located within the Long Range Mountains which rise 300 m abruptly along the southeastern margin, terrain corrections as large as 15 mGal are possible. However, only

at a few stations would terrain corrections exceed 5.0 mGal (Peavy, 1985), due to deliberate positioning away from steep elevation gradients. The stations for which the largest terrain corrections would apply are located to the southeast of the Long Range Fault. Bouguer anomaly values at these stations are not essential to analysis of the Carboniferous basin, but rather were occupied to define the gravity gradient associated with the lithologic change along this boundary.

A total of 122 offshore underwater gravity stations were occupied on a 6 km grid covering all of St. George's Bay and extending westward beyond the tip of the Port au Port Peninsula. Three Mini-Ranger transponders emplaced over survey markers on nearby cliffs provided horizontal positioning by triangulation methods. The elevated cliffs and ideal geometry of the basin margins enabled strong transponder signals and provided excellent horizontal control. The uncertainty in horizontal position is estimated to be better than ±25m as determined from the positioning errors. Water depths, accurate to within 1 m, were scaled from the survey vessel's depth sounder records. The offshore survey was tied to Canadian National Network base stations at Argentia, Nfld. in a previous leg of the survey and at Port Harmon, Nfld. within the study area, with two base ties at the latter.

Five (5) stations or about 4% were reoccupied to provide a check on navigation, since the repeatability of horizontal positioning affects also the repeatability of depth and meter reading. Statistics for station repeats are listed in Table 3.1 below. Sample standard deviations are quoted here. Average absolute difference in position was 205 m with a standard deviation of 139 m. Two station pairs repeated with no difference in water depth, while one value of 10 m for a repeat in an area of steep seabottom gradients raised the mean to 1.2 m and increased the uncertainty to 5.0 m. The mean of Bouguer differences on reoccupation was 0.36 mGal. It is interesting to note that while

large differences in positions are associated with the largest differences in water depths, there is no similar strong correlation with differences in Bouguer anomalies. Station positions did not repeat as well as expected despite the fact that the vessel was equipped with dynamic positioning having bow and stern thrusters. Poor positional repeatibility reflects the ship's inability to accurately reoccupy a station and is not an indication of Mini-Ranger navigational reliability. Position differences for repeated stations showed largest differences in the northing component. This is unfortunate in that calculation of the gravity reference field is latitude dependent (Appendix A-5) and the local field is generally more variable in the north-south than the east-west direction.

Table 3.1
Repeatability Statistics

Station Numbers	Δ Easting (m)	Δ Northing (m)	Δ Position (m)	Δ Water Depth (m)	Δ Bouguer Anomaly (mGal)
7286-7201	152	-339	371	10.0	1.5
7311-7207	88	34	94	0.0	-1.0
7302-7211	130	-226	261	-2.0	1.4
7247-7221	24	-20	31	0.0	-0.3
7275-7253	65	-262	270	-2.0	0.2
Mean	92	-162	205	1.2	0.4
St. Dev.	51	161	139	5.0	1.1

Table 3.1. Station repeatability statistics for 5 of 122 gravity occupations located in St. George's Bay.

All the 1983 and 1984 gravity data were reduced to Bouguer anomalies using the 1967 International Gravity Formula (see Appendix A-5), with crustal and seawater densities of 2.67 gm/cm^3 and 1.03 gm/cm^3, respectively. No corrections were made for regional water variations or tides.

Principal facts for the entire gravity data set are listed in Appendix A-6. Posted and contoured Bouguer anomaly values from all sources are presented here as Map 2. Features present on this map will be discussed later in Chapter 5. Contour smoothness

and consistency in trend indicate that data from the various phases of collection are in excellent agreement. Only two of the stations recently occupied are of questionable quality on the basis of contoured Bouguer anomalies: station 550 of the 1983 land survey and station 7265 of the 1984 underwater survey. The former is situated in an area of steep local gravity gradients while the latter lies on the southwestern margin of the offshore survey area where water depths are most variable and the gravity field is laterally ill-defined.

3.2. Magnetic Data

Total field magnetic data were compiled from three sources, each originally collected at different reference levels and processed using varying techniques. Therefore, each required separate treatment during compilation. Through application of digital filters and least-squares best fitting the three datasets were essentially upward continued and referenced to a common datum. Figure 3.2 is provided to show the locations of interpolated stations and coverage associated with the three datasets.

3.2.1. Aeromagnetic Data - GSC. Maps

Onshore aeromagnetic data in the Bay St. George area consist of a series of map sheets representing two phases of data collection. All data are published by the Geological Survey of Canada at a scale of 1:63360 (1 inch = 1 ile) as maps 0.5 ° in longitude by 0.25 ° in latitude. The earlier phase was collected during July and August, 1953 using a flux-gate magnetometer with a total field reference background setting of the order of 2000 gammas. Flight lines flown at 300 m altitude in an east-west direction and spaced at 800 m surveyed a strip from 48 ° to 49 ° N (4 map sheets in width) from western to east-central Newfoundland. These data are not referenced to the IGRF (International Geomagnetic Reference Field). The second phase of data collection was flown in a similar fashion and at the same resolution over the remainder of Newfoundland from February 1966 to August 1967 to the north of the first phase and from April 1967 to November 1969 to the south, but in this case using a proton precession magnetometer. This dataset differs from the first in two ways: absolute magnitude of the total field was recorded and, by using Doppler navigation, flight lines were extended offshore for some distance, whereas in the earlier phase data ended at the shoreline. Magnetic values were digitized at a 0.8 km spacing in both latitude and longitude on all maps covering the study area. Before removal of the IGRF background field, the dataset from the earlier phase required referencing to a true total field consistent with the second dataset. Along

3.2. Magnetic Data

Total field magnetic data were compiled from three sources, each originally collected at different reference levels and processed using varying techniques. Therefore, each required separate treatment during compilation. Through application of digital filters and least-squares best fitting the three datasets were essentially upward continued and referenced to a common datum. Figure 3.2 is provided to show the locations of interpolated stations and coverage associated with the three datasets.

3.2.1. Aeromagnetic Data - GSC. Maps

Onshore aeromagnetic data in the Bay St. George area consist of a series of map sheets representing two phases of data collection. All data are published by the Geological Survey of Canada at a scale of 1:63360 (1 inch = 1 ile) as maps 0.5° in longitude by 0.25° in latitude. The earlier phase was collected during July and August, 1953 using a flux-gate magnetometer with a total field reference background setting of the order of 2000 gammas. Flight lines flown at 300 m altitude in an east-west direction and spaced at 800 m surveyed a strip from 48° to 49° N (4 map sheets in width) from western to east-central Newfoundland. These data are not referenced to the IGRF (International Geomagnetic Reference Field). The second phase of data collection was flown in a similar fashion and at the same resolution over the remainder of Newfoundland from February 1966 to August 1967 to the north of the first phase and from April 1967 to November 1969 to the south, but in this case using a proton precession magnetometer. This dataset differs from the first in two ways: absolute magnitude of the total field was recorded and, by using Doppler navigation, flight lines were extended offshore for some distance, whereas in the earlier phase data ended at the shoreline. Magnetic values were digitized at a 0.8 km spacing in both latitude and longitude on all maps covering the study area. Before removal of the IGRF background field, the dataset from the earlier phase required referencing to a true total field consistent with the second dataset. Along

map edges where the data from the two phases merge (ie. at the 48° and 49° N latitude boundaries), magnetic field values were digitized from the corresponding maps located north and south of these edges at a 0.8 km spacing relative to their median longitudes in a manner consistent with Peavy (1985). The d.c. shifts or offsets obtained from differences in field levels to either side were then fitted to a 2^{nd} degree least-squares polynomial in x, the distance (positive eastwards) from the median on each map sheet pair boundary, expressed in terms of 0.8 km grid units:

$$y(x) = C_0 + C_1 x + C_2 x^2 \tag{3.1}$$

The coefficients, C_i, $i = 0,1,2$, of these polynomials were then used to generate offset values, $y(x)$, for all points, x, along this Phase I/Phase II boundary. To obtain an offset estimate for each digitized location within the map area, linear interpolation was used between the offsets corresponding to its longitude derived from these polynomials at 48° and 49° N latitudes. Interpolation was carried out from polynomial descriptions specific to the latitude range of each map sheet in attempts to keep distortion to a minimum. Four map sheet pairs were correlated in this way at the 48° N boundary while only the two easternmost corresponding map sheets required such correlation to the north of the study area. To extend such interpolation west of 58° 30′ W longitude at the northern 49° N map boundary (ie. seaward where no aeromagnetic map sheet pairs were available) a second degree polynomial was fitted through values for the two map sheets east of 58° 30′ W, from which offsets were generated for longitudes to the west of this point. Coefficients of the various polynomials used in generating offsets at map boundaries are listed in Table 3.2. As would be expected, the dominant coefficient in these polynomials is the C_0 or d.c. offset term.

Table 3.2
Polynomial Coefficients for Least-Squares Fit
of Magnetic Map Boundaries

Map Sheet Boundary	C_0	C_1	C_2
At 48 ° N boundary:			
59 ° – 30′ to 59 ° – 00′ W	53259.45	-1.0671	0.0295
59 ° – 00′ to 58 ° – 30′ W	53345.82	0.5629	-0.3104
58 ° – 30′ to 58 ° – 00′ W	53212.16	-0.0243	0.1431
58 ° – 00′ to 57 ° – 30′ W	53238.58	-0.7204	0.1497
At 49 ° N boundary:			
58 ° – 30′ to 58 ° – 00′ W	53247.65	0.4564	-0.0696
58 ° – 00′ to 57 ° – 30′ W (two map sheets)	53262.55	0.9154	0.0342
58 ° – 30′ to 57 ° – 30′ W	53224.70	0.3855	0.0038

Table 3.2. Listing of polynomial coefficients for least-squares fit of magnetic background levels along map boundaries where data from different aeromagnetic datasets overlap.

Next the IGRF background was removed to obtain values of residual magnetic field anomaly. A Fortran program of Miller and Weir (1982) was adapted to the present study to carry out IGRF removal and subsequent 25 point $\frac{1}{r}$ weighted averaging to suppress short-wavelength features.

Values for magnetic IGRF background were obtained by bicubic spline interpolation between values of the IGRF total field intensity reference for year 1965.0 at corner co-ordinates of a 2 ° by 2 ° grid in latitude and longitude listed in the IAGA Bulletin 29 (1971). Although the IAGA Bulletin recommends use of a similar second difference interpolation technique from its 2 degree square grid tables, applied first in latitude followed by interpolation in longitude, IGRF values obtained by employing a simple linear interpolation method differ from those calculated directly by a maximum of only +20 gammas (Fabiano and Peddie, 1969), that representing the difference attained only at low latitudes where the magnetic field is spatially most variable. Bicubic spline interpolation

was adopted here rather than the linear interpolation used by Miller and Weir (1969) to more closely approximate the true IGRF through removal of a smoothly varying, as opposed to a piecewise continuous, magnetic reference field. A routine employed from the IMSL user library (1984) enabled convenient application of bicubic spline interpolation. Comparison of interpolated IGRF values from linear and bicubic spline methods in this study were found different by a maximum of only +10.1 gammas when applied to listed grid values for the area of interest.

Inverse distance filtering removes much of the effect of features having wavelengths less than the filter's effective width, 4.0 km in this instance. This smoothing reduces the influence of high frequency variablility in the digital data due to near-surface inhomogeneities of magnetic mineral content that would confuse or complicate a regional interpretation. Values for the $\frac{1}{r}$ grid used are found in Appendix B-1. The center point in the averaging grid was given a weight of twice that of any point 1 grid unit radially distant from the center. Near the data edges, averages were calculated on the condition that a minimum of three rows or columns of data lie beneath the filter grid. Magnetic averages were normalized by the sum of only those grid weights situated over real data. As only one magnetic value was obtained for every 25 digitized values (running averages were not necessary), a "station" spacing of 4.0 km was simulated, consistent with the order of average gravity station spacing.

3.2.2. Aeromagnetic Data - Spector (1969)

An aeromagnetic survey was carried out over the inner reaches of St. George's Bay and adjoining coastlines by Lockwood Survey Corporation during the spring of 1969 (Spector, 1969). The survey is sited within an area 100 by 50 km (60 by 30 mi) with the longer dimension oriented nearly NE-SW. Traverses in NW-SE and N10°E directions were flown at an altitude of 300 m ASL using a fluxgate magnetometer for a total of

2465 line kilometers.

Data reduction and interpretation is described in a report by Spector (1969) and summarized here. Although data were reportedly presented on maps as total field intensity, from which values were digitized at a square grid spacing of 0.8 km (Spector, 1969), neither the total field intensity map nor the digitized data accompany the report. Since the survey was referenced to an arbitrary level, a planar trend was fitted to the data to remove a linear gradient approximation to the local geomagnetic intensity. Next a logarithmic energy spectrum was calculated for the data to distinguish energy arising from sources near the surface from that of sources located at depth by the method of Spector (1965). The effects of a near-surface ensemble of sources were estimated from the higher frequency portion of the spectrum to arise from sources at 0.6 km average depth. Estimated average depth to deeper sources was 3.35 km. A matched filter was designed to separate the long wavelength features resulting from deeper sources from near-surface features. Since the filter had an effective width of 4.0 km, this is the width of a margin at data boundaries inside which the filter was applied. Maps of near-surface and regional components accompany the report. By a similar technique, a filter was designed to downward continue the regional component to a plane at 5.6 km depth. Depths to sources were estimated from anomalies on downward continued regional field maps which also accompany the report.

The regional component of magnetic field anomaly consisting of long wavelength features from the Spector (1969) study was considered most similar to the other onshore and offshore filtered data sets in terms of frequency content. Hence, contours of regional component were digitized from the maps displayed on a similar projection and at an arbitrary scale. Digitized points were scaled and mapped with a minimum of distortion into UTM coordinates to enable display and comparison to the other data sources (Fig-

ure 3.2). Short wavelength features, excluded in the regional and present on near-surface component maps, are only prominent in two areas indicating the presence of shallow sources. The first forms an arcuate belt trending from SW to west in the offshore south of Port au Port and the other coincides with the core of the Flat Bay Anticline.

The regional component dataset was found to adequately fill the former data void (Map 3) and its contours showed trends roughly consistent with those of the other two datasets. However, upon plotting and comparison, a datum mismatch was observed at the three margins of the dataset where contours overlapped those of the filtered GSC aeromagnetic data flown at the same elevation (see Figure 3.2). Offsets were then evaluated by first approximating the value of the Spector data at the filtered GSC station positions. Since a planar regional field had previously been removed from the data, a first-order least-squares surface in UTM coordinates was fitted to offsets to obtain a datum correction. Coefficients for the correction polynomial may be found in Appendix B-3. The Spector data displayed on Map 3 is uncorrected. Digitized values from the dataset were corrected previous to modelling (discussed in later sections). Figure 3.3, showing the correction applied to values along seismic line E-24, gives an indication of the correction magnitude.

3.2.3. Sea Magnetometer Data

During 1968 and 1969, two cruises of the CSS Baffin of Bedford Institute of Oceanography, Dartmouth, recorded measurements of the magnetic field over the northeast and southeast Gulf of St. Lawrence. This seamag data provides excellent coverage in the offshore regions of the present study west of the Port au Port Peninsula. Total field intensity output from a Barringer 104 proton precession magnetometer towed 200 m astern of the vessel was recorded every six seconds on digital tape (Haworth and McIntyre, 1975). Linear averaging was subsequently performed (by Atlantic Geoscience

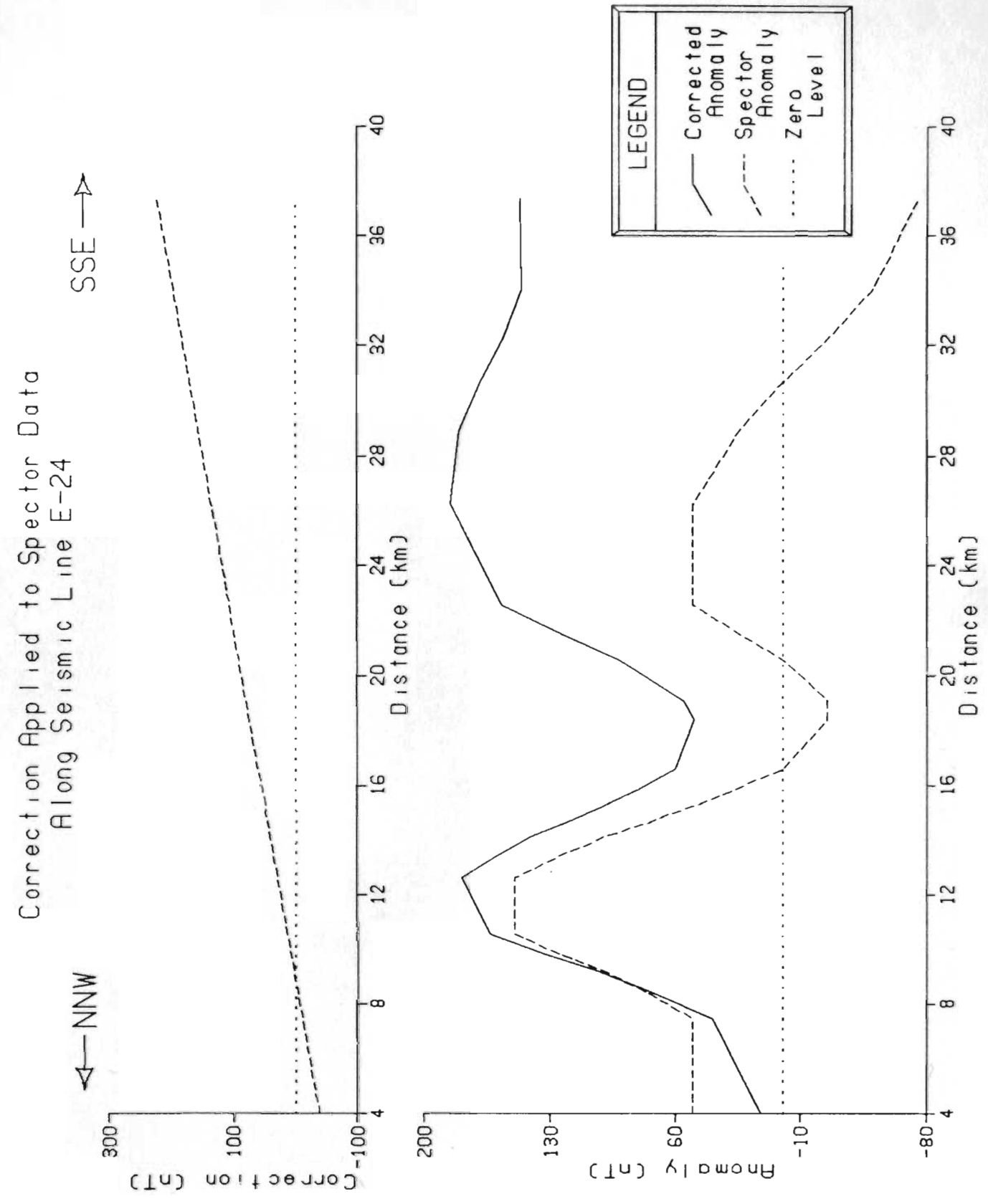

Figure 3.3. Linear correction applied to Spector (1969) data along seismic line E-24.

Center personnel) over segments of ten consecutive values to simulate a station output at 1 minute intervals consistent with simultaneously recorded surface gravity meter data. Values were discarded where showing large variability. At an average survey speed of 20 km/hr, digital data were spaced at approximate 0.33 km intervals along traverses.

Positional control for the seamag survey was provided by Decca 12F Lambda in the two range mode (Haworth and Watts, 1974) to within accuracies determined by the Canadian Hydrographic Survey as better than ±200 meters at the 95% confidence level. Traverses were oriented in east-west directions with tie lines directed nearly orthogonal where navigation would permit. Traverses were spaced at 3.7 km over much of the Gulf. Spacing was reduced to 0.9 km in the shallow waters south of the Port au Port Peninsula and to the west in areas adjacent to the Magdalen Islands. Although magnetometers were monitored at temporary onshore locations surrounding the Gulf of St. Lawrence during the survey, attempts at constructing a diurnal variation model failed to produce significantly improved corrections over those obtainable using the measured variation at Dartmouth, NS. (Haworth and MacIntyre, 1975). The diurnal variation applied to correct magnetic data recorded in the Gulf of St. Lawrence was that monitored at Bedford Institute, Dartmouth during survey. Magnetic anomalies were calculated by removal of the IGRF from total field values. Data quality and navigation control are considered to be excellent.

The raw data corrected for diurnal variation were made available in digital format by personnel of the Atlantic Geoscience Center, Bedford Institute. Preliminary plots of magnetic anomalies revealed that on certain traverses, offsets with magnitudes of up to 150 nT were present at points of line intersection. An offset correction scheme adapted from Mittal (1984) and described in Appendix B-2 was employed to eliminate offsets and

correct magnetic anomalies to an internally consistent datum. Smoothing was subsequently performed by a cosine bell of 5 stations width over assumed equidistant stations along traverses. The values obtained were assigned to the center positions of this filter, from which only every 8^{th} "station" was selected for map preparation (see Figure 3.2). This simulated an along-line station interval of 3.3 km, consistent with the average coarser survey line spacing. No direct smoothing operations were performed on values across adjacent lines. However, further averaging resulted from generation of $\frac{1}{r}$ distance-weighted grid nodes during contour map preparation.

3.3. Trend Surface Fitting

Gravity and magnetic anomaly data show features of varying wavelength and amplitude. Removal of a regional trend from regularly gridded data is easily carried out in the frequency domain by Fourier methods. However, where data are irregularly spaced or where large areas are not represented by the data, as in the case under study, application of Fourier methods becomes difficult. Errors may be introduced in attempts to interpolate potential field values onto a regular grid. Very long wavelength features may be removed from the data to enhance local features of interest by fitting a trend surface described by orthogonal polynomials (Whitten, 1973) to the data and calculating differences from this surface as residual anomalies, as outlined by Nettleton (1976). A least-squares surface of order n in a rectangular reference frame may be described in x and y by:

$$S_i(x,y) = \sum_{j=0}^{n} \sum_{k=0}^{n-j} a_{jk}\, x^j\, y^k, \tag{3.2}$$

where $S_i(x,y)$ is the trend surface amplitude for the i^{th} location (x, y) and a_{jk} are the coefficients of the two-dimensional polynomial regression surface. The coefficients, a_{jk}, are determined by a least-squares matrix inversion. The forward problem may be

expressed as a minimization of distances from the trend surface to the potential surface described by anomalies $g_i(x,y)$. Setting the first derivatives of the N equations described by

$$\sum_{i=1}^{N} [g_i(x,y) - S_i(x,y)]^2 \tag{3.3}$$

equal to zero, the problem, in matrix notation, becomes:

$$[\sum_{i=1}^{N} x^{m+j} \; y^{k+l}] \, [a_{jk}] = [\sum_{i=1}^{N} g_i(x,y) \, x^m \; y^l] \tag{3.4}$$

(after Miller, 1970). Elements of the coefficient matrix may be obtained by least squares inversion of the first matrix as:

$$a_{jk} = [\sum_{i=1}^{N} x^{m+j} \; y^{k+l}]^{-1} \, [\sum_{i=1}^{N} g_i(x,y) \, x^m \; y^l] \tag{3.5}$$

A trend surface fitting FORTRAN program was taken from Whitten (1973) and adapted by T. Laidley to computer facilities at Memorial. The program enables least-squares trend surface fitting of two-dimensional polynomials to order 8. In the present study, this program was altered so that polynomials were referenced to an origin located at the center of data with x and y axes oriented along Easting and Northing UTM coordinates. The program was previously written to expand a polynomial about an origin located at the lower left hand corner of the data window. For the large area under study, referencing to a corner origin resulted in deteriorated accuracy when fitting polynomials of order higher than 3, such that with increasing orders higher than 5, the correlation of the fitted surface was found to decrease rather than increase. By referencing to a central origin, the ranges of x and y were effectively halved so that their exponentiation to high orders resulted in reduced overall truncation error during summation. For low order fits and for regions having narrower distance ranges, this problem would not arise. In the case of magnetic anomalies where stations have a greater areal extent

(Figure 3.2), distances were also scaled to values near 1.0 before trend surface fitting to avoid computer overflow at the higher polynomial orders.

3.4. Physical Parameters

Densities and magnetic susceptibilities for samples of Carboniferous sedimentary rocks and pre-Carboniferous basement rocks collected or obtained from drill cores were determined by Peavy (1985). The density of each sedimentary sample was assigned to a geologic formation or member within a formation so that all major rock lithologies were represented and the densities for all samples within each unit were averaged. As well, halite, gypsum, and anhydrite from drill cores were sufficiently sampled to obtain representative densities for the evaporite sequences.

Having obtained densities for each sediment unit, each was assigned a weighting, corresponding to its relative thickness estimated from onshore exposures from which weighted average densities and sample standard deviations were calculated for the Anguille, Codroy and Barachois Groups. Relative thicknesses of Barachois units were measured from a borehole core. The densities of units and the weighted averages along with standard deviations are reproduced here as Table 3.3 for reference.

Representative densities of 2.63, 2.47 and 2.54 g/cm^3 were obtained by Peavy (1985) from thickness-averaged samples from the Anguille, Codroy and Barachois Groups, respectively. Anguille units show higher densities (Table 3.3) and thus density contrasts (relative to 2.67 g/cm^3) lower in magnitude than the overlying Codroy and Barachois Groups. Such findings are consistent with observations by Knight (1983) that competent well-cemented Anguille clastics contrast sharply with the more friable younger Carboniferous clastics. Watts (1972) used postulated densities of 2.67, 2.2, and 2.45 g/cm^3 for the equivalents of Anguille, Codroy and post-Codroy Group sediments in gravity modelling studies within the East Magdalen Basin. The low density of Windsor

Table 3.3
Rock Densities

From Peavy (1985):

Group	Geologic Unit Fm./Member	Map Unit	Density ± Standard Deviation (g/cm^3)
Anguille	Kennels Brook	2	2.58±0.11
	Snakes Bight	3	2.67±0.10
	Friars Cove	4	2.67±0.04
	Spout Falls	5	2.59±0.04
	Fichells Cong.	5a	2.32±0.03
	Average		2.63±0.06
Codroy	Ship Cove	6	2.72±0.03
	Codroy Road	7	2.48±0.14
	Robinsons River/		
	Jefferys Village	8a	2.40±0.09
	Highlands	8b	2.53±0.13
	Brow Pond Lentil	8e	2.58±0.03
	Average		2.47±0.09
Barachois	Searston	9	2.51±0.08
	Upper Series	10	2.56±0.08
	Average		2.54±0.08
Evaporites	anhydrite		2.97±0.03
	gypsum		2.28±0.03
	salt		2.18±0.03

From Present Study:

Codroy	Robinsons River/		
	Overfall Brook	8c	2.44±0.08 (19)
	Mollichignick	8d	2.55±0.12 (75)

Table 3.3. Summary of densities averaged from representative sedimentary rock samples collected in the onshore portion of the Carboniferous Bay St. George Subbasin. The numbers of samples used in determining lithologic densities and their standard deviations, as measured in the present study, appear in brackets; the numbers of density measurements of the Peavy (1985) study are not available.

Age sediments in Watts' (1972) paper reflects a considerable thickness of evaporites in the section. The high density value for pre-Windsor rocks corresponds with the values reported for the middle Anguille Group, non-conglomeratic clastics by Peavy (1985) and may result from increased density of these rocks with depth of burial within the deeper

parts of the Maritimes Basin.

Densities of pure salt sequences from boreholes were measured at 2.18 g/cm^3 with little variability (Peavy, 1985). This value closely agrees with the value of 2.15 g/cm^3 used by Watts (1972) in modelling salt structures. The presence of gypsum in the section, with a density of 2.28 g/cm^3, would be indicated by a negative Bouguer anomaly of greater magnitude than that of surrounding sediments. Anhydrite samples have a strong positive contrast of +0.20 g/cm^3 relative to assumed crustal density of 2.67 g/cm^3.

The densities, as measured by Peavy (Figure 4.1, 1985), of some 45 samples of Grenville age, Indian Head basement rocks gave consist results. These samples of anorsitic to granitic compositions are locally gneissic (Williams, 1985) and have densities averaging $2.68 \pm 0.07 g/cm^3$ with only 7 samples lying outside and symmetrically disposed about the 2.60 to $2.75 g/cm^3$ range. In contrast, the measured densities of 22 rock samples from the Steel Mountain Complex averaged $2.83 \pm 0.34 g/cm^3$ with 10 samples giving values above $2.70 g/cm^3$ (Figure 4.1, Peavy, 1985). The much greater variability in density of Steel Mountain samples is caused by a few samples of high density, two of which are greater than $3.20 g/cm^3$. Although the Steel Mountain Complex is considered to be Grenville in age, its high magnitude and variability of density, as compared with equivalents in the Indian Head Complex, probably results from the ranges in composition from anorthosites to gabbronorites and the strong metamorphic overprint, dated as Upper Ordovician, expressed as chloritization of Steel Mountain samples (Murthy and Rao, 1976). The bimodal and assymmetrical character of the density distribution for Steel Mountain samples (Figure 4.1, Peavy, 1985) may be reasoned as a reflection of this metamorphic overprint. Williams (1975) reports a mid-Paleozoic metamorphic grade increasing to the east with proximity to the Long Range Complex.

Two members of the Codroy Group, the Mollichignick and Overfall Brook units, were not present in the study area of Peavy (1985). Rocks of these units outcrop in a trough along the Long Range Fault southeast of the Anguille mountains (see Map 1). A representative suite of samples were measured for these rocks, the results of which are included in Table 3.3. Rocks were weighed while dry to obtain M_{air}, then reweighed while submersed in water at 15 ° C to obtain M_{wat}. A density was calculated for each sample as:

$$D = \frac{M_{air}}{(M_{air} - M_{wat})} \times D_{wat}\,; \tag{3.6}$$

where D_{wat} is the density of water (= 1.0 g/cm^3 at 4 ° C).

An average density and sample standard deviation were evaluated by linear averaging of results for all samples within each member. The method is consistent with that used in the study of Peavy (1985). In a few of the coarser grained, poorly cemented samples, small air bubbles formed on rock surfaces while submerged, indicating the porous nature of certain rock types and introducing a source for possible errors in determined densities. The values listed in Table 3.3 therefore represent dry densities, several of which should be treated with some reservation when used in modelling; a proper approach would entail weighing of saturated rock samples, from which a closer approximation to *in situ* densities could be evaluated. The larger standard deviations associated with densities of certain units are the result of variations in lithology within these units and generally do not reflect numbers of samples measured. No adjustments were applied to D_{wat} in Equation 3.6 for water temperature as the correction would be insignificant for temperatures near that of the water used in measurement (15 ° C).

No samples from the offshore were available for measurement. However, sediments in the offshore subbasin are considered to be largely Visean in age (Knight, 1983; also

later sections) and to have densities similar to those of sedimetns of the Codroy Group listed in Table 3.3. Onshore the Codroy units show the largest density variability of the groups, due to the lateral lithologic inconsistencies and the localized presence of evaporites. In the case of salt, possible flowage is responsible for observed large lateral density variations and the related short wavelength gravity anomalies.

Magnetic Susceptibilities

Magnetic susceptibilities of Carboniferous sediments and sediments in general are so low as to be nearly 'transparent' to an external inducing field (Peavy, 1985). The sediments within the subbasin and the Port au Port Peninsula carbonates do not affect the magnetic fields measured in the area, and thus require no further consideration.

By comparison, samples of basement rocks show variable susceptibilities ranging from near zero to 6000×10^{-6} cgs units (Peavy, 1985). Most samples from Indian Head basement have low and consistent susceptibilities of less than 100×10^{-6} cgs units, but samples from gabbroic lenses or layers rich in titaniferous magnetite within the complex (Williams, 1985) would yield higher values. Samples from the Steel Mountain anorthosite contributed the bulk of the variability in magnetic content of the basement samples measured, owing to the presence of magnetite rich lenses or zones (Murthy and Rao, 1976). The variability in the measured magnetic field observed associated with the Indian Head Complex and proximal to outcrop of Indian Head rocks at Flat Bay are assumed the result of the variable magnetic content in these rocks.

In an aeromagnetic survey interpretation of the inner St. George's Bay region by Lockwood Survey Corp., Spector (1969) lists anomalous susceptibility estimates responsible for magnetic anomalies in Table III of his report. Nine (9) susceptibility contrasts lie within the range 70 to 340×10^{-6} cgs units, while a short wavelength anomaly near the coast at Flat Bay gave a high value of 900×10^{-6} cgs. The average of the ten (10)

susceptibility contrasts interpreted by Spector (1969) is 178×10^{-6} cgs. These values show the characteristic contrasts associated with anomalous features, such as magnetite lenses, so will be higher than the susceptibility of an equivalent homogeneous basement layer. As a comparison, pre-Carboniferous basement was assigned a susceptibility of 100 to 130×10^{-6} cgs by Watts (1972) in his magnetic interpretation.

In summary, only basement of metamorphosed Grenville or older rocks has sufficient susceptibility to give rise to observed magnetic anomalies. Lenses of variable susceptibility within the basement give rise to the magnetic field variations observed. To model an equivalent homogeneous magnetic basement, a susceptibility of approximately 100×10^{-6} cgs is deemed appropriate on the basis of the above discussion.

3.5. Reflection Seismic Data

The available reflection seismic data for the Bay St. George subbasin consist of 16 lines shot during 1971 and 1973 for Mobil Oil Canada, Ltd. in an area offshore between the western tip of the Port au Port Peninsula and the southeastern Bay St. George coastline (see Figure 3.4). From the more than 900 line kilometers reportedly shot during the program (Mobil Oil Canada, Ltd., 1973), about 340 km were available for this study. These data, in the form of processed seismic sections, cover an area of roughly half that of the offshore underwater gravimetry data. Velocity scans were available for two of the centrally located lines, E-20 and G-23. The following processing sequence was applied to the raw data (Mobil Oil Canada, Ltd., 1971):

- Binary gain recovery
- Static corrections
- Predictive gap-deconvolution
- C.D.P. gather
- Digital gain control scaling
- Velocity analysis
- Normal moveout
- 24-fold C.D.P. stack
- Predictive deconvolution with whitening

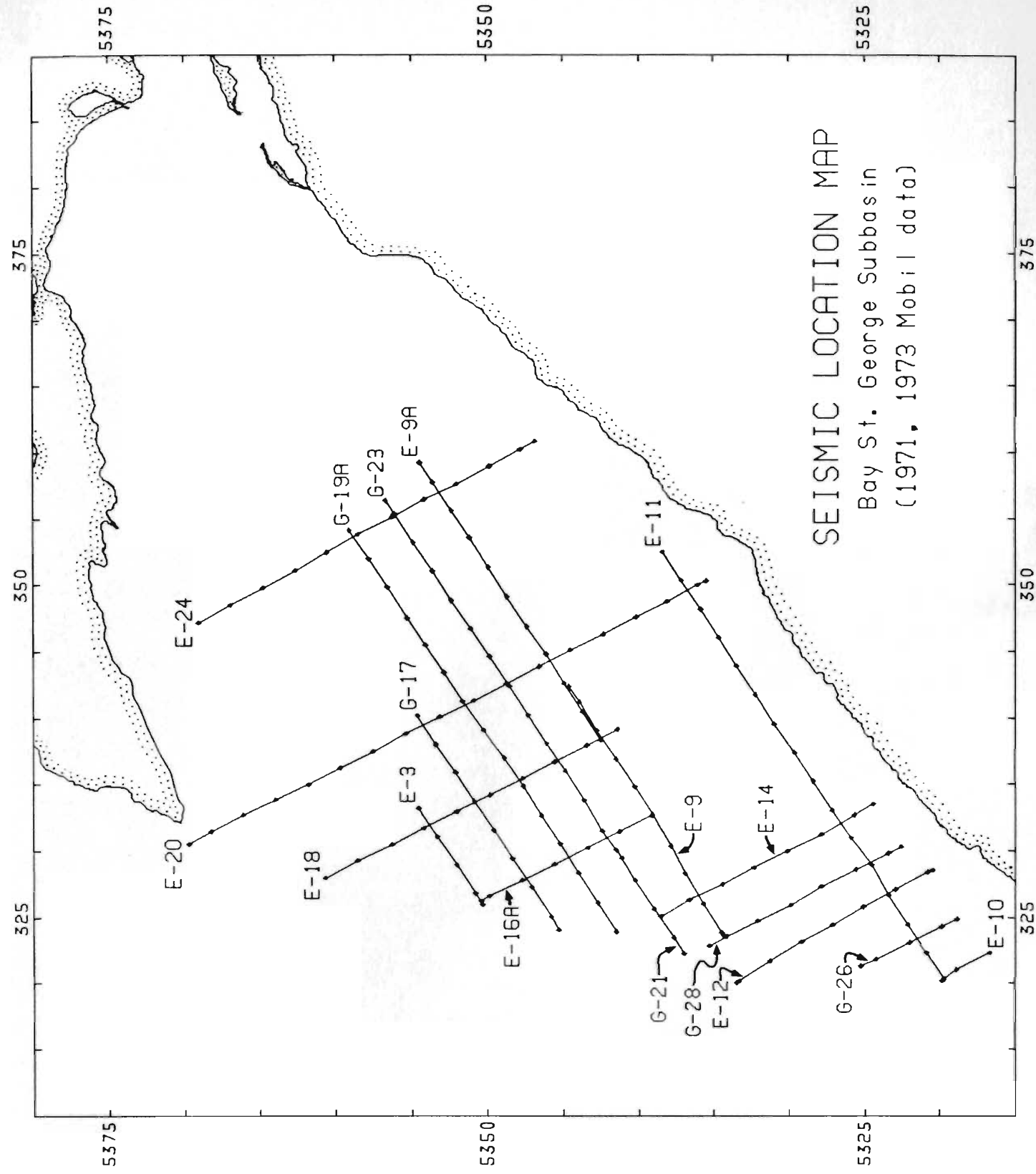

Figure 3.4. Reflection seismic survey location map. Line numbers are those of Mobil Oil Canada, Ltd., (1971; 1973).

- Time variant filtering
- Time variant scaling

Data were recorded at a 2 ms interval and processing was performed on the data subset sampled every 4 ms. Additional processing included air gun/geophone correction to sea level reference and relative static correction in areas of variable water depth in attempts to improve pre-stack reflector alignment (Mobil Oil Canada, Ltd., 1973).

Despite the fact that two phases of deconvolution have been applied to the digital data, strong water bottom reverberations or "ringing" persists throughout the sections. In many areas, reverberations are so strong that they completely overwhelm and mask early arrivals. Thus only later arriving strong reflections can be traced and correlated across several sections. As well, strong late arrivals are followed by a train of peg-leg multiples, creating interference on sections. The problem arises from a general deficiency in recent sediment cover over Carboniferous bedrock on the sea floor as a result of glaciation, thereby creating very large velocity and impedance contrasts at the water/bedrock interface. The problem was similarly noted in attempts to deploy a heat flow probe in conjunction with the gravity survey, in that limited areas had sufficient sedimentary cover. Data quality also varies widely from section to section, rendering certain sections relatively useless in the interpretation. Section E-24, included as Figure 3.5, represents the best of the sections available in terms of clarity and displays the character of reflected signal. In Figure 3.5 the sequence of reverberations that immediately follows strong R1 reflector arrivals is readily recognized. Multiples of reflectors are enhanced during amplitude scaling of the lower time section and may be observed here as late arrivals. Discussion of the interpretation is reserved for later sections.

Probable causes of inconsistent quality are variations in water depth and water bottom interface character, lateral lithologic changes within the section, less than optimum source/receiver array parameters, and poor weather conditions and/or quality control on

the many necessarily short lines during survey. Variable water depths are noted in the southwest corner of the seismic coverage, an area that corresponds to generally poor record quality. Application of proper time shifts or static corrections to individual traces representing source/receiver pairs is essential to good quality data in areas of variable water column. Combined with the persistence of reverberations, static corrections greatly influence optimum moveout hyperbola picks, and thus estimates of layer velocities from CDP gathers. It appears from velocity estimates that insufficient attention was exercised in applying static corrections to the data; a standard, rather than tailored, statics routine was probably applied before gather. Velocity scans for lines E-24 and G-23 show inconsistencies between scans along the same line, some of which may be attributed to lateral velocity variations along the seismic line, but most are the result of survey conditions and poorly defined parameters as described above. On the whole, data quality is poor to fair, largely the result of ineffective water bottom reverberation removal.

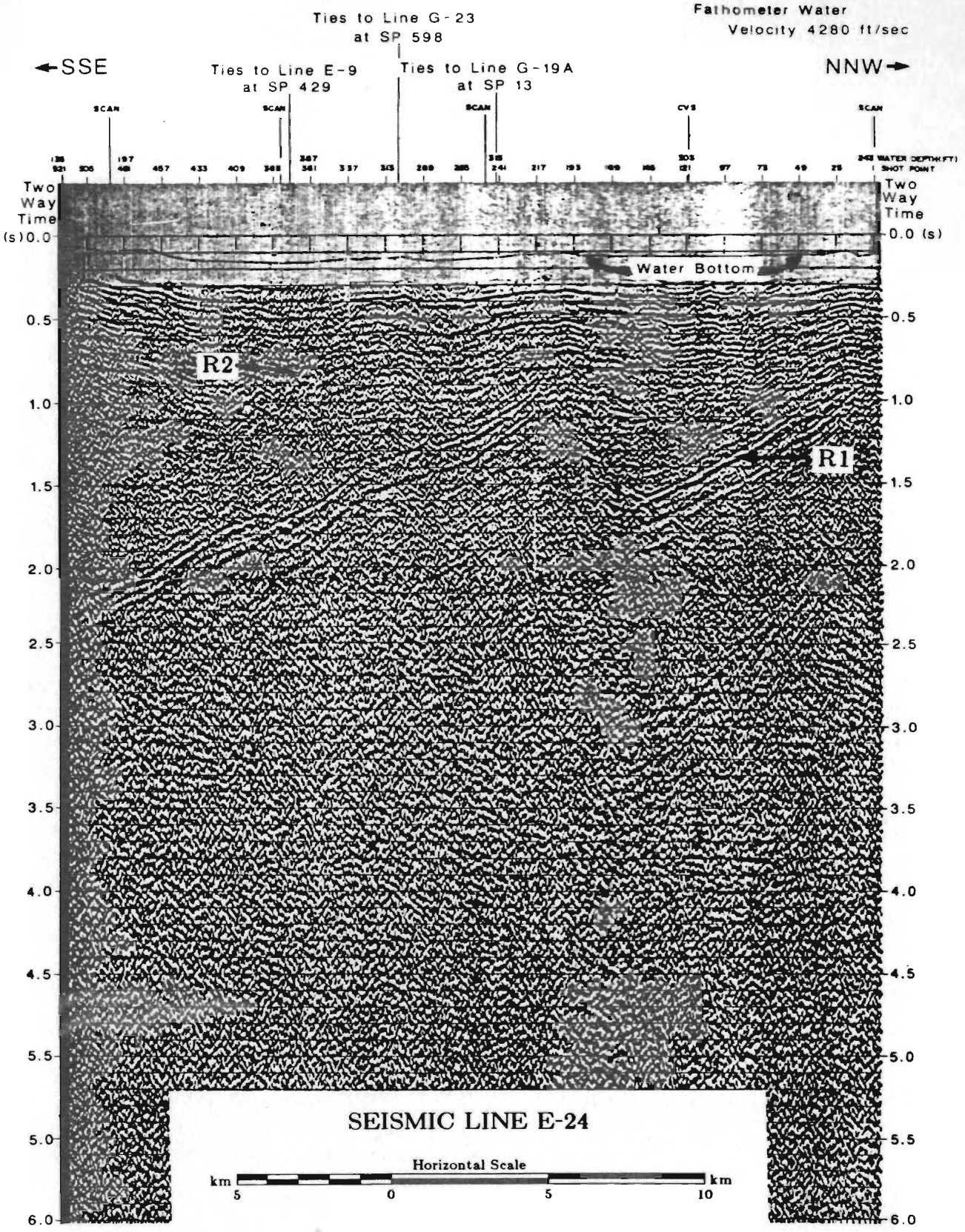

Figure 3.5. Seismic reflection line E-24 (Mobil Oil Canada, Ltd., 1971) showing typical data quality. Reflectors marked R1 and R2 are pre-Carboniferous basement and Codroy picks, respectively.

4. Potential Field Inversion

In attempting a depth-to-basement analysis for a sedimentary basin the logical starting point would be application of an inversion scheme to obtain depth estimates directly from profiles of potential field data, subject to known geologic constraints. The advantages of inverse methods are unbiased interpretation, speed and ease of use. Since there is no unique solution to any set of potential field data, contraints must be imposed to limit the range of possible solutions that result. The problem encountered in inverting potential field data is that the Green's Functions describing the fields are nonlinear in several of the model parameters. The linearity of gravity or magnetic potential with respect to density or susceptibility, respectively, enables easy determination of these parameters in cases where other model parameters are known and allows modelling using only a density or susceptibility contrast. Unfortunately, however, potential fields are generally found nonlinear with regard to determination of body coordinates or geometries.

Much recent literature has been devoted to the subject of inversion of potential field data (Al Chalabi, 1971; Safon *et al.*, 1977; Pedersen, 1979; Vigneresse, 1978; Last and Kubik, 1983; Guillen and Menichetti, 1984). FORTRAN routines were developed by Peavy (1985) at Memorial University to carries out an inversion scheme for gravity modelling using 2-D and 2.5-D models on profiles over sedimentary basins. The method carrys out iterative corrections for each observation station to a Bott-type (1967) infinite slab equivalent first model on the basis of calculated residuals at each iteration. By cosine bell weighted smoothing of these corrections over adjacent stations, the step size or correction was reduced and the oscillations inherent in the linear approximation were lessened. Iteration was continued until the sum of squares of residuals was reduced to a pre-specified tolerance, defined by observation uncertainty, or a maximum number of

allowed iterations was reached. However, for theoretical models having steeply dipping or vertical boundaries, this inversion suffers problems of slow convergence and generation of undesirable "side-lobes" in the solution, overdeepening z-values in the vicinity of the steep boundary. Figure 4.1 shows typical results of attempts to model using the cosine bell weighting scheme, an extreme case of a 5 km thick block of sediment with its top at surface and having vertical boundaries. Where steep or vertical boundaries are present, a very narrow width for the cosine bell smoothing is found most effective. A broader smoothing gives most rapid convergence for bodies having less steep boundaries. Other weighting schemes, such as $\frac{z}{r^3}$ (proportional to the vertical derivative of the gravity field), were extensively tested in the present study and found to exhibit similar characteristics. Fournier and Krupicka (1973) report improved rates of convergence of the iterative Bott-type linear inversion by application of regression to successive depth estimates. However, the method provides no remedy to the side-lobe problem inherent in the resultant models.

The sections that follow describe and compare methods by which potential field data may be modelled by inversion. The ultimate objective of this portion of the study is to explore the range of solutions that result from several inversion schemes when models are subjected to various constraints, and thus to develop the methodology best designed for modelling the sedimentary and basement rocks in the Bay St. George Subbasin. Section 4.1 is a brief description of the Gauss-Newton matrix inversion, which is the basis of many hybrid methods. Several evaluating routines were developed in this study based on one such hybrid, Marquardt-Levinberg inversion.

4.1. Gauss-Newton Inversion

A least-squares inversion scheme was used by Corbato (1965) to adjust the z-

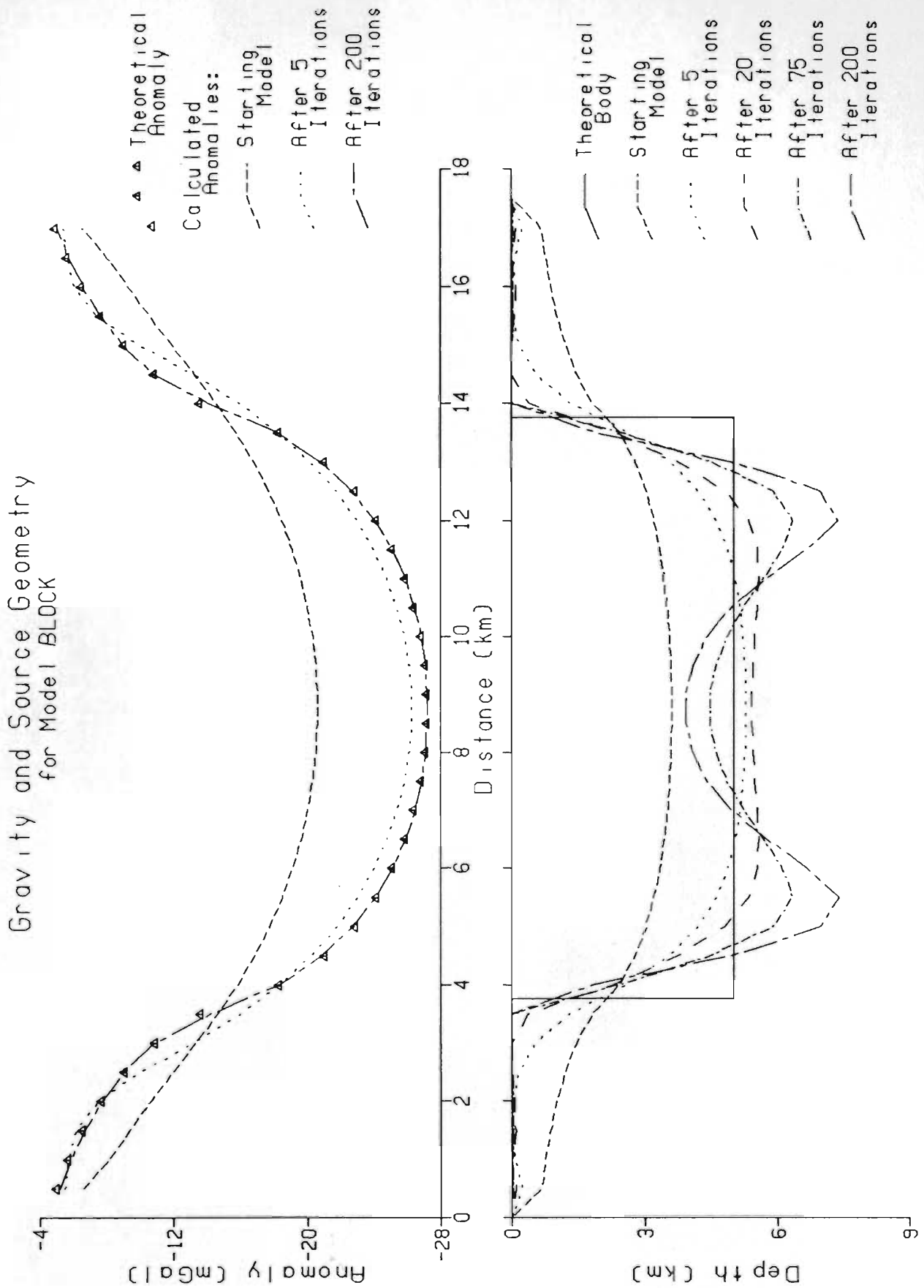

Figure 4.1. Example of the side-lobes generated in attempts to model a sedimentary block using iterative Bott-type (1967) gravity inversion. Gravity residuals are iterated to estimate the z values of body coordinates equally spaced in x.

coordinates of a two-dimensional Talwani-type polygonal body based on the residuals of approximated gravity anomalies. Thus, the function $F(X) = |G(X) - g(X_i)|$ is to be minimized where X is a vector of m unknown parameters and subscript i denotes estimates to X at the i^{th} iteration. $G(X)$ and $g(X_i)$ are vectors of n observed and calculated anomalies. The method is one of Gauss-Newton least-squares provided $n > m$. The nonlinear gravity function is linearly corrected by iterative application of the inverse Jacobian matrix of partial first derivatives of the gravity expression with respect to z-coordinates to the gravity residuals, $F(X)$. Corbato (1965) uses as an example an approximation to the parabolic shape of the base of a glacier. Convergence to the solution is rapid provided the starting values for unknowns are sufficiently close to the solution.

A similar scheme applying the Gauss-Newton method is given in Tanner (1967) for inversion of gravity data to generate bodies described by vertically sided prisms of infinite strike length. Two versions of Tanner's (1967) computer program allow the user the choice of evolving the model downward from the surface in the sedimentary basin model or upward from some lower reference to describe a granitic or intrusive body.

The Gauss-Newton method is one of least-squares in which a nonlinear function, $F(X_n)$ of some desired parameters $\{X_n\}$ is approximated by a linear function obtained by deleting the second and higher order terms from the Taylor's series expansion about some initial guess of the solution (Levinberg, 1944). The first guess at the solution may also be obtained by nonlinear methods. If the first guess lies far enough from the true solution that the nonlinear Taylor series terms cannot be safely ignored, then the iterative solution may never converge to the true solution. A major drawback of the Gauss-Newton method is that the ability to converge to a local minimum is highly dependent upon the initial starting point. Other methods use the calculated gradient of a function

to determine corrections toward a local minimum. The methods based solely on steepest descent or gradient suffer the drawback of being painfully slow in approaching a minimum in the region of parameter space near a local minimum (Marquardt, 1963).

4.2. Marquardt-Levinberg Inversion

Whereas Gauss-Newton is a method of least-squares, Levinberg describes a method of "damped least squares" (Levinberg-Marquardt least-squares), a linear combination of the Gauss-Newton method of first order Taylor series approximation and that of steepest descent. Brown and Dennis (1972) outline the Levinberg-Marquardt inversion scheme as a series of approximations having the form:

$$X_{n+1} = X_n - [\mu_n I + J(X_n)^T J(X_n)]^{-1} J(X_n)^T F(X_n) \qquad (4.1)$$

where I is the identity matrix, $J(X_n)$ is the Jacobian matrix of partial derivatives of the function $F(X_n)$, superscript T indicates matrix transposition, and μ_n may be thought of as the weighting that determines the emphasis of the method between that of steepest descent (when μ_n is large) and the Gauss-Newton convergence method (when μ_n is relatively small). For any nonlinear function and starting point, a "damping factor", μ_n, can be obtained for which the sum of squares of distances from the solution will be reduced (Levinberg, 1944). Levinberg outlines a method of finding the optimum weighting factor, μ_n, and shows that the optimum convergence rate is obtained when the same weighting factor is applied in all parameter dimensions. When $\mu_n = 0$ in Equation 4.1, the method defaults to that of Gauss-Newton.

The advantage of a Levinberg-Marquardt scheme over either of the two of which it is a combination, is that the direction of the correction vector and the step size are determined simultaneously. By limiting the value of increments from "overshooting" the minimum via the damping factor, μ_n, the sum of squares of residuals are minimized at each iteration. The Levinberg-Marquardt method may be thought of as a hybrid

method in emphasizing the better features of both, while bypassing their respective limitations. It adapts from the gradient methods the ability to converge from outside the region of convergence for the Gauss-Newton method, and from the Gauss-Newton method, the characteristic of rapid convergence as the minimum is approached.

Since linear functions have elliptical equipotential contours in parameter space, the degree to which a function is nonlinear dictates the degree of contour distortion from true ellipticity. As extremal points are approached, higher than first-order terms in the Taylor's expansion diminish in significance. Contours become progressively more elliptical as the expansion approaches linearity. Lines and Treitel (1984) illustrate graphically the relationship between the Gauss-Newton and Levinberg-Marquardt correction vectors toward a local minimum of a nonlinear function in a two dimensional cross-section of parameter space (Figure 4.2). It is in the nearly linear vicinity of a minimum solution that the Gauss-Newton method converges most efficiently. Because of the generally elongate nature of functions in parameter space (from a disproportionate dependence on one or some combination of parameters), the Gauss-Newton correction vector often lies nearly 90° from the correction vector obtained from gradient methods. The optimum correction vector is a linear combination of these two and must lie at an intermediate angle within 90° of the gradient vector (see Figure 4.2) (Marquardt, 1963; Lines and Treitel, 1984).

To apply a Levinberg-Marquardt scheme the Jacobian matrix of first derivatives must be obtained at each iteration, an operation that may be very tedious or computationally inefficient depending upon the nature of the nonlinear function. An alternative of approximating the Jacobian for the Gauss-Newton method by finite difference methods was alluded to by Corbato (1965). Brown and Dennis (1972) outline the structure of a "derivative free" finite difference version of the Levinberg-Marquardt least

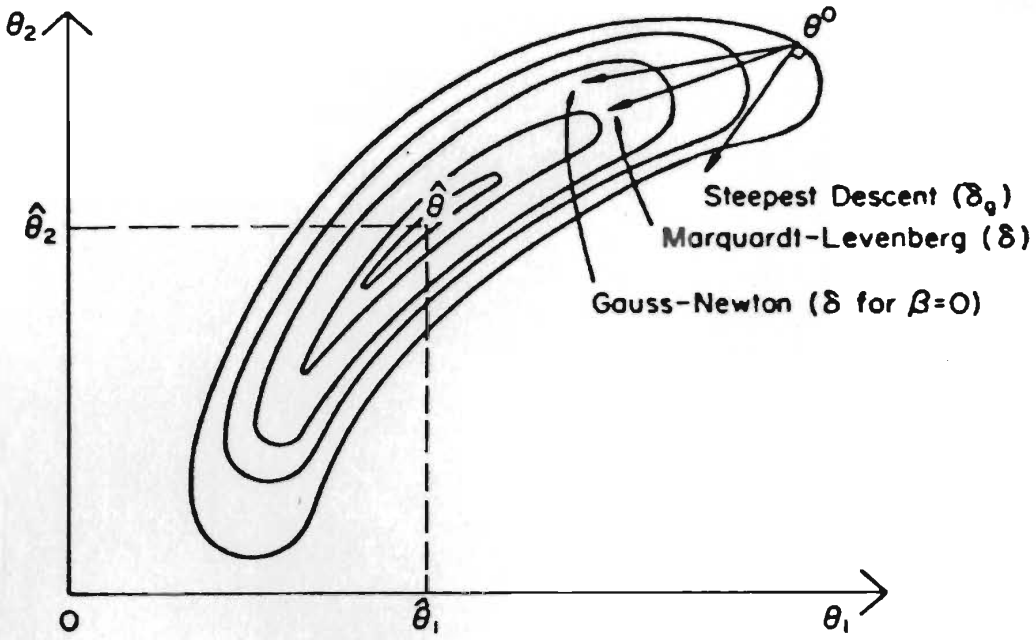

Figure 4.2. Two dimensional cross-section of nonlinear parameter space illustrating its non-elliptical nature (after Lines and Treitel, 1984). Note the angular relationship between correction vectors of the Gauss-Newton method, the strict gradient methods and the hybrid Marquardt-Levinberg scheme.

squares inversion. Here, $J(X_n)$ is approximated by use of finite difference quotients. A finite difference matrix is defined as:

$$\Delta F_{ij}(X,h) = f_i(X+hu_j) - f_i(X) \tag{4.2}$$

where h is the step size (real number) and u_j is the j^{th} unit vector such that the Jacobian matrix is approximated by

$$J(X_n,h_n) = \frac{\Delta F(X_n,h_n)}{h_n} \tag{4.3}$$

Then the analogue of the Levinberg-Marquardt equation (Equation 4.1) in iterative finite differences is:

$$X_{n+1} = X_n - [\mu_n I + h_n{}^{-2}\Delta F(X_n, h_n)^T \Delta F(X_n, h_n)]^{-1} h_n{}^{-1}]\Delta F(X_n, h_n)^T]F(X_n)$$

or

$$X_{n+1} = X_n - h_n [h_n{}^{2}]\mu_n I + \Delta F(X_n, h_n)^T \Delta F(X_n, h_n)]^{-1}\Delta F(X_n, h_n)^T]F(X_n) \quad (4.4)$$

(Brown and Dennis, 1972).

If μ_n and $| h_n |$ are of the order of $| \, | F(X) | \, |_2$, the norm (or distance from zero) of the function $F(X)$, the norm will tend toward zero on successive iterations and the finite difference scheme will be quadratically convergent (Brown and Dennis, 1972). The Gauss method tends to fail when X_n is far from the solution, that is, when the norm of $F(X)$ is large. Thus, a large value for μ_n is desired when beginning from some initial guess $\{X_0\}$ located far from the solution in parameter space, and μ_n should be reduced with each iteration to ensure rapid convergence by a dominantly Gauss-Newton type iterative method as the local minimum is approached (Lines and Treitel, 1984; Brown and Dennis, 1972).

Brown and Dennis (1972) report nearly identical results from applying the finite difference Levinberg-Marquardt scheme to a range of problems as were obtained using the "true" scheme involving inversion of a Jacobian matrix of exact partial derivatives.

4.3. Application of Least Squares

Although Peavy (1985) discusses several inversion techniques, methods involving matrix inversion were not implemented in his study, but, as previously discussed, automatic techniques involving modelling of geophysical bodies by iterative correction to a least squares solution were tested. The sections that follow describe the steps taken in the present study to design, implement and test the Levinberg-Marquardt inversion technique as applied to various potential field forward modelling algorithms. The purpose of this investigation was to compare various applications of this technique to other inver-

sion schemes, and thus develop the optimum inverse modelling routine for a specific geological scenario. In each application, the forward modelling kernel routine was optimized by equations of the most recent literature to minimize the computational overhead of repetitive function calls required by finite difference least squares inversion. In addition, the routines were encoded to be as general and adaptive as possible by invoking tests for special cases (Won and Bevis, 1987).

The IMSL library of subroutines (IMSL, 1984) under implementation at Memorial University has available a subroutine, ZXSSQ, designed to efficiently obtain the minimum of the sum of squares of M functions in N variables using the Levinberg-Marquardt finite difference technique. In order to effect least-squares, the routine requires that M exceed N, that is, the problem must be overconstrained. Nonlinear functions to be minimized may be evaluated by a user-supplied, external routine, enabling ZXSSQ to be readily adapted in minimizing any nonlinear function whose formula can be discretely described or closely approximated. In the present study, the residuals (observed minus calculated) of modelled potential field data are to be minimized. ZXSSQ allows the user to specify three convergence criteria which terminate the convergence process on the condition that one is satisfied: the estimated number of significant digits desired in the solution vector, the minimum difference in the sum of squares of residuals on two successive iterations, and the lower limit on the Euclidean norm or gradient. As well, a maximum limit may be placed on the number of user-supplied function calls allowed. The subroutine starts its iteration using a value for the damping factor μ_n, decreasing this parameter automatically by a step constant on successive iterations. However, if an iteration fails to converge, μ_n is iteratively increased by the square of the step size until convergence is re-established or the upper limit of μ_n is reached. The user may supply the starting μ_n value, the step-size and limits for μ_n; alternatively,

default values calculated from the norm may be used. Forward differencing is used when μ_n is large (far from the minimum), while central differencing is employed where most efficient near a local minimum. Error codes signal the method of the process termination.

ZXSSQ is available in single or double precision versions. Either version is compatable with a single or double precision user-supplied function, but the latter is recommended to ensure rapid convergence. User-supplied kernel evaluating functions should be robust and encoded efficiently since many function calls (M) are required on each iteration. Further documentation may be found in the IMSL User Manuals.

Several functions were written to define residuals of gravity and magnetic data, from equations describing 2-D and 2.5-D forward models assuming density contrasts and susceptibilities to be homogeneous throughout the modelled bodies and assuming that the magnetic anomaly is entirely due to the inducing field.

4.3.1. Inverse Gravity Modelling

In the case of gravity, 2-D and 2.5-D forward model equations for a body of polygonal cross-section were adapted from Johnson (1967) and Rasmussen and Pedersen (1979), respectively, and efficiently coded in FORTRAN as external functions to be accessed by the ZXSSQ subroutine. The resulting polygonal body-type, 2-D/2.5-D gravity (Levinberg-Marquardt) inversion program is listed in Appendix A. The polygonal body routines were recently corrected to account for special cases as outlined in Won and Bevis (1987). Similar routines were written for vertically sided prism-type 2-D and 2.5-D models on the basis of eq. (2.49f), (page 74) of Telford *et al.* (1976) and formulae from Nagy (1965). An alternate version of the Nagy formula which eliminates the use of $\sin(x)$ terms was adopted from Banerjee and Das Gupta (1977).

In the case of magnetics, the 2-D and 2.5-D forward model polygonal body formulae of Talwani *et al.* (1965) and Rasmussen and Pedersen (1979) were written into residual evaluation functions. A formula describing the magnetic effect due to a 2-D vertical prism found in Telford (1976) (eq. 353, page 189) was likewise incorporated into an evaluating subroutine.

These functions were designed to invert data in such a way that the body is either "grown" downward (signalled by positive Z_o) from an arbitrary upper starting level, Z_o, or extended upward (negative Z_o) from some lower reference, Z_o, in a manner similar to that developed by Tanner (1967) in his sedimentary or intrusive body styles having "inward and outward sloping" boundaries, respectively. In either case, if a z-coordinate is evaluated as being negative on any iteration, its value is reset to zero. The calling program employs a piecewise cubic spline interpolation routine extracted from Forsythe *et al.* (1977) to approximate the observed gravity field at regularly spaced x-coordinates from irregularly spaced data values in obtaining a first estimate. Starting z-coordinates used throughout are calculated as points having thicknesses above or below Z_o as determined from the regularly spaced interpolated data by the Bott infinite slab method of equivalent thickness. Thus, a body geometry that directly (or inversely) mimics the gravity profile shape is used as the starting model.

Theoretical gravity models consisting of blocks having various geometries were devised to test the two inversion techniques. In most models, 34 stations (M) at a spacing of 0.5 km were symmetrically distributed over the theoretical bodies whose total length was 10 km. Prism and polygon coordinates were spaced at the same intervals with two additional "free" coordinates included beyond either extreme of the body's width during inversion, giving N a value of 24. The convergence criteria for various inversions are listed in Table 4.1 together with convergence results.

Table 4.1

Model	Type	Infer	IER	NI	Norm	NSIG	Marq	NC
Gravity models:								
5	P	2	0	8	0.15231	2.073178	0.00042	85
5	N	0	133	46	11.543023	0.895196	4.25267	1114
2-5	P	2	0	10	0.009450	1.596330	0.00016	135
2-5	N	2	0	30	0.485904	1.908675	2.17125	462
B3	P	2	0	5	1.242217	1.173869	0.16607	111
B3	N	2	0	7	1.903085	1.338115	0.00073	82
B2-5	P	2	0	8	0.122139	1.903971	0.00002	106
B2-5	N	0	39	13	0.209806	4.940729	2682.29565	272
B5-2	P	2	0	7	0.010691	1.701985	0.00000	156
B5-2	N	2	0	29	0.103828	1.944274	0.00666	440
Magnetic models:								
M.5-3	P	2	0	16	13.60339	1.905102	0.00005	194
M-3a	P	2	0	38	3.743032	1.246097	0.00004	452
M-3b	P	0	133	17	130.029465	0.494586	0.87936	222

Model:
- 5 - 5 km thick block starting from surface.
- 2-5 - 3 km thick block starting from a 2 km Z_o level.
- B3 - 3 km thick basin model starting from surface.
- B2-5 - 3 km thick basin model starting from a 2 km Z_o level.
- B5-2 - 3 km thick inverted basin model grown upward from a 5 km Z_o level.
- M.5-3 - 2.5 km thick block grown downward from Z_o =0.5 km; Inc=90°,Dec=45° *(Figure 4.7)*.
- M-3 - Infinite block grown upward to 3 km depth, from 5 km start;
  a - Inc=90°,Dec=45° *(Figure 4.8)*.
  b - Inc=45°,Dec=45° *(Figure 4.9)*.

Type: P - Vertical prism-type inversion
N - Polygon-type (Talwani) inversion

Infer - Indicates which convergence criterion was satisfied:
0-No convergence criterion was satisfied
2-Difference in $\Sigma\,(\text{residual})^2$ on two successive iterations was $< \epsilon$

IER - Output error parameter:
39-Marquardt parameter, μ_n, exceeds the maximum
133-Maximum number of function calls exceeded

NI - Number of iterations
Norm - The norm of the gradient
NSIG - The approximate number of significant digits in the solution vector
Marq - Final value of the Marquardt scaling parameter, μ_n
NC - Number of evaluating function calls

Table 4.1. Table listing aspects of idealized 2-D bodies used along with ZXSSQ convergence information resultant during gravity and magnetic least-squares inversions (for further reference, see IMSL manual). In the case of gravity models, results from *polygon*-type versus *prism*-type inversion techniques are easily compared.

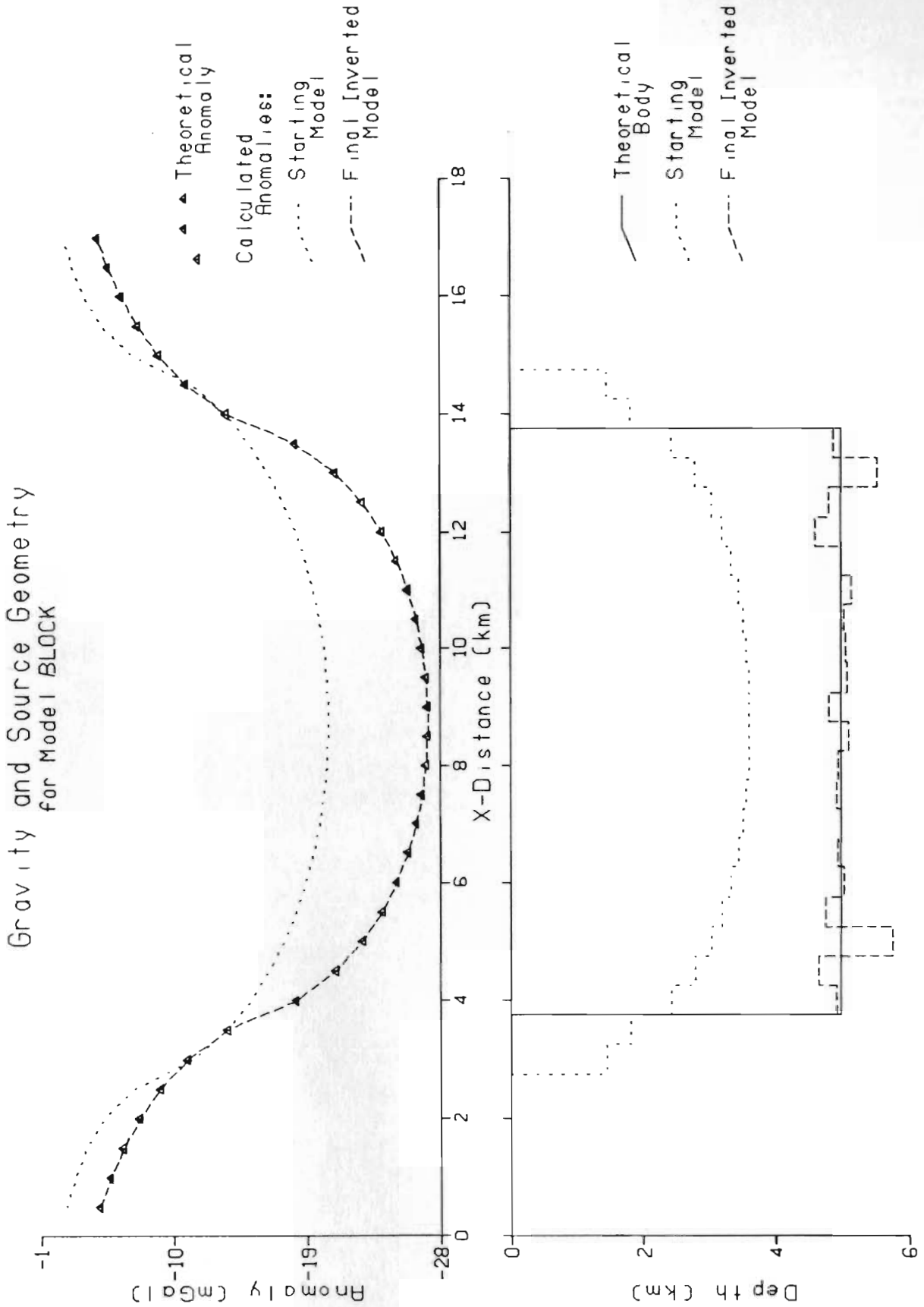

Figure 4.3. Results of applying a *prism*-type least-squares inversion to the gravity effect due to a vertically sided slab model.

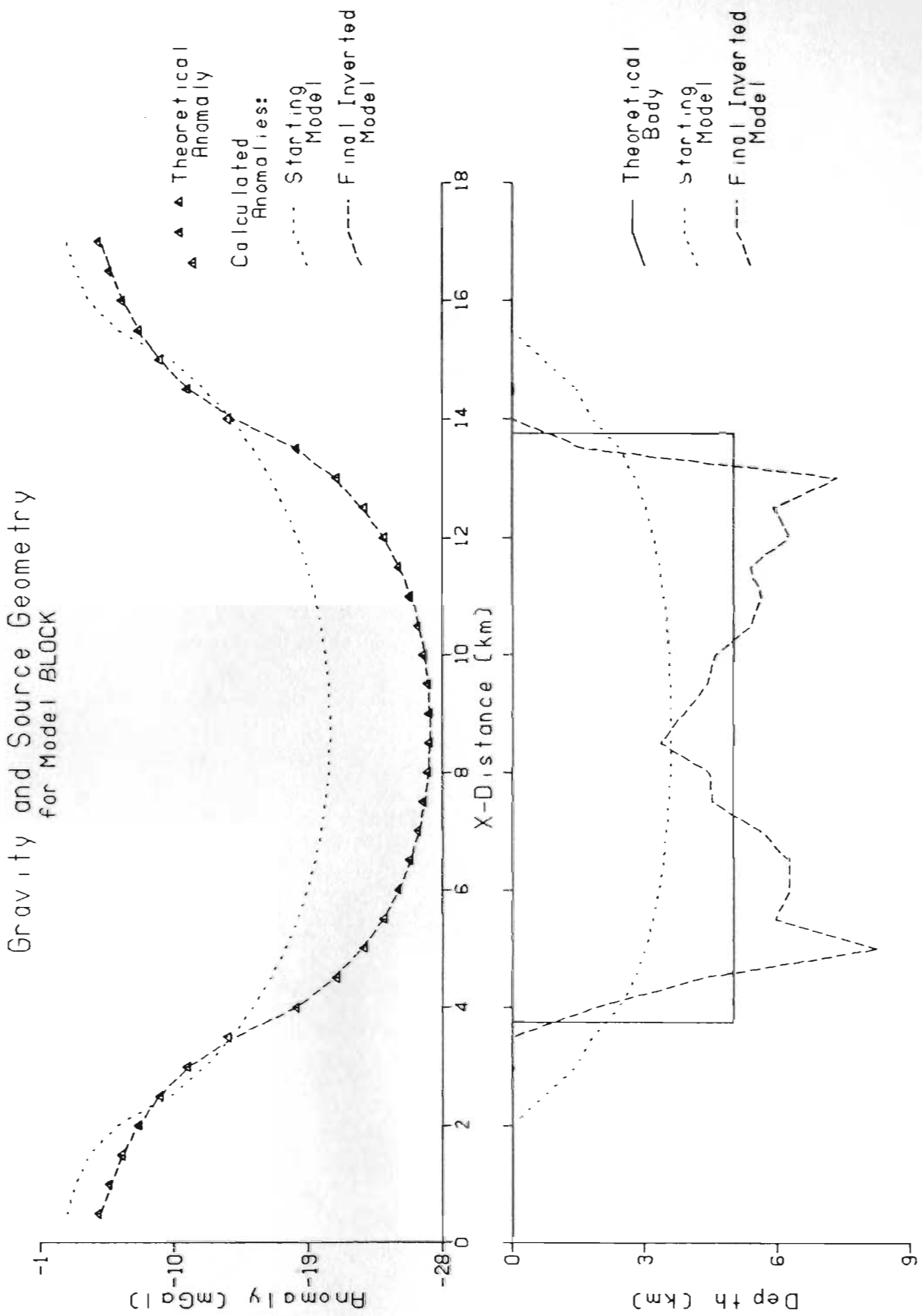

Figure 4.4. Results of applying a *polygon*-type least-squares inversion to the gravity effect due to a vertically sided slab model. (Compare inverted body to that of Figure 4.3).

The gravity effect of a vertically-sided 5 km thick slab of negative density contrast beginning at the surface was found best inverted by the prism-type inversion scheme (Figure 4.3). The polygonal body inversion (Figure 4.4) displays some of the Gibb's effect of side-lobing similar in character to phenomena observed by Peavy (1985). In this case, side-lobes arise from inability to fit polygon coordinates equally spaced in X to the vertically sided theoretical body. Despite the oscillatory nature of the resultant body, the total area enclosed by the polygonal body cross-section equals that of the source model. It is also noteworthy that the free body coordinates rapidly fall to zero outside the theoretical body. If these coordinates were not constrained to be positive, the body would show additional negative side-lobes beyond either extreme of the theoretical body.

A sedimentary basin delimited by sides sloping inward at 45° from surface to a 3 km level defined a second model tested by these programs; results are displayed in Figures 4.5 and 4.6. In this case, the two methods performed similarly, but a hint of the side-lobes present in the cosine-bell weighted method of Peavy (1985) is present in the resultant model of polygonal cross-section (Figure 4.6). Although the two inversion schemes produced comparable z-parameters, the polygonal model is the more visually pleasing. A third model was constructed by burying the geometry of the sedimentary basin to a 2 km depth. In this case, the prism-type inversion outperformed the polygonal type. An upside down version of this last model, with outward sloping sides, when subsequently employed in the inversion, yielded similar results.

In comparing the two methods of the matrix inversion process (prism-type .vs. polygon-type) convergence to the starting model is in almost all cases swifter and more assured for the prism-type inversion. Generally, the greater the depth of approximated z-coordinates, the slower the convergence to the minimum and the more poorly determined are these parameters. Output from the polygon inversion indicates that its

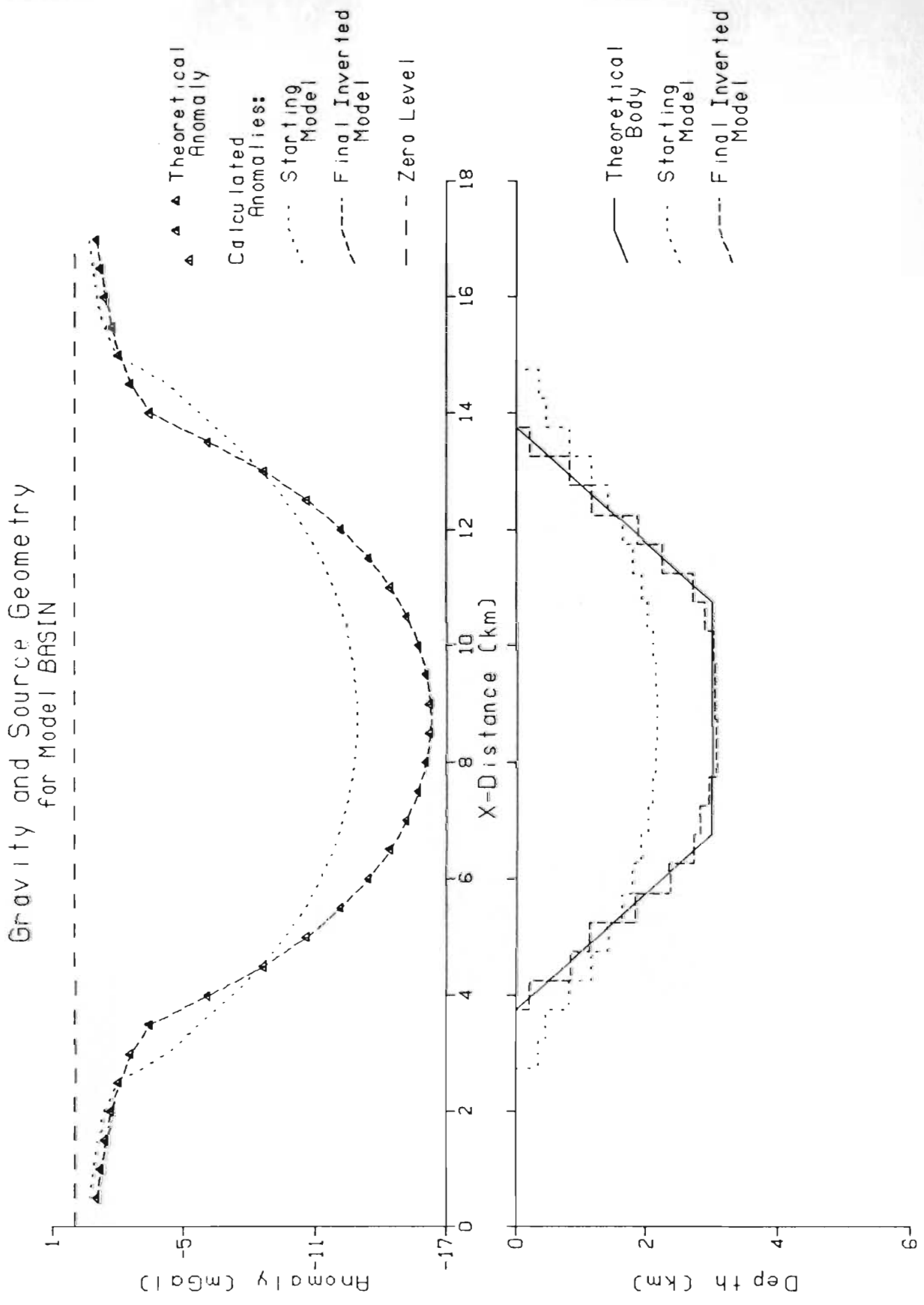

Figure 4.5. Results of applying a *prism*-type least-squares inversion to the gravity effect due to a sedimentary basin model having inwardly sloping sides.

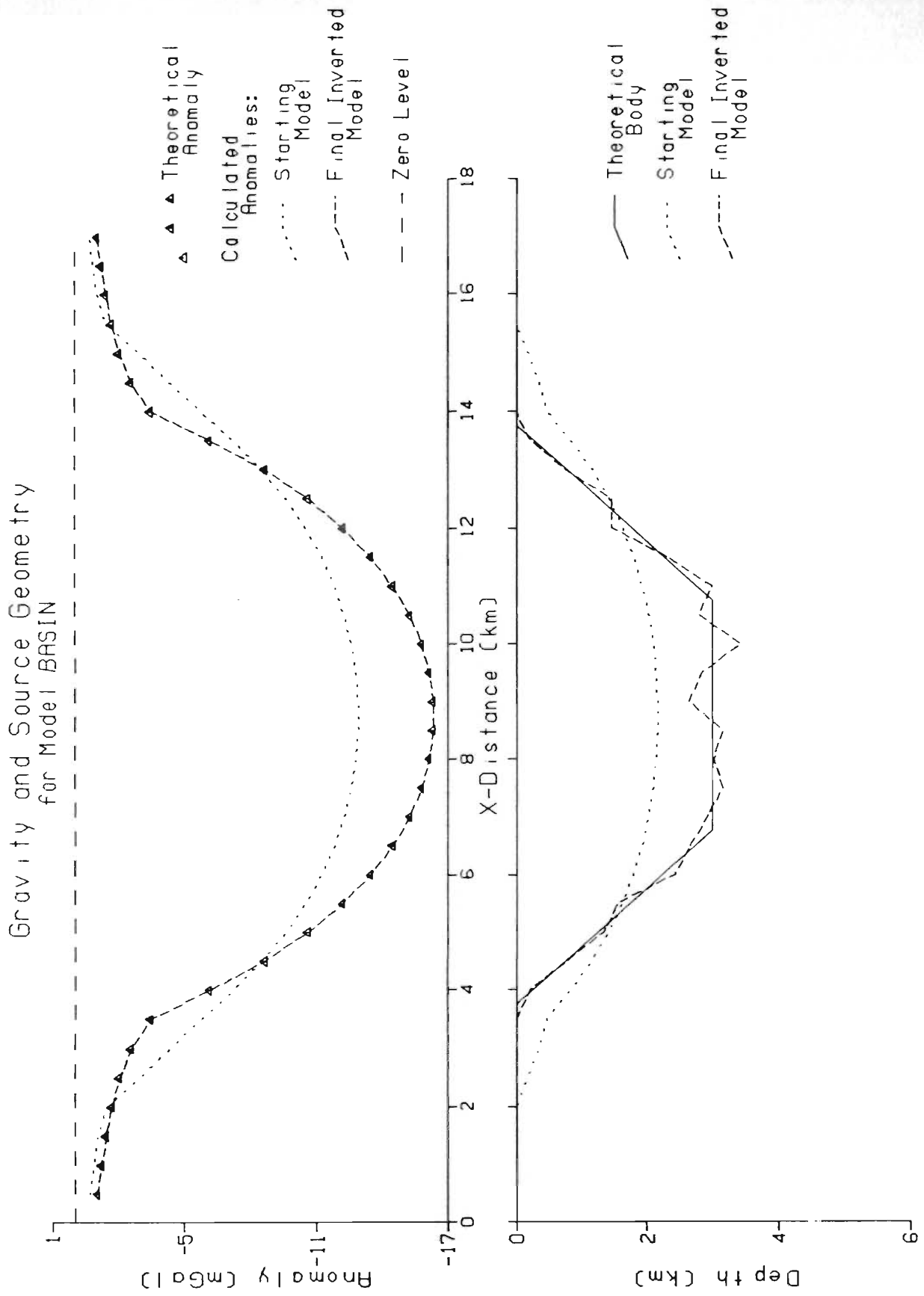

Figure 4.6. Results of applying a *polygon*-type least-squares inversion to the gravity effect due to a sedimentary basin model having inwardly sloping sides. (Compare with Figure 4.5).

parameter determination deteriorates at a greater rate with depth than do those of prism-type inversion. One reason may be that changing the variable z on any one of the polygon vertices, i, affects the mass distribution spanning the distance in x between the adjacent vertices to either side, a distance of twice the vertex spacing. By the same token, adjustment of either of the adjacent vertices, $i-1$ or $i+1$, alters the distribution out to the present vertex, i. In this sense, vertices of a polygon are all interwoven and interdependent. On the other hand, to shift a z-coordinate of an individual prism in a prism-type inversion affects only the mass distribution over the width of that prism, so that prism depths are relatively independent of each other. Certainly, the prism-type inversion is the superior in modelling steep gravity gradients or for models where steeply dipping to vertical sides are expected. Formulae describing the gravitational effect of a vertically sided prism possess less nonlinearity than corresponding relations for the Talwani-type polygonal body.

4.3.2. Magnetic Inverse Modelling

As in the case of gravity modelling, two approaches to inverting magnetic data were explored: inversion based on a series of vertical prisms and Talwani-type inversion based on bodies of polygonal cross-section.

Evaluating functions describing the total field magnetic response from vertical two dimensional and 2.5-D (infinite and finite length, respectively) prisms were constructed on the basis of a double application of equation (3.53) from Telford *et al.* (1976) and corresponding equations from Bhattacharyya (1964), respectively. Both routines were optimized in the manner described in Kunaratnam (1981). Because of its computational speed advantage, the 2-D version was used to test an inversion scheme for a magnetically induced subsurface block. As a theoretical model, a 2-D block buried at 0.5 km, having a 3.0 km thickness and polarized in a vertical field, was adopted. Total field

anomalies from this block model were evaluated by the method of Talwani (1965) at "stations" spaced 0.5 km along the x coordinate, assuming no remanent magnetization and neglecting demagnetization. The fitted anomalies and source geometry was evaluated by the ZXSSQ inversion routine are displayed in Figure 4.7. Convergence was rapid (Table 4.1) and the inverted results were very close to the solution, even for cases where the starting model was far from the derived minimum. It may be noted in Figure 4.7 that inverted prisms have depths most variable in the center of the body rather than near the body edges, as is the case with gravity inversion (Figure 4.3). This phenomenon is thought to result from the vector nature of the magnetic field, being most highly constrained near the body margins and much less so over the body center, where gradients are comparatively diminished. Although evaluating functions for the magnetic responses from 2-D and 2.5-D polygon-type bodies were constructed (Talwani, 1965; Rasmussen and Pedersen, 1979), these routines were found to be nonconvergent on implementation. Even when beginning from models very close to the theoretical solution, routines based on the magnetic responses of bodies described by polygons in cross-section caused ZXSSQ to terminate with error messages.

A depth-to-basement evaluating function was written from equation (3.53) of Telford *et al.* (1976) for the magnetic effect of a vertically-sided 2-D prism whose top is at depth z and base is at infinity. Results of an inversion performed on data from a infinite vertical prism of 10 km width and buried to 3.0 km is displayed in Figure 4.8. The method is very robust and convergence is most rapid when starting from a level deeper than the actual depth of burial (Figure 4.8), although similar end results evolve from shallower starting levels. Depth estimates are most variable in the central portion of the body when the inducing field is vertical. Data from inclined fields evolve models having most variable depths near the body edges as may be observed in Figure 4.9. It

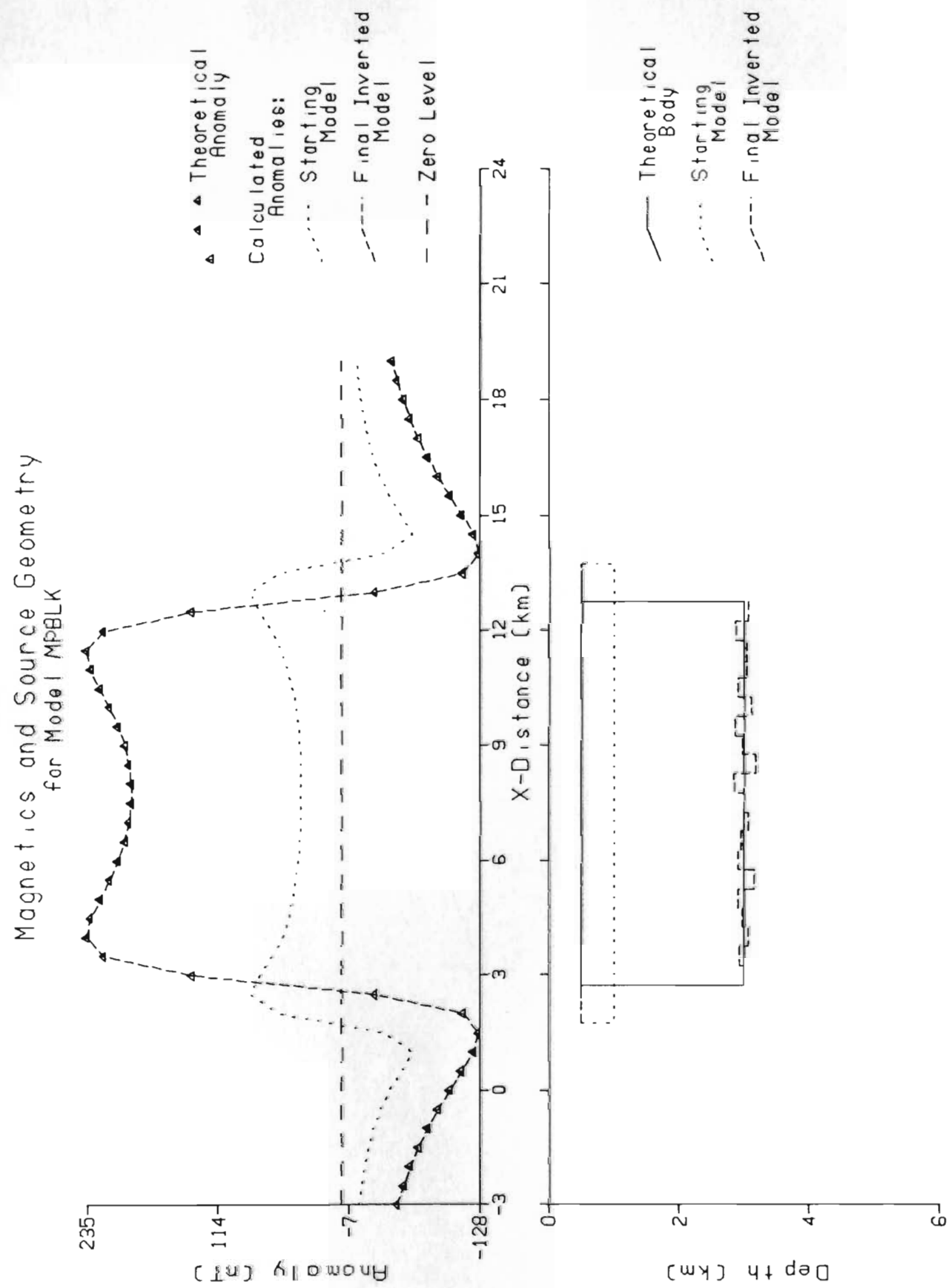

Figure 4.7. Least-squares *prism*-type magnetic (2-D) inversion results for a vertically sided block (finite prism) model buried to 0.5 km in the presence of a vertical inducing field.

appears that inversions of magnetic data produce most variable depth to magnetic basement estimates in regions where the anomalous field shows least gradients. Conversely, the most reliable depth estimates are associated with regions of steep magnetic gradient. This sensitivity of the solution to magnetic gradients implies that development of more sophisticated routines, which employ additional observed horizontal and/or vertical magnetic gradient information as constraints, would ensure efficient and accurate convergence to a local minimum of desired body parameters.

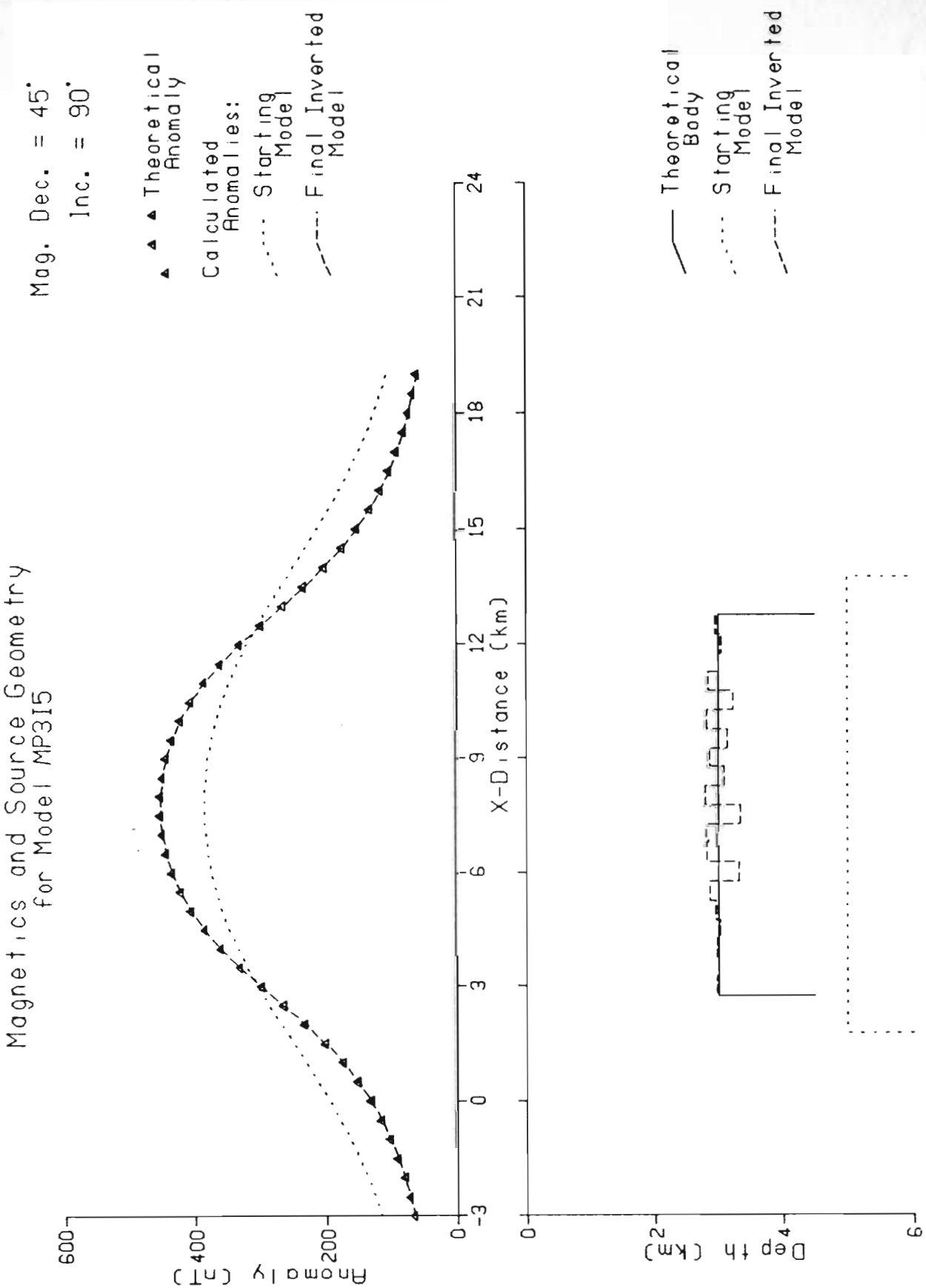

Figure 4.8. Least-squares *prism*-type magnetic (2-D) inversion results for a infinite vertical prism model buried to 3.0 km and induced by a vertical field.

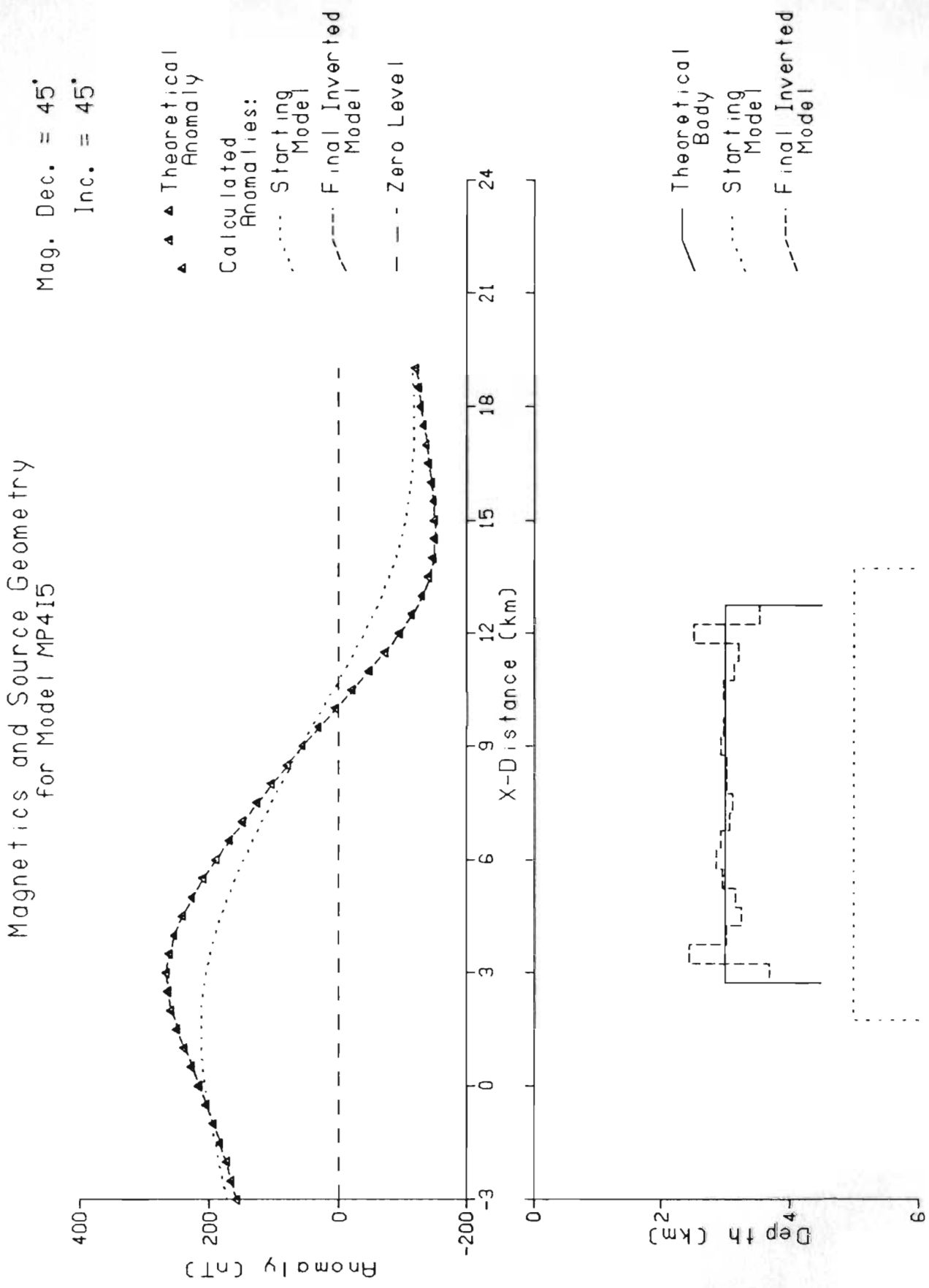

Figure 4.9. Similar to Figure 4.8 but in the presence of a field inclined at 45°. Notice that the most variable evolved depths in this case are situated near the body extremes.

5. Geophysical Interpretation

5.1. Qualitative Interpretation

5.1.1. Interpretation of Gravity Data

All gravity data available for the present study are posted as Bouguer anomalies and contoured in Map 2 as a foldout. Of the features on this map, the most noticeable are the linear trends, strongly reflecting the dominant northeast structural trend and the subsidiary eastward trend. As well, a minor northward trend is weakly expressed. A broad closed positive anomaly associated with the southern Port au Port Peninsula trends eastward. Positive values on the flanks of this high extend into the offshore to the southeast, with values decreasing systematically in that direction. Contours pass smoothly across the onshore/offshore boundary along the southern coast of Port au Port and near Stephenville, indicating a consistency within the two data sets. Contours are generally smoother in the offshore due to sparser data sampling.

The predominantly carbonate rocks of the Lower Paleozoic on the Port au Port Peninsula are relatively undeformed (Schillereff and Williams, 1979) with bedding dipping or plunging moderately north to northwestward. The lowermost carbonate units in the sequence are of higher density than the assumed normal crustal density of 2.67 gm/cm^3. The high Bouguer anomaly values observed along the southern coast of Port au Port reflect both the presence of these rocks and the proximity to surface of the underlying Grenville 'basement' rocks of Steel Mountain Complex affinity, which have a positive density contrast of approximately $+0.06 gm/cm^3$ (Peavy, 1985) relative to normal crustal rocks. The positive gravity gradient in northward transects across the Port au Port Peninsula may be explained by a thickening of Early Paleozoic carbonates with a partial contribution from a possible positive gravity gradient caused by the underlying Grenville rocks. A similar gravity gradient increasing eastward is observed entirely

within Grenville rocks in the Northern Peninsula to the north of the study area (Williams, 1979) (Gravity Map series).

A linear defined by steep gravity gradients trending northeastward parallel to the Long Range Fault delimits the southeastern boundary of the subbasin onshore. A belt of gradients similar in appearance parallels the southeast coastline of St. George's Bay, suggesting that a fault subparallel to the Long Range is defining the coastline orientation. Gradients along this trend are observed to steepen to the northeast and the fault trend swings more northerly in the vicinity of Flat Bay. At 5330.N UTM, the gradient changes direction as trends turn eastward, correlating with the east-trending northern limit of the Anguille Anticline as defined geologically. The Bouguer contours are indented about 5 km here over the St. David's Syncline in a curve that swings back toward north to follow the coastline again just to the northeast.

Onshore, several anomalous gravity features may be directly correlated with known structural geology. The Anguille and Flat Bay anticlines show closed gravity highs relative to the field over surrounding rocks, and the St. David's Syncline is associated with a large intervening gravity low. A northeast trending belt of gravity gradients follows the surface trace of Crabbes Brook Fault, separating the high gravity values of the Flat Bay Anticline to the northwest from the lower anomaly values to the southeast associated with thickened sediments of the Barachois Synclinorium (Peavy, 1985). Thus, the Flat Bay Anticline shows steep gravity gradients to either side, suggesting that it has a strong fault-bounded character.

In contrast, the Anguille Anticline shows steep gradients to the west but those to the east are much gentler. This is consistent with the asymetrical nature of sediment bedding orientation of comparatively steep dips on the western limb of the Anguille Anticline becoming vertical to overturned to the southwest of exposure. Only faults

having minor vertical displacement are mapped to the immediate east of the anticline core. Anomaly values decrease to the southeast of the Anguille high, becoming most negative in a trough adjacent to the Long Range Fault. This trough correlates with an interpreted fault-bounded thickened sedimentary wedge in which upsection sediments of the Codroy Group appear as outcrop; rocks of the Searston Formation of the Barachois Group outcrop in the southeast extreme of exposed subbasin (Knight, 1983). The lower Mississippian Anguille Group sediments are likely confined to the relatively narrow belt of their surface outcrop onshore in the subbasin (Belt, 1969).

Overall, increasing negative Bouguer values correlate with inferred and interpreted thickened sedimentary sequences. Superimposed on this general picture are elongate and bull's-eye gravity lows. Several anomalous 'low' features have been drilled to reveal evaporite sequences of the Codroy Road Formation, while others have been identified and inferred to also be salt-cored (Knight, 1983; Peavy, 1985).

Offshore, as mentioned above, increasingly negative Bouguer values are encountered in transects oriented southeastward from the Port au Port Peninsula, where contours generally following the subbasin strike. This implies a steadily thickening sequence of sediments and basin deepening as the southeast coastline is approached, an area where some of the most negative Bouguer anomalies for the subbasin are situated. Gradients noticeably steepen in the inner bay area as contours curve gently northward to intersect the coastline at right angles near Stephenville. The curvilinear trend thus defined parallels the broader structural trend that wraps around the Grenville promontory east of Stephenville.

At the western margin (at about 325E UTM) Bouguer anomaly contours swing sharply north defining a moderate gradient decreasing to the west, and indicating the presence of a fault trending north-northeast nearly parallel to and merging with the

northwest Port au Port coastline. Contours are more widely spaced defining a much gentler gradient to the west of 315E UTM.

As observed onshore, the smooth contours describing the offshore gravity field are interrupted locally by large amplitude, northeast trending, low troughs, here interpreted from seismic evidence and by analogy with similar interpretations (Watts, 1972) as caused by elongate evaporite structures within thickened Codroy clastic sequences. The most prominent of these lies just offshore from the Anguille Mountains and is defined by steepened gradients to either side. Contour trends would suggest that the underlying structure swings onland and terminates at the St. David's Syncline, where the most negative Bouguer anomaly (-29.5 mGal) recorded in the subbasin is posted.

A second evaporite structure is identified between UTM coordinate pairs 325E, 5345N and 300E, 5330N. Contours are indented eastward from their northward linear trend, to curve around the northeast abrupt end of this structure. Increasing negative Bouguer values and less steep gradients flanking the feature to the southwest suggest a plunge in that direction. However, lateral gravity data control is not sufficient for accurate definition of this body. An easterly trending weaker distortion of contours is observed in the central offshore area beginning near 335E and 5350N UTM and continuing toward a low anomaly onshore at Flat Bay. Finally, a broad gravity low trends northeastward from Flat Bay to Stephenville and continues onshore for a distance before terminating in steep gradients. Again, lateral control here in the near-shore is poor, but gradients appear to be very steep to the southeast along the suspected offshore fault.

In attempts to enhance features present on the Bouguer anomaly map, a regional-residual separation was undertaken. As observed visually and discussed previously, the regional field becomes progressively negative to the southeast in the offshore, indicating that it is caused by a general thickening of sediments. Removal of a low-order regional

field described by a least-squares fit through all data points strips away most of the anomalous gravity effect arising from deep-seated or intra-basement features as well as the longer wavelength portion of the field arising from general basin geometry (ie. that due to a blanket of sediment having a thickness approximating the average subbasin depth). Highs in the residual field correlate with larger wave-number basement topographic highs and residual lows reflect locallized thickening sedimentary accumulations or the presence of sediments or evaporites of anomalously low density. Using the program as discussed in Section 3.3, trend surface and residual map pairs were generated for polynomial orders 3 through 8. Successively higher orders of least-squares data fits contain features of increasingly shorter wavelength. Upon careful inspection, a 5^{th} order polynomial fit was chosen as giving a reasonable representation of the regional field while enhancing residual features. A map of 5^{th} order residuals for Bouguer anomalies is included as Map 4 of the map-holder. Much of the contour sinuousity observed on Map 4 is an artifact of regular gridding and the light smoothing applied during map production. Further smoothing was found to be at the expense of high amplitude features. Where Bouguer anomaly lows are sandwiched between highs, such as between gravity highs associated with the Anguille Anticline and the Long Range Complex rocks, their amplitudes have been exaggerated during regional removal due to the long wavelength nature of the low-order polynomial fit.

Several of the features and trends delineated by the Bouguer anomaly map, Map 2, are enhanced on the gravity residual map, Map 4. Large amplitude positive residuals are associated with the Flat Bay and Anguille Anticlines. These are separated by a cross-cutting negative trending east and associated with St. David's Syncline. A linear trend may be followed eastwards from the offshore along the northern margin of the Anguille Anticline. The Flat Bay high joins with the Indian Head Complex to form a 'ridge' on

the residual map. To the southeast, the Barachois Synclinorium is associated with a broad negative, which reaches maximum amplitude near the Long Range Mountains to the southeast. A large amplitude circular low at 380E 5335N UTM outlines an interpreted evaporite feature, the discussion of which will be reserved for later sections.

Other negative residual features onshore are associated with outcrops of Codroy Group strata, particularly that observed in the vicinity of Round Valley (350 E and 5315 N). The trough of Mollichignick and Overfall Brook members of the upper Codroy Group, located adjacent to the Long Range Fault (Units 8c and 8d, Map 1) correlates with the location of an elongate gravity residual low. Nearly circular, negative residual features, located near Codroy in the extreme southeast of the Carboniferous exposure, correlate with Searston Formation outcrop and may be due, in part, to underlying evaporite structures. The broad negative residual to the east of the Indian Head Complex (maximum anomaly at 413 E and 5378 N) is located over thick glacial overburden underlain by extensive Carboniferous sediments, considered Codroy in age (Knight, 1983; Williams, 1985). The positive residuals along the Long Range Complex are of very large amplitude on the residual map due to the attendant steep gravity gradients which are poorly described by a low order trend surface.

The positive anomaly associated with the Port au Port Peninsula is situated over the peninsula's southern coastline on the residual map, and is flanked to the southwest by a broad east-west oriented negative anomaly. These negative Bouguer values are interpreted in this study as resulting from a thickened sequence of sediments to the north of an east-trending fault discussed in the section on seismic interpretation (Section 5.1.3). The offshore salt-cored anticlinal structures discussed earlier are noticeably enhanced on the residual map. The most prominent negative gravity residual feature on Map 4, situated just offshore from and northwest of the Anguille Mountains, shows the

dominant northeast trend as it appears to parallel the Snakes Bight Fault and merges onshore with St. David's Syncline. The magnitude of Bouguer anomaly and the steepness of symmetrical gravity gradients flanking this feature indicate the presence of a thickened linear accumulation of low density evaporites in the sedimentary section at this locality. Two local minima occur along the length of the feature, one coincident with St. David's Syncline; the other, located at 325 E and 5325 N, corresponds with a widening of the feature, probably resulting from greater depth of source(s).

A series of three smaller isolated gravity residual lows, located between coordinate pairs 301E, 5331N and 320E, 5342N near the western data boundary are aligned in a northeast direction parallel to the elongate feature just discussed. The greater breadth and lesser magnitude of this series of lows is interpreted here to the result from a smaller linear accumulation of low density evaporites at depth. This feature is terminated in a region of eastward gradient by an interpreted (from seismic evidence) east trending strike-slip fault, displacing the sedimentary section and the basement at depth.

A similar elongate residual gravity low feature of lesser magnitude, located in the central bay region (at 348E, 5351N UTM), is well defined to the west, but shows poor contour closure eastward (Map 2). As discussed earlier, this is largely due to its superposition amid generally increasingly negative Bouguer values eastward in the direction of the broad gravity low situated northwest of Flat Bay. If the latter feature is related to evaporite accumulations, as steep gravity gradients on its margins suggest, planar to bedded deposits would be expected, in contrast to other evaporite features in the subbasin.

In a geophysical study of the East Magdalen basin, Watts (1972) attributes large amplitude negative gravity anomalies to lateral density variations within the Late Mississippian sediments, namely evaporite structures. Near-circular negative anomalies are

ascribed to salt diapirs, while those of elongate shape trending NE are interpreted as caused by evaporite cored anticlines, by analogy to those found in southern New Brunswick and in Cape Breton. Most short wavelength gravity low features in the present study area may be interpreted in terms of one or other of these two categories. Generally, elongate gravity lows have the larger amplitude. A gravity low centered at 328E, 5293N UTM, near the Long Range Fault in the south onshore, shows a character intermediate between the two end members. However, the anomaly is well defined only along its length by the Weir (1971) dataset, with little other lateral definition. Interpretation of this feature as a salt-cored structure is in agreement with a similar postulation of a study by Hooker Chemical Corporation reported in Knight (1983).

A broad Bouguer anomaly low located just north of Flat Bay and west of Stephenville appears very similar in shape and orientation to "gravity 'low' A" on Fig. 3 of Watts (1972) which is attributed to thick planar evaporite accumulations in Mississippian age strata. The low in the present study area differs in that it is superimposed on a less negative background level, a result of substantially shallower basin structure.

The gravity expression of subsurface configurations of source rocks for negative anomalies is complicated by the fact that the thicker evaporite sequences tend to occur near basement faults as these are zones of structural weakness and/or maximum sediment deformation. Therefore, negative evaporite-related gravity anomalies are in places superimposed on less steep gravity gradients associated with faulted blocks. Such superposition of gravity signals can, in certain cases, complicate the identification of faults.

5.1.2. Magnetic Data Interpretation

Since the magnetic susceptibilities of the Carboniferous sedimentary rocks within the Bay St. George subbasin were found to be lower than the detection limits (Peavy, 1985), the map of filtered total field magnetic data (Map 3) reflects the relative orientations and depths of magnetic Indian Head-type basement blocks. Lenses of magnetite-rich rocks similar to those reported present within the more mafic members of the Indian Head Complex (Williams, 1985) and modelled by Peavy (1985) are considered to be the probable cause of the variability of patterns of large magnitude anomalies observed on magnetic maps for the area. The field contours of Map 3 represent two phases of averaging: an averaging applied directly to the data during the digitization and subsequent filtering, and that performed during contour generation by the computer. As a result, the map is weighted toward long wavelength features at the expense of short wavelength features due to sources in the near-surface.

The most prominent feature on Map 3 is the nearly linear series of high values located to the southeast of the Long Range Fault, associated with Precambrian mafic rocks known to outcrop there. This northeastward contour trend is interrupted and shows eastward offset at about 5325 N UTM, near the southern extent of the Barachois Synclinorium. However, the northeast trend is maintained and contours are displaced westward at about 5350 N UTM to again coincide with the subbasin margin of Long Range rocks further north. This magnetic 'ridge' is flanked on its northwest side by a series of low amplitude magnetic negatives as would be expected in these intermediate latitudes (magnetic inclination $\approx 72^\circ$). The magnetic offset along the Long Range Fault may arise from a lateral lithologic change within the Long Range Complex rocks, resulting in a local relative deficiency in magnetic composition. Alternatively, magnetic rocks of the Long Range Sequence may have been thrust westward such that lower magnetic

5.1.2. Magnetic Data Interpretation

Since the magnetic susceptibilities of the Carboniferous sedimentary rocks within the Bay St. George subbasin were found to be lower than the detection limits (Peavy, 1985), the map of filtered total field magnetic data (Map 3) reflects the relative orientations and depths of magnetic Indian Head-type basement blocks. Lenses of magnetite-rich rocks similar to those reported present within the more mafic members of the Indian Head Complex (Williams, 1985) and modelled by Peavy (1985) are considered to be the probable cause of the variability of patterns of large magnitude anomalies observed on magnetic maps for the area. The field contours of Map 3 represent two phases of averaging: an averaging applied directly to the data during the digitization and subsequent filtering, and that performed during contour generation by the computer. As a result, the map is weighted toward long wavelength features at the expense of short wavelength features due to sources in the near-surface.

The most prominent feature on Map 3 is the nearly linear series of high values located to the southeast of the Long Range Fault, associated with Precambrian mafic rocks known to outcrop there. This northeastward contour trend is interrupted and shows eastward offset at about 5325 N UTM, near the southern extent of the Barachois Synclinorium. However, the northeast trend is maintained and contours are displaced westward at about 5350 N UTM to again coincide with the subbasin margin of Long Range rocks further north. This magnetic 'ridge' is flanked on its northwest side by a series of low amplitude magnetic negatives as would be expected in these intermediate latitudes (magnetic inclination $\approx 72^\circ$). The magnetic offset along the Long Range Fault may arise from a lateral lithologic change within the Long Range Complex rocks, resulting in a local relative deficiency in magnetic composition. Alternatively, magnetic rocks of the Long Range Sequence may have been thrust westward such that lower magnetic

Another prominent feature on the magnetic map is a large amplitude high located over known outcrop of Indian Head anorthosite in the core of the Flat Bay Anticline. Contours here follow the general trend of structure mapped at the surface. A series of high frequency elongate magnetic anomalies trending north to northeast over the Flat Bay Anticline are reported in an early aeromagnetic survey by Scott and Evans (1952). To the northwest of the Flat Bay anomaly, gradients are very steep as would be expected from a near-surface magnetic block fault-bounded on its northwest margin. The Flat Bay magnetic anomaly is also flanked and separated from similar Indian Head rocks to the north by very steep gradients, indicating that the basement is similarly down-faulted along the anticline's northern margin. Contours swing eastward along the northeast of this anomaly to include an anomaly of lesser magnitude associated with the Steel Mountain anorthosite of the Long Range Complex. The Flat Bay anomaly shows largest values at 5355N UTM, immediately to the east of Indian Head outcrop in the anticline core. A somewhat weaker anomaly located at 5340 N and 400 E UTM south of Steel Mountain correlates with outcrop of Indian Head rocks at Mount Howley. This implies that sediment cover is not extensive over a basement ridge joining the two outcrops.

The Flat Bay anomaly is bordered to the southeast by a broad low that extends eastward to merge with the negative trough flanking the Long Range Mountains. The gradient to the southeast quite closely correlates with the Crabbes Brook Fault (Knight, 1983) which separates the relative basement high underlying the Flat Bay Anticline from magnetic basement at greater depth beneath the Barachois Synclinorium. The Flat Bay anomaly is observed to taper off gently to the southwest consistent with the interpreted southward anticlinal plunge and extends to the northern extent of lower Anguille outcrop (5330 to 5335 N), where it terminates in negative gradients.

A magnetic anomaly of lesser magnitude and gentler gradients is associated with outcrop of the Indian Head Complex to the northeast of Stephenville. The implication is that these rocks differ from those of the Flat Bay Anticline core to the south in having lower magnetic susceptibilities and/or sources at greater depth. Variable composition within the Indian Head Complex was reported by Williams (1985) within the more massive units of the southern outcrop and near Indian Head at the southern extent of the northern outcrop (Murthy and Rao, 1984). Presumably gabbroic rocks to the south have a higher mafic or magnetite content than the finer grained layered diabases to the north, the former possibly representing rocks originating from deeper within the complex. The northern Indian Head magnetic anomaly is defined to the east by a negative eastward gradient, interpreted as due to Carboniferous sediments and overburden thickening eastward.

It is noted that the Anguille Anticline does not show a magnetic character similar to that of the Flat Bay Anticline; rather, magnetic values become increasingly negative to the southeast across the onshore exposure of the Anguille Group to form a broad negative band adjacent to and northwest of the Long Range Fault. Magnetic basement can be interpreted to lie at considerable depth in this earliest basin, a point which is further supported by a negative southeastward gradient located just offshore coincident with the interpreted fault bounding the northwestern margin of the Anguille Group. A transition to deeper magnetic basement beneath Anguille strata is indicated. Such apparent deepening could result if Anguille sediments do not rest directly on magnetic basement, but upon an intervening sequence of rocks having non-magnetic character, such as a carbonate sequence.

A magnetic high 'ridge' is situated just off the south coast of the Port au Port Peninsula at 5375N and from 375E westward. The ridge originates onshore northwest of

Stephenville and shows a change in trend from southwestward onshore to westward offshore, roughly parallel to the coastline. As this magnetic high can be correlated onshore with proximity to surface of Grenville rocks, this apparent change in trend of the interpreted near surface Precambrian basement edge may be explained as follows:

Onshore, the carbonate sequences overlying Grenville basement have a gentle dip to the north or northwest. High-angle faults within the earlier Paleozoic rocks (comprising portions of the pre-Carboniferous basement in the subbasin) display consistent NNE strike and characteristically downthrow to the east whereas later faults displacing Carboniferous strata generally have their downthrown sides to the northwest. A series of faults cutting Early Paleozoic carbonate rocks of the Port au Port Peninsula (Map 1) conforms with the earlier fault pattern. Continued offshore as illustrated in Map 5, this fault geometry would systematically raise Precambrian rocks to the near-surface on the western sides. The upper surface of Grenville magnetic basement underlying Early Paleozoic carbonate rocks should then have a step-like nature, dipping gently northwestward but faulted upward periodically in a westward traverse across this magnetic ridge.

A lower amplitude, broader magnetic high in the Spector data situated farther west just off the tip of Port au Port at 340E, 5372N is interpreted in this study (also Spector, 1969) as arising from a deeper source.

Magnetic anomaly values indicate a north to northeasterly trend near 315E, 5335N UTM separating negative values to the west from positives to the east. The trend correlates with a similar trend observed on the map of Bouguer anomaly (Map 2) and earlier interpreted as caused by a fault with sense of throw down to the west or northwest. To the west of this feature, magnetic values are negative and relatively uniform, depicting a deepened basin in that direction. A broad positive magnetic feature of about 250 nT amplitude is observed to the east, in the center of the bay and north of the Anguille

Anticline (5345N and 340E). Its breadth suggests this anomaly arises from a source at depth, while its magnitude suggests high susceptibility and large dimensions. The extension or nosing out to the southeast may indicate either an extension of the body in this direction or the presence of a similar body of lesser dimensions. The expression of magnetic bodies in the offshore conforms with the general concept of a thickening subbasin to the southeast as interpreted from gravity data.

5.1.3. Seismic Interpretation

Despite the generally poor quality of seismic data, the stronger reflections were interpreted and traced across several sections. Appendix C contains line drawing interpretations of seismic reflectors on sections accompanied by the corresponding gravity profiles for correlation purposes. Gravity data are presented as profiles from the contoured Bouguer anomaly field with actual values for all stations within 5 km to either side of the seismic section locations included for unbiased reference. For seismic lines trending east-northeast, station values show largest variability and departure from the contoured field as these lines follow the sedimentary basin strike.

The most prominent reflector identified on most of the seismic sections (reflector R1 on all figures of Appendix C) is interpreted here as the pre-Carboniferous basement, rocks of probable Grenville age. Crystalline Grenville rocks were subjected to metamorphism during the Devonian Acadian orogenic event and therefore contrast sharply with the overlying, relatively undeformed Carboniferous strata. Two-way time picks to this basement reflector on seismic lines trending northwest-southeast indicate that the basin thickens in general monoclinally to the southeast. The southeastward dip of this reflector is interrupted locally by at least one high-angle normal basement fault trending east to northeast and (downthrown to the north) lending a blocky nature to the sub-basin (Figures 3.5, C.3, C.4, C.5). Near the northwest ends of southeast oriented seismic lines, where the basin shallows, the basement reflector loses its strong reflective character suggesting a possible intra-basement lithologic change. However, the presence of strong low-order water bottom reverberations introduces difficulty in interpretation of these early reflection arrivals. Basement picks on seismic lines trending east-northeast show very little dip on reflector R1, indicating that these lines are oriented nearly parallel to the basin strike as expected from trends observed on the Bouguer anomaly map. In the

offshore area covered by seismic data the basin structure is interpreted as that of a half-graben dipping toward the southeast Bay St. George coastline and striking subparallel to the Long Range Fault margin.

Due to the persistent peg-leg multiples and the large acoustic contrast at the Carboniferous-basement boundary, no reflectors can be traced beneath or within the pre-Carboniferous basement. However, subtle structure is evident within the Carboniferous strata. The next most prominent reflector, R2, is interpreted as the top of an evaporite sequence of Middle Codroy (or Windsor) age. It characterizes the general trend of Carboniferous sediments warped by movements of evaporite sequences mobilized under the influence of subsequently deposited thick upper section and basement block rearrangement (see Figure C.4), forming a series of subparallel anticlines and synclines whose axes trend parallel to the basin axis. The thickest sections of evaporites are expected in the nose areas of anticlines, where sediments have undergone the tightest folding and probable minor faulting within the Upper Carboniferous strata. The reflective character of the R2 horizon changes locally from being very strong on the flanks of anticlines to relatively weak and difficult to trace through the anticlinal hinge areas, as indicated on Figure C.7. Such phenomena would be expected from a change in reflector orientation from a concave "focussing" shape on the anticline flanks to a convex or divergent form near the hinge region, but also suggests that salt has flowed toward the hinge areas thereby altering the reflective character of the sediment-evaporite interface. If evaporites are near the surface, salt solution and subsequent downfaulting would be expected to complicate the structure over the anticlinal hinge. A coherent signal from the top of salt near hinge areas cannot be discerned among the first strong water bottom multiples in the upper section (as indicated by "?" on Figure C.7). Portions of sections identified as showing anticlinal structure can also be correlated with basement reflector

pull-up, further indicating a thickened evaporite sequence in the hinge regions. Beneath these salt accumulations the basement reflector often loses its characteristic strength, as also noted by Williams (1974) in discussing interpreted reflection seismic data from near the Magdalen Basin. Salt pillows in anticline hinges induce localized gravity lows which superimpose on the general trend of increasingly negative Bouguer values to the southeast in offshore data. The short wavelengths of salt induced features become especially prominent on residual gravity maps after trend removal. Correlation with gravity profiles during seismic interpretation is essential in the identification of the more subtle anticlinal structures on sections where seismic data quality is particularly poor.

The largest salt structure identified on the seismic sections is situated just off the southeast coast near St. David's Syncline. Interpretation of the intersecting lines E-20 and E-11 shows a massive salt body outcropping at or very near the present seabed in the core of the anticlinal feature (see Figures C.1, C.4). On line E-11, the salt core shows classic reflector pull-up but little other internal structure. Basement reflectors beneath the structure are impossible to discern. R2 reflectors on line E-11 indicate a dome-like tapering of the salt structure to the northeast but the structure is interpreted as terminating abruptly to the southwest by a fault identified as trending east-west. Departures of plotted Bouguer anomaly values from the contoured field displayed in Figure C.1 are due to their lateral distances from the seismic line and the steep gravity gradients in proximity to the anticline. Contours that outline a pronounced trough in gravity data, coincident with this evaporite feature, exhibit a subtle but definite westward jog south of this fault. The apparent smaller dome feature identified to the southwest of the fault on Line E-11 is thought to be a side-swipe phenomenon of a large domal feature located immediately west of this portion of the line, adding further support to the east-west dextral fault interpretation. If the two features are displaced portions of

the same structure as interpreted, estimates of both the relative timing and displacement magnitude of the fault may be obtained. The salt structure may be traced along its southwestward trend by the trough in gravity data. However, the portion of the structure identified on line E-11 may represent the most extensive accumulation along the length of the anticline. The occurrence of large negative gravity anomalies onshore near St. David's indicates a continuation of the evaporite structure eastward. The many small faults and divergent bedding orientations mapped in this area (Knight, 1983) imply a complicated structure.

Weaker reflectors above the Middle Codroy reflector also display the folded character of sediments. Several of the more coherent upper section reflectors were added as dashed lines to the section line drawings to show the general trend of sediments. These reflectors tend to be discontinuous laterally and cannot be easily correlated from section to section. The later arrivals of apparent upper section reflectors may actually be multiples from earlier arrivals or interference patterns of multiples with reflectors. Signal is strongest in the synclinal axis areas where reflectors are most concave, particularly where the primary reflected signal is in constructive interference with the strong water bottom reverberations. However, subtle reflections are traced through regions of steep reflector dip, distinguished on the basis of their oblique orientation to reverberated signal. A possible explanation for observed lateral discontinuity in upper section reflectors is the presence of alternating sandstone/shale sequences, a result of river channel lensing in the Upper Codroy Group section (Knight, 1984). From onshore exposures, it is evident that Carboniferous sediments are cut by numerous minor faults in addition to a few major faults. Similar minor faults in the offshore, related to the folding of clastic sediments, are responsible for much of the discontinuity in upper section reflectors.

Using picks of the basement reflector, R1, a two-way time structure map was con-

structed for most of the region covered by seismic data to evolve a picture of basement structure. The R1 reflector could not be identified with certainty on a few of the short lines or for complicated sections of other lines, such as Line E-11. Therefore the dataset of basement reflector picks is incomplete. The fault evident on Figure 3.5 is shown striking east-west on the interpretation map, Map 5.

Normal and strike-slip faults are mapped within Carboniferous strata of the southeast Maritimes Basin in Nova Scotia (Williams, 1974). Although both normal and strike-slip faulting exists in the Bay St. George subbasin, the latter is not readily identified on seismic sections, especially where little vertical displacement of the R1 reflector is recorded. However, features on seismic sections may indicate high-angle faulting expressed in the sedimentary section as laterally discontinuous reflectors, as on seismic line E-18, Figure C.3. When interpreted in conjunction with dextral offsets of features and contours of the gravity field (Map 2), these features apparently identify loci of strike-slip displacements. The several sub-parallel east trending strike-slip faults that have been identified in the present study (see Map 5) are likely reactivated faults or zones of weakness remanent from the pervasive Acadian orogenic event. Although movement along individual faults is not extensive, the cumulative displacement necessary to produce these faults has magnitude of significance. Discontinuity of Upper Codroy strata such as that observed to the southeast on Line E-18, and displacement of Codroy age evaporite cored anticlinal structures evidenced on the gravity maps suggest that a tectonic phase occurred at least as late as very late Codroy or early Barachois time, subsequent to Upper Codroy deposition offshore. The tectonic event is probably of Permian or later age, but timing remains uncertain as associated Permian or more recent basins have not been identified in onshore Newfoundland.

5.2. Quantitative Interpretation

In general, the structure of the subbasin has been interpreted within the framework of a northeast trending strike-slip basin opening (cf. Wilson, 1962; Bradley, 1982). Several features identified from the geophysical data support this mechanism. Models incorporating gravity and magnetic data were used to test agreement with proposed structure. Gravity data were modelled using the constraints of depth to basement determined from seismic as well as those imposed by surface geology. Because of the general consistency of features along the strike of the basin, 2-D forward modelling of blocks uniform in cross-section was used to approximate the structure to the accuracy required.

To ease the modelling process, transects were oriented along seismic lines (where possible) and the structure evident from seismic reflectors was used to constrain models. The quantitative interpretation is complicated by the fact that the negative effect of thickened sediment sequences is superimposed on a broad gravity positive over the entire basin offshore, presumably originating either from deep within the crust or from a fairly uniform thickness of Indian Head complex rocks in the shallow basement. Small changes in the density contrast of sediments may easily be countered by thickening of the underlying basement block or increasing its positive density contrast. Attempts at applying an inversion directly to the data failed due to the superposition of the various effects and incorrect assumption of uniform density contrasts throughout the subbasin. Application of a universal negative offset to account for the presence of the positive regional Bouguer anomaly from the basement block, likewise resulted in unrealistic inverted models, largely as a result of lateral variations in density contrasts among the various sections of the subbasin. Thus, a supervised modelling procedure, allowing user interaction was adopted.

Although the presence of salt structures contributes to the ambiguity always

inherent in gravity interpretation, removal of the effects of evaporites poses less of a problem, as such features are of short wavelength and readily show up on residual maps of higher order. During modelling of the evaporites, a density contrast relative to the sediments was used, so that the sediments could subsequently be modelled as a unit having a homogeneous density contrast relative to the basement rocks. Densities were assumed consistent with those measured and appearing in Table 3.3. Densities of the various blocks are included on the models.

The first step in modelling the gravity profile of seismic line E-20 was removal of the effects of large amplitude, short wavelength gravity lows due to interpreted local evaporite accumulation. The profile for the Bouguer field along E-20 accompanies the line drawing, Figure C.4. From this profile, a background or "regional" (see straight dashed line on gravity profile, Figure C.4) was chosen for the two anomalous features present. At the SSE end of this profile, where the Codroy Group is interpreted from magnetic and gravity data as being in fault contact with the Anguille Group, the anomalous portion due to the salt body was estimated as the curved dashed line drawn. Thus, the anomaly beneath the assumed background is attributed entirely to two distinct evaporite bodies as suggested by distinctive high structure on the R2 reflector of the corresponding line drawing. Using a density contrast of -0.3 gm/cm^3 (relative to sediments) and assuming two-dimensionality in structure these anomalies were inverted via the inversion routine discussed earlier. Bodies were allowed to develop upwards from basal depths, Z_o, of 1.5, 2.0 and 2.5 km, as the inversion results of Figure 5.1 show. The "observed" field is that digitized at 1 km intervals from the contoured field, and must be considered subject to the limitations of hand contouring precision, as well as those of observational accuracy and sparser sampling in the offshore. The unknowns or free parameters here were the heights of the body above the various reference levels, Z_o.

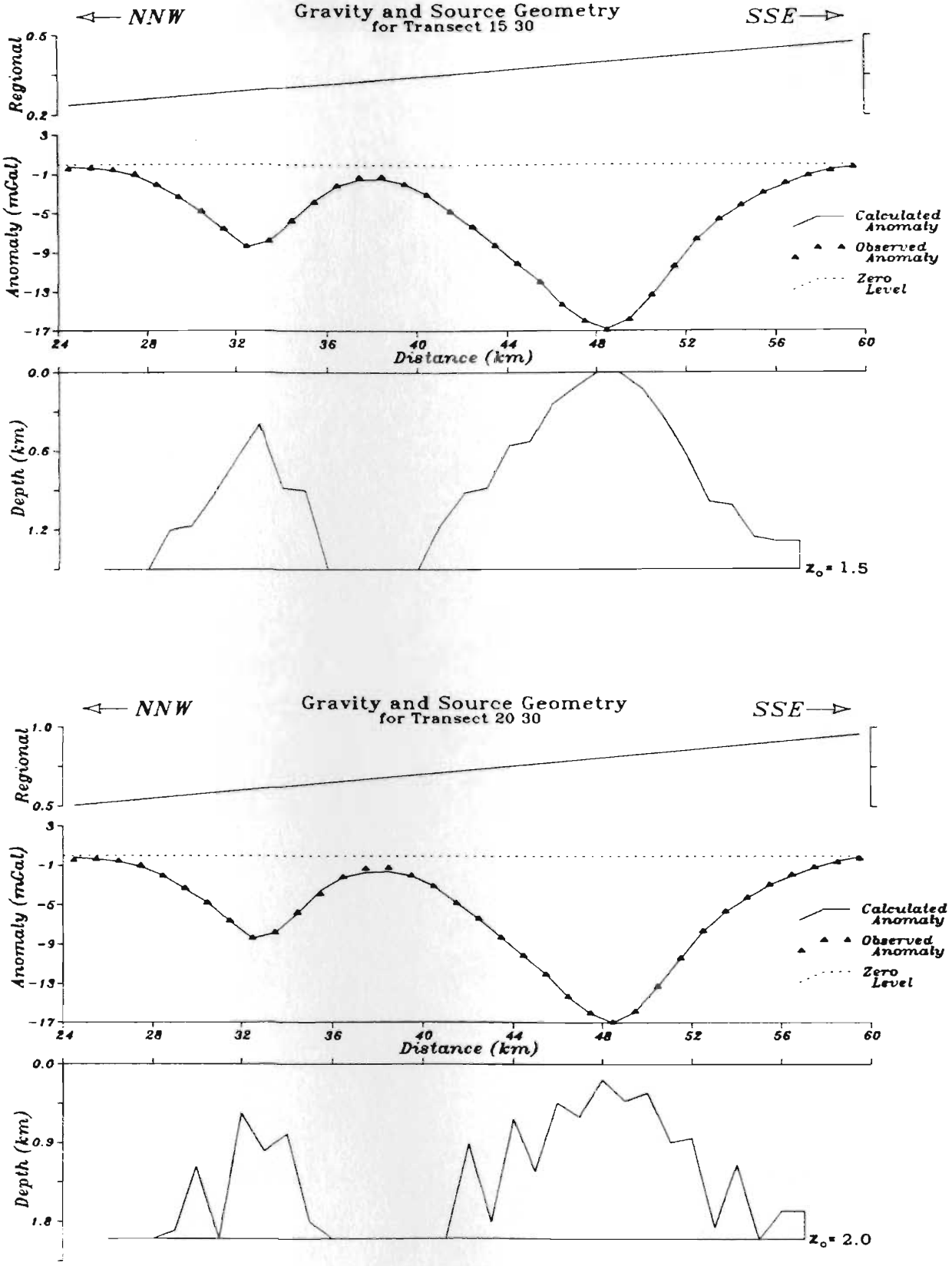

Figure 5.1. Results of inverting the portion of the gravity anomaly over transect $A - A'$ (Map 5) arising from interpreted salt structure. Bodies having a constant density contrast of -0.30 gm/cm^3 relative to sediments were evolved from successive basal depths, z_0 of 1.5, 2.0 and 2.5 km. Note increases in body complexity and evaluated regional with increasing depth of source.

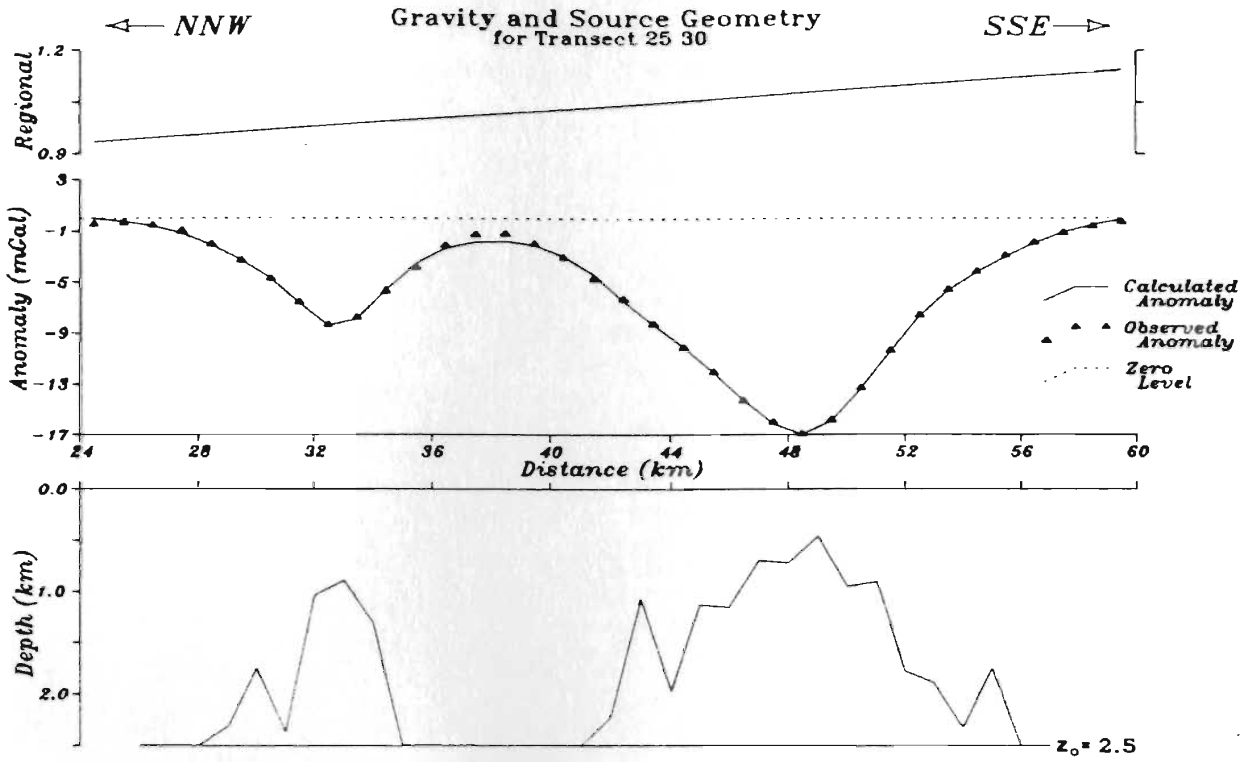

Figure 5.1 (continued).

Two additional free parameters were allowed during inversion to obtain a correction to the assumed regional field of the form $\Delta R = Ax + B$, ΔR being the inverted regional correction, and A, B the free parameters in units of mGal/km and mGal, respectively.

The seismically determined depth-to-basement provided constraints on the appropriate choice of lower reference levels. Figure 5.1 shows the models that develop from basal depths of 1.5, 2.0 and 2.5 km depths. As observed in Figure 5.1, incorrect choice of lower reference depths evolves models of unrealistic appearance and not conforming to the structure interpreted from seismic reflector orientation. The body grown from 2.0 km is particularly of unrealistic appearance. Regardless of the basal reference level chosen, inverted models produce similar corrections to the assumed regional. The evolution of the body inverted from a basal depth of 2.0 km from a starting model may be traced on Figure 5.2. It is noted that due to their linear dependence, the parameters describing the correction to the regional field, A and B, stabilize very early in the model development, by about iteration, $I = 4$. Because of its stronger dependence on the total anomalous field, the linear gradient portion of the regional, A, has converged by iteration 2, whereas the constant or d.c. term, B, does not converge until the body coordinates begin to exhibit stability. The inverted regional may be very sensitive to choice of starting body or model density, as the regional dependence aspect was not tested extensively. Nevertheless, from a cursory examination of the regional field results from various inversions (Figure 5.1), the regional shows little dependence on the chosen Z_o-level.

By iteration 3 or 4, a reasonable model has evolved; subsequent local perturbations develop under the requirements of improved data fitting imposed by termination tolerances. From the rapid convergence of r.m.s. residual values, R on Figure 5.2, and the increasingly oscillatory nature of evolved z- coordinates, it is noted that further iterations beyond $I = 4$ decrease the residual only marginally and at the expense of increased

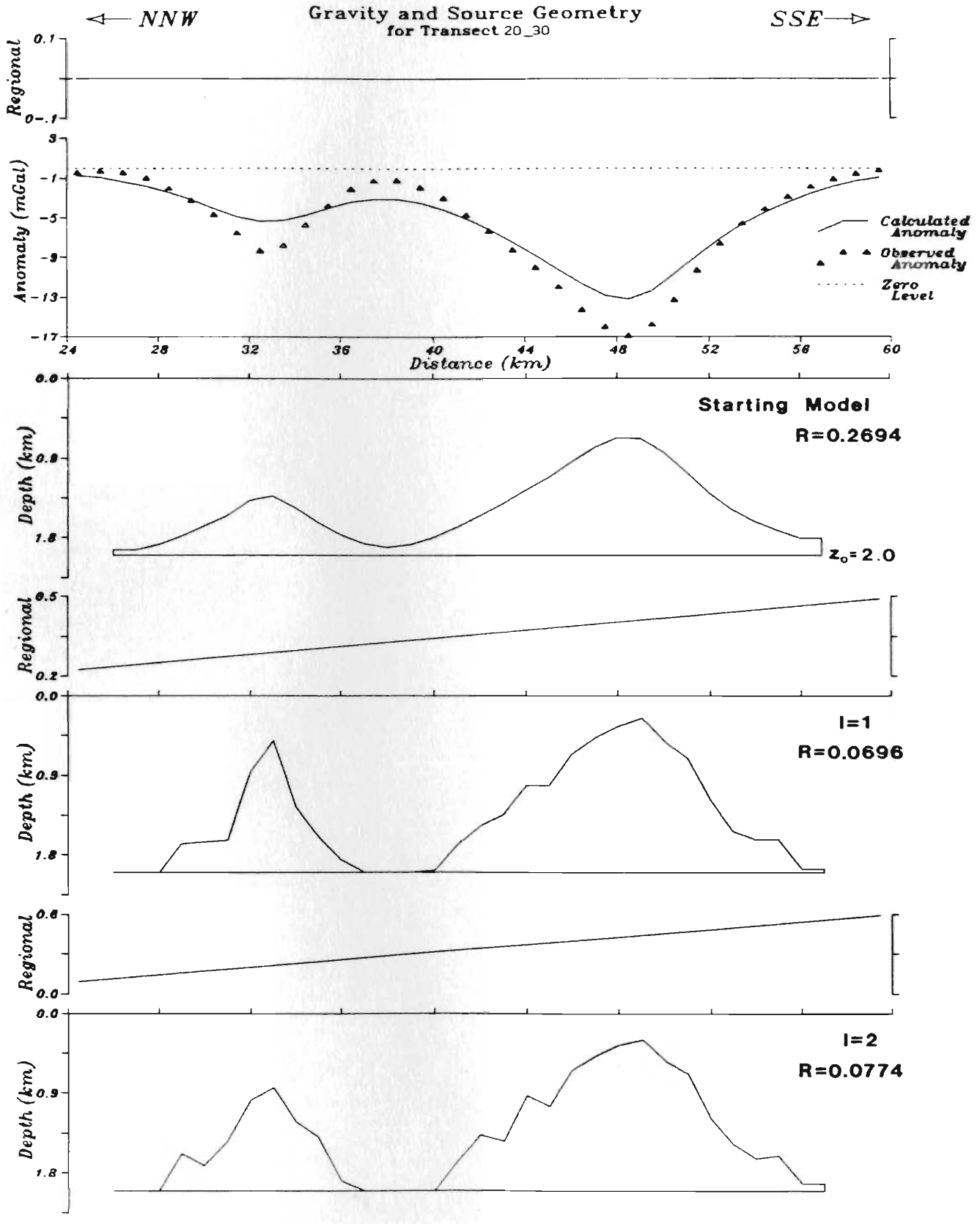

Figure 5.2. Evolution of the inverted body of Figure 5.1 evolved from a basal depth of 2.0 km. Upper diagram displays the initial model. The remainder shows the body after successive iterations, I. Values of R are the rms. residuals in the anomaly from each iterant.

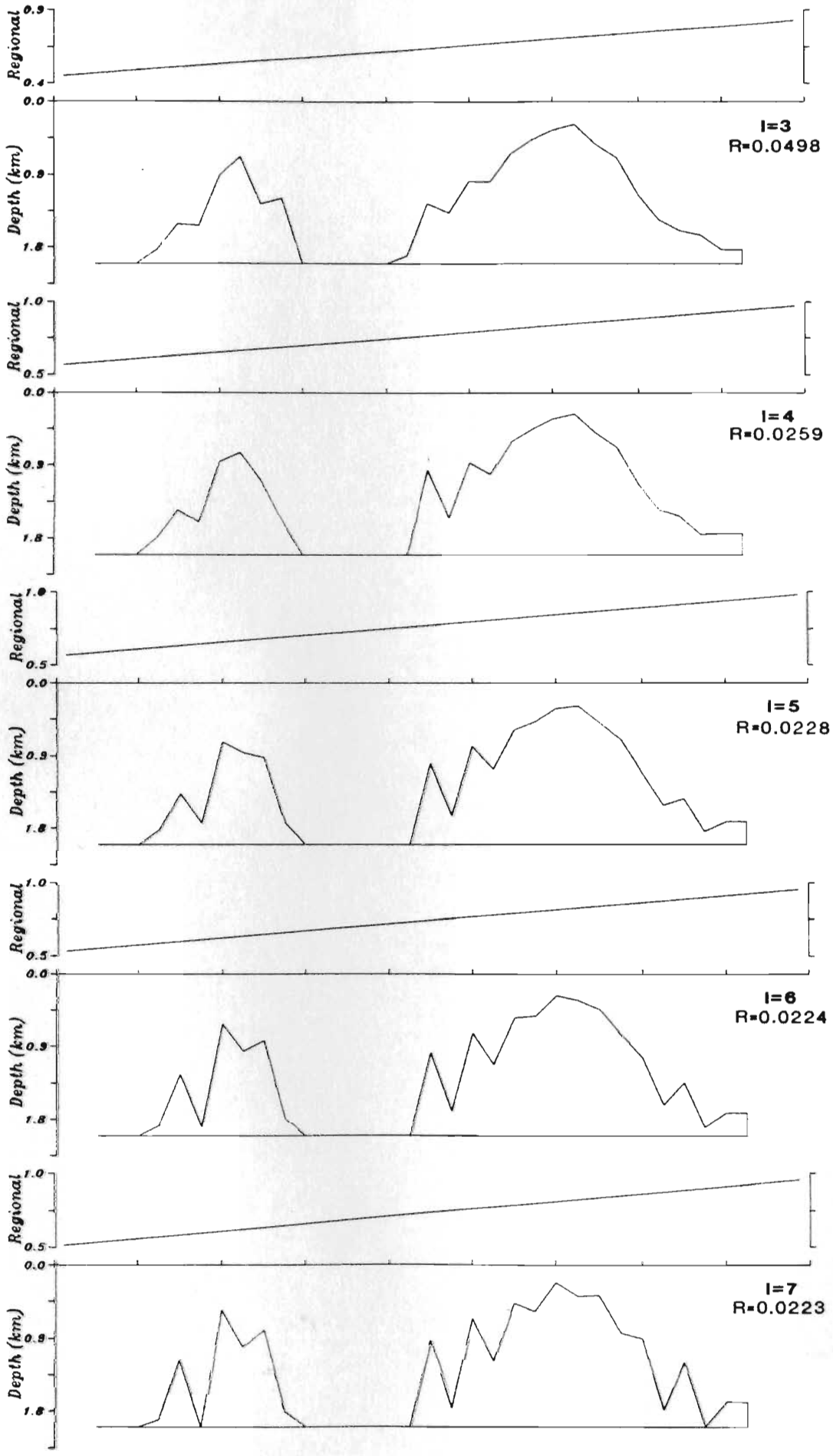

Figure 5.2 (continued).

model complexity. The body coordinate oscillation observed beyond $I = 3$ is partly a consequence of the sensitivity of the model to the programming approach. The problem is particularly well developed on the model having the 2.0 km basal depth. Through application of a double precision version of the improved inversion scheme, as contained in the program listed in Appendix A, the oscillation was reduced such that convergence to a body similar to those from 1.5 or 2.5 km depth resulted.

To observe the effects of density variations on the inverted structure, inversions were performed from a sloping basal limit, defined by the time picks of the R1 reflector on seismic line E-20 converted to equivalent depths. Inversion results using bodies having density contrasts of -0.20, -0.25, -0.30 and -0.35 gm/cm^3 are displayed in Figure 5.3. Inversion with a density contrast of -0.30 gm/cm^3 results in a modelled structure of least complexity. Generally, the inverted structures imply a lesser cross-sectional area of salt than would be inferred from the seismic section. However, gypsum or clastic impurities as are present in salt sequences from boreholes within the basin onshore, would increase the average density of the salt structure, decrease the magnitude of its density contrast, and thereby increase the volume of a causative body. The degree to which the structure departs from two-dimensionality and the possibility that evaporites do not extend to the pre-Carboniferous basement are likely contributing factors to this apparent volume discrepancy. The presence or absence of sediments beneath evaporite structures cannot be ascertained since structure is generally not discernible beneath the strong R2 reflectors on section E-20.

Since the anomalous effects of subsurface bodies contribute additively to the total anomaly, the anomaly portion due to evaporites was removed from the profile. The resultant profile has a nearly linear gradient similar to that expected from a basin dipping monoclinally to the southeast. The density of the clastic sedimentary infill was

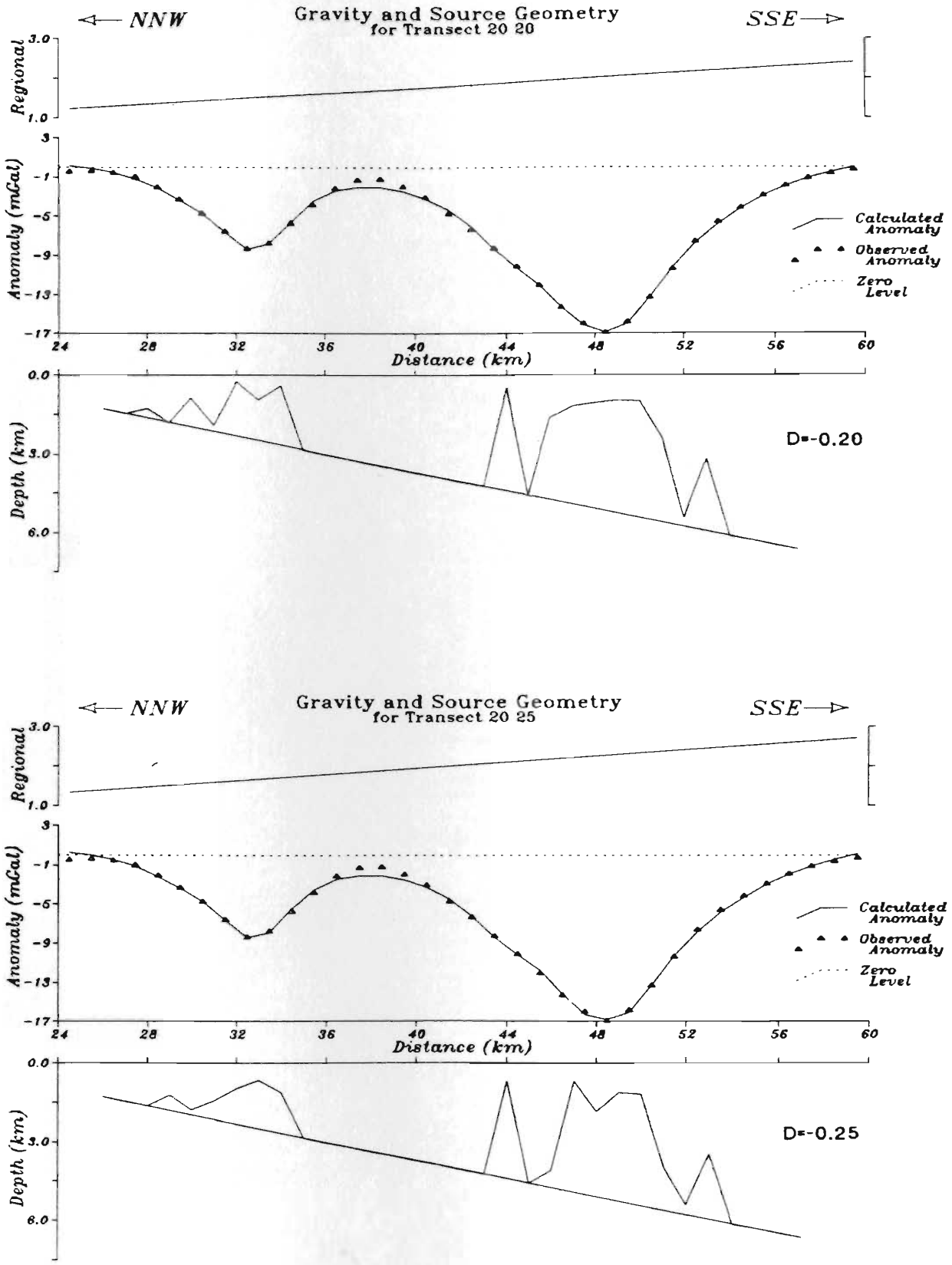

Figure 5.3. Inversion results from a basal level, z_0, having a slope equivalent to that deduced from R2 picks on seismic line E-20 for the portion of the gravity anomaly over transect $A - A'$ arising from interpreted salt structure. Displayed are evolved bodies having density contrasts, D, of -0.20, -0.25, -0.30 and -0.35, respectively, relative to clastic sediments.

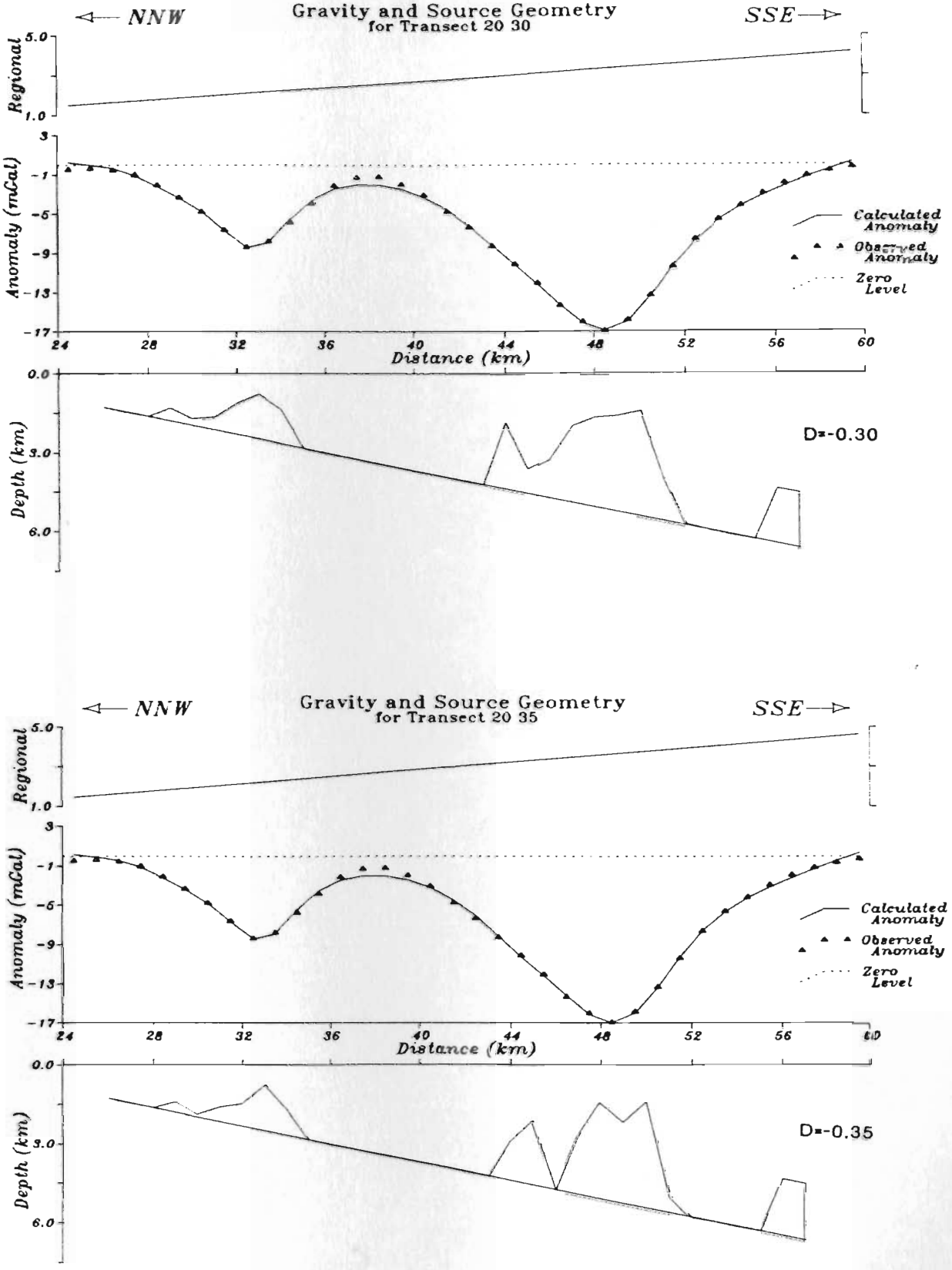

Figure 5.3 (continued).

then assumed homogeneous and the contribution to the gravity anomaly of the underlying basement block of positive density contrast was assumed linear. This enabled the density contrast of the sedimentary section to be estimated as that homogeneous body having its basal boundary defined seismically and giving the best fit to the residual gravity anomaly.

Using the resultant density contrast, -0.13 gm/cm^3, for Codroy Group sediments offshore, a forward 2-D model was configured for Line E-20. A sufficient thickness of high density basement was added to account for the total anomaly observed. It is realized that modelling of this positive density block introduces ambiguity to the interpretation: a small change in the density contrast of either the sediment block or the high density basement block may be countered by altering the thickness and shape of basement material, contributing the positive offset to the field observed. Figure 5.4 shows the final geological configuration modelled from gravity (transect $A - A'$ on Map 5) underlying seismic line E-20, and extended onshore to the Long Range Fault subbasin margin. Digitized values of the contoured gravity field (see Figure C-4) were used in the modelling since a profile of anomaly values at stations within 5 km of Line E-20 (see Figure 5.5) were found to be too variable to provide necessary constraints to an accurate model of the sedimentary infill, and, in particular, the evaporite structures.

Of particular note is the presence of the positive density contrast block (+0.075 gm/cm^3) underlying the subbasin offshore, but not continuing onshore beneath Anguille strata ($\Delta\rho$ = -0.05 gm/cm^3 on Figure 5.4). This model concurs with the interpretation that the offshore subbasin is underlain by a basement block which was transported to the northeast by right lateral strike-slip and denuded during late Anguille time, before becoming the locus for Codroy Group deposition, such that the pre-Carboniferous "basement" beneath the onshore and offshore parts of the subbasin are of contrasting compo-

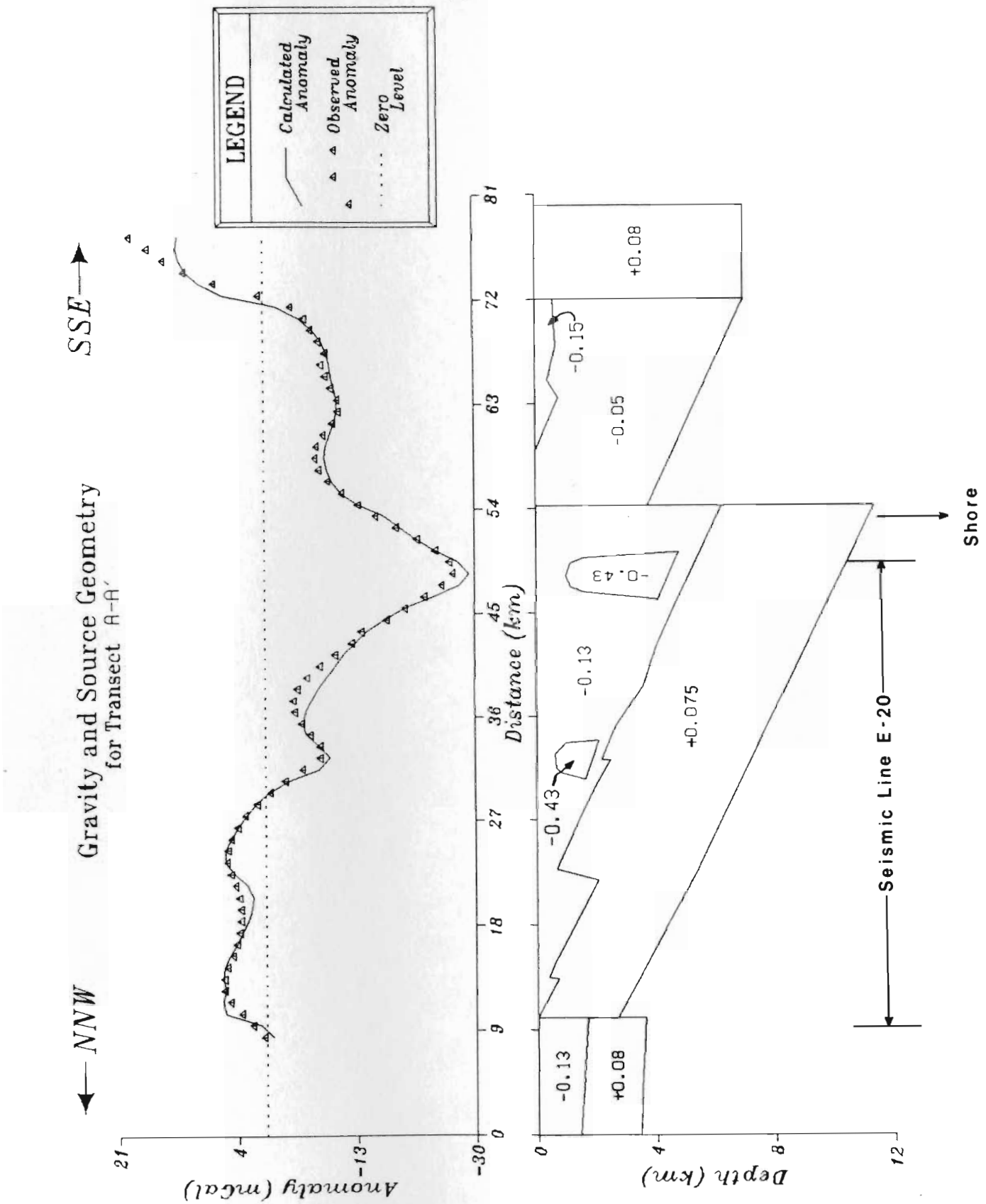

Figure 5.4. Cross-section of 2-D model for Transect $A - A'$, the digitized values of hand-contoured gravity data along seismic Line E-20. Two salt structures ($\Delta\rho = -0.43\ gm/cm^3$) are included within the Codroy sedimentary half-graben infill ($\Delta\rho = -0.13\ gm/cm^3$) offshore. A half-graben comprised of Anguille sediments ($\Delta\rho = -0.05\ gm/cm^3$) and Codroy Group in the upper section attains a 7 km depth at the Long Range Fault margin (X=72 km). Gently dipping carbonates overlain by a Carboniferous sediment wedge are modelled to the NNW of a suspected fault (at X=10 km).

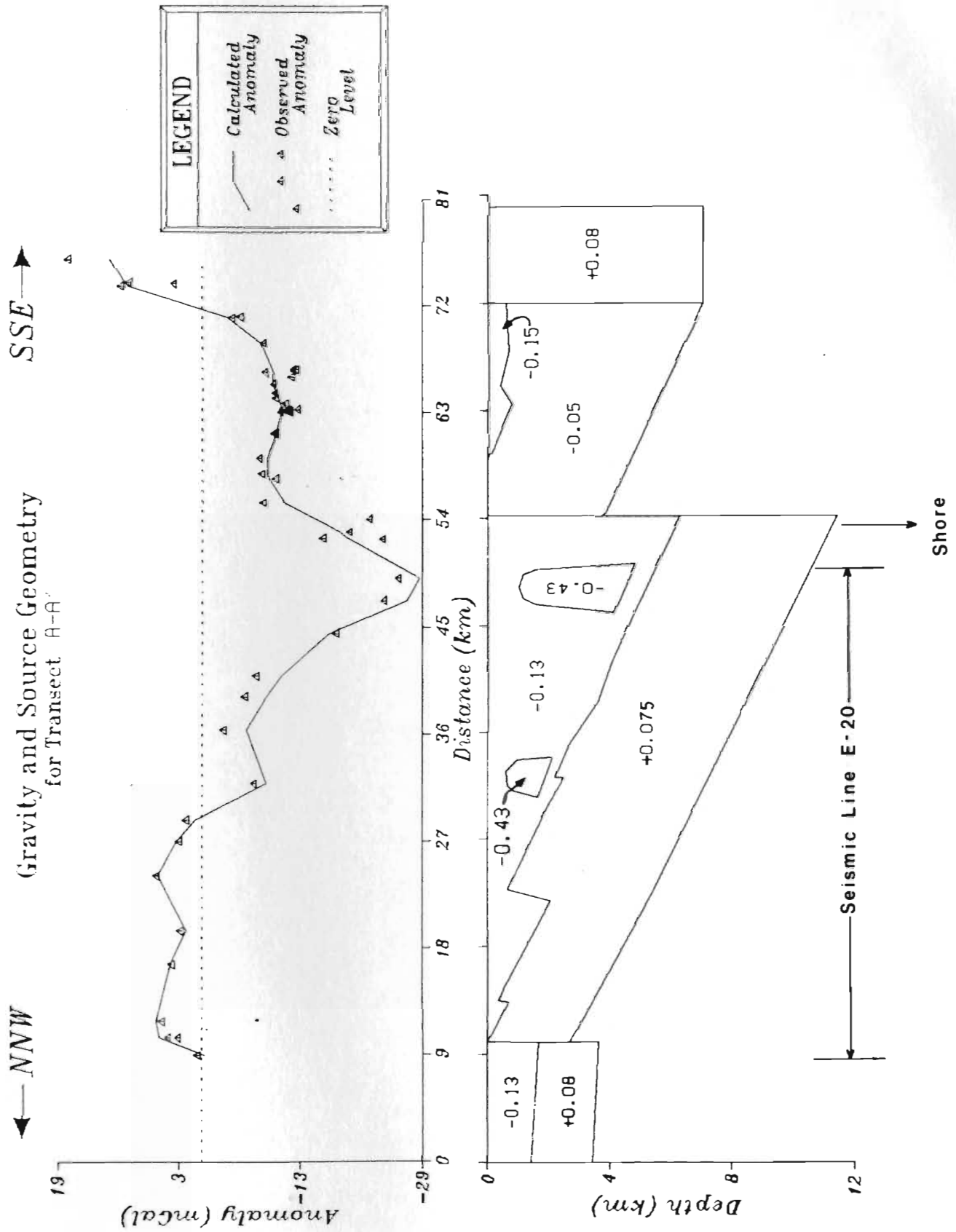

Figure 5.5. Transect $A - A'$ of gravity values from all stations within 5 km of seismic Line E-20. The 2-D gravity model is the same as in Figure 5.4.

sitions. Such is consistent with the low levels and smoothness of the magnetic field over the subbasin portion containing Anguille Group sediments, which indicate a very deeply buried magnetic source, if magnetic basement occurs beneath the Anguille section at all. Addition of a positive density contrast basement block immediately beneath the Anguille Mountains on transect $A - A'$ would result in an anomalously thick sequence of these high density sediments on the model of Figures 5.4 and 5.5.

Anguille sediments are depicted in Figure 5.4 as filling a deep half-graben onshore, bordered to the southeast by positive density contrast Long Range Complex rocks. Local depressions in the Bouguer anomaly field are accommodated by shallow wedges of Codroy Group sediments as mapped on the surface. Structure within the oldest remnants of the subbasin, now represented by Anguille sediments, is likely much more complicated than depicted. Resolution of complicated structure is diminished, though, due to the low magnitude of Anguille Group density contrast and the common occurrence of Codroy sediments forming the near surface lithology.

The salt anticlines from earlier inverse modelling are included in the offshore sediments of Transect $A - A'$. Salt was modelled using a $\Delta\rho = -0.43\ gm/cm^3$. The cross-section of salt illustrated in Figure 5.4 is representative of the lower limit of actual accumulation. Modelling using a greater density for salt and finite strike dimensions, as shown in Map 5, would evolve models of increased cross-sectional area.

Interpretation was extended with uncertainty beyond the northwest end of Line E-20. Here, relatively flat-lying sediments overlying a block of carbonates are modelled to the northwest of a suspected fault. The thicknesses shown are uncertain as a result of a lack of gravity data control. The fault trends north-northeastward, coincident with the northwest coastline of the Port au Port Peninsula. Reflection seismic lines located in the offshore northwest of the Port au Port Peninsula indicate near horizontal stratigraphy.

A two dimensional cross-section resulting from modelling the gravity data for Transect $B-B'$ (along seismic Line E-24) is shown in Figure 5.6. Transect $B-B'$ contains many of the features of Transect $A-A'$ discussed above. Again, only the offshore half-graben, filled with Codroy sediments (modelled with $\Delta\rho$=–0.15gm/cm^3) containing two evaporite structures is underlain by a high density Precambrian basement layer in the model. A northwest dipping block of positive density contrast was included for the region beneath the Port au Port Peninsula to represent its early Paleozoic carbonate dominated stratigraphy. The increasing depths to basement northward interpreted from magnetic data (Spector, 1970) and the north-northeastward dips of carbonate strata measured onshore provide evidence for the dipping carbonate wedge model.

The scatter of gravity values near 43 km on Figure 5.6 results from the oblique orientation of the profile with respect to both the evaporite structure and the basement blocks. The cross-section was continued onshore to the southeast where it includes a smaller half-graben block of Codroy sediments. The southeastward dip modelled for the subbasin onshore is much less than the dips interpreted offshore. A block of higher $\Delta\rho$ Anguille sediments would be sandwiched (to the southeast) between the Codroy block and rocks of the Long Range Complex. Modelling of this portion of the subbasin is discussed further below in conjunction with Transect $D-D'$.

A gravity profile transecting the inner portion of St. George's Bay and through the Flat Bay anticline was modelled and appears as Transect $C-C'$ in Figure 5.7. The orientation chosen is nearly true southeast, oblique to Transects $A-A'$ and $B-B'$, more perpendicular to lithologic trends and the local subbasin axis. The offshore Codroy sediments and the underlying basement block were assigned more negative $\Delta\rho$ values during modelling of Transect $C-C'$ than those on Figures 5.4 and 5.6. Sedimentary infill appears to be of lower density in the inner parts of the subbasin and may contain Bara-

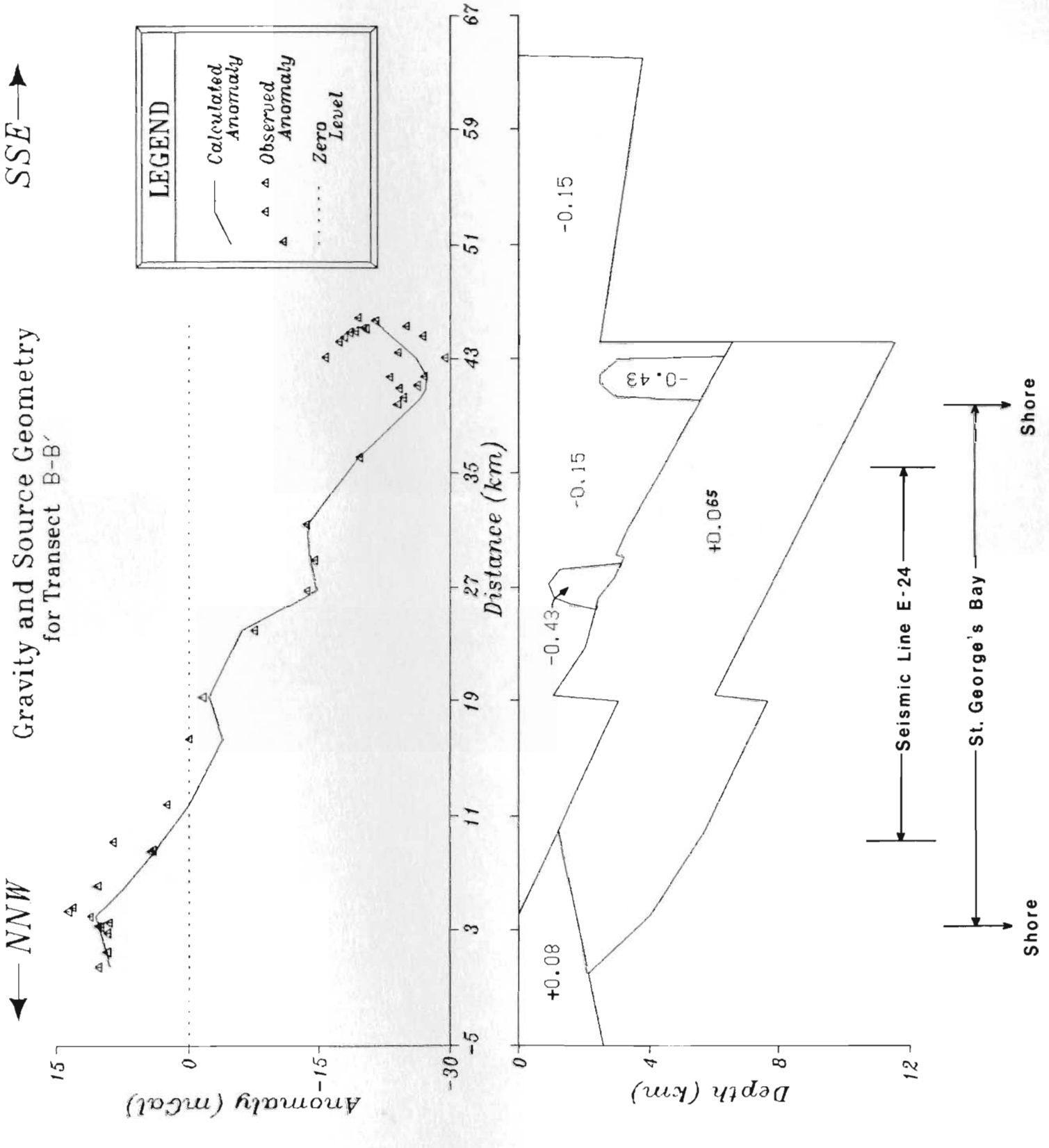

Figure 5.6. Transect $B - B'$ of gravity values within 5 km of seismic Line E-24 and modelled 2-D cross-section. A fault at 44 km separates a faulted half-graben containing sediments (and salt) offshore from a smaller Codroy wedge onshore. A northwest-dipping wedge of carbonates ($\Delta\rho = +0.08 gm/cm^3$) is modelled beneath the Port au Port Peninsula.

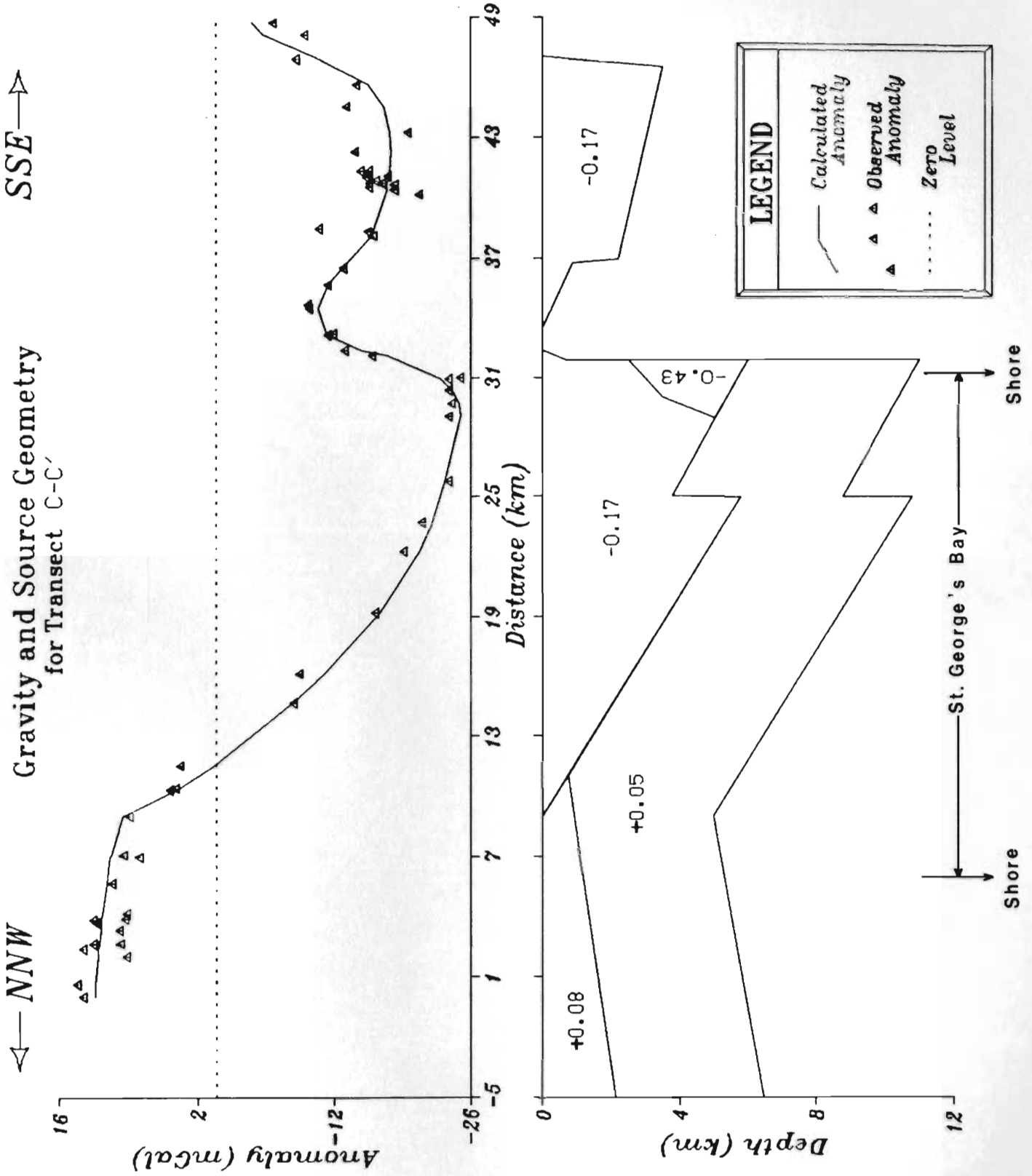

Figure 5.7. Cross-section (2-D) modelled for gravity values from all stations within 5 km of Transect $C - C'$ (see Map 5 for location). A raised, fault-bounded block of Precambrian basement, forming the core of the Flat Bay Anticline, separates a faulted half-graben of Codroy sediments ($\Delta\rho = -0.17 gm/cm^3$) offshore from a smaller block onshore. A wedge of carbonates ($\Delta\rho = +0.08 gm/cm^3$) beneath the Port au Port Peninsula dips to the northwest. A small salt body is situated within the thickest sedimentary section.

chois units in the upper section. As in Figure 5.6, a northwestward dipping block of carbonate rocks is modelled beneath the Port au Port Peninsula. A wedge of salt (at 31 km) is situated against the fault controlled block of Grenvillian basement which outcrops near Flat Bay. To the southeast, a fault-bounded half-graben filled with sediments is developed. Surface outcrop here indicates that sedimentary infill consists of lower Codroy strata topped by clastics from the Barachois Group. The included gravity values for stations within 5 km of the profile show extensive variability for this section as a result of the oblique transect intersection relative to basement blocks.

Transect $D-D'$ of Figure 5.8 shows an interpretation of a gravity profile over the short wavelength low anomaly, situated at the southeast corner of Codroy exposure onshore. "Observed" anomalies are then interpolated at a spacing of 1.0 km from the hand-contoured map of Bouguer anomalies for a principal profile over the elongate anomalous feature. A salt pillow within Codroy sediments of -0.43 gm/cm^3 density contrast and having a strike length of 4.0 km was interpreted as giving rise to the observed negative anomaly. All other blocks on the model have a strike length of 100.0 km to simulate infinite dimensions perpendicular to profile. The model is the result of a 2.5-D modelling where the salt is situated entirely within the Codroy sediment block. Thus the salt was modelled as an extra block of a density contrast of -0.30 gm/cm^3, which together with the -0.13 gm/cm^3 density contrast of Codroy sediments already occupying that region, produces a net contrast $\Delta\rho$ of -0.43 gm/cm^3. A block of higher density Anguille sediments is wedged between the Codroy and Long Range Complex rocks having positive density contrast. Positioning of the major units is constrained by contacts extracted from the geological map of Knight (1983), Map 1. The model of Figure 5.8 is included here to illustrate one possibility. As in all the models presented here, it is merely one of the many possible under the geologic and realistic constraints, and its vali-

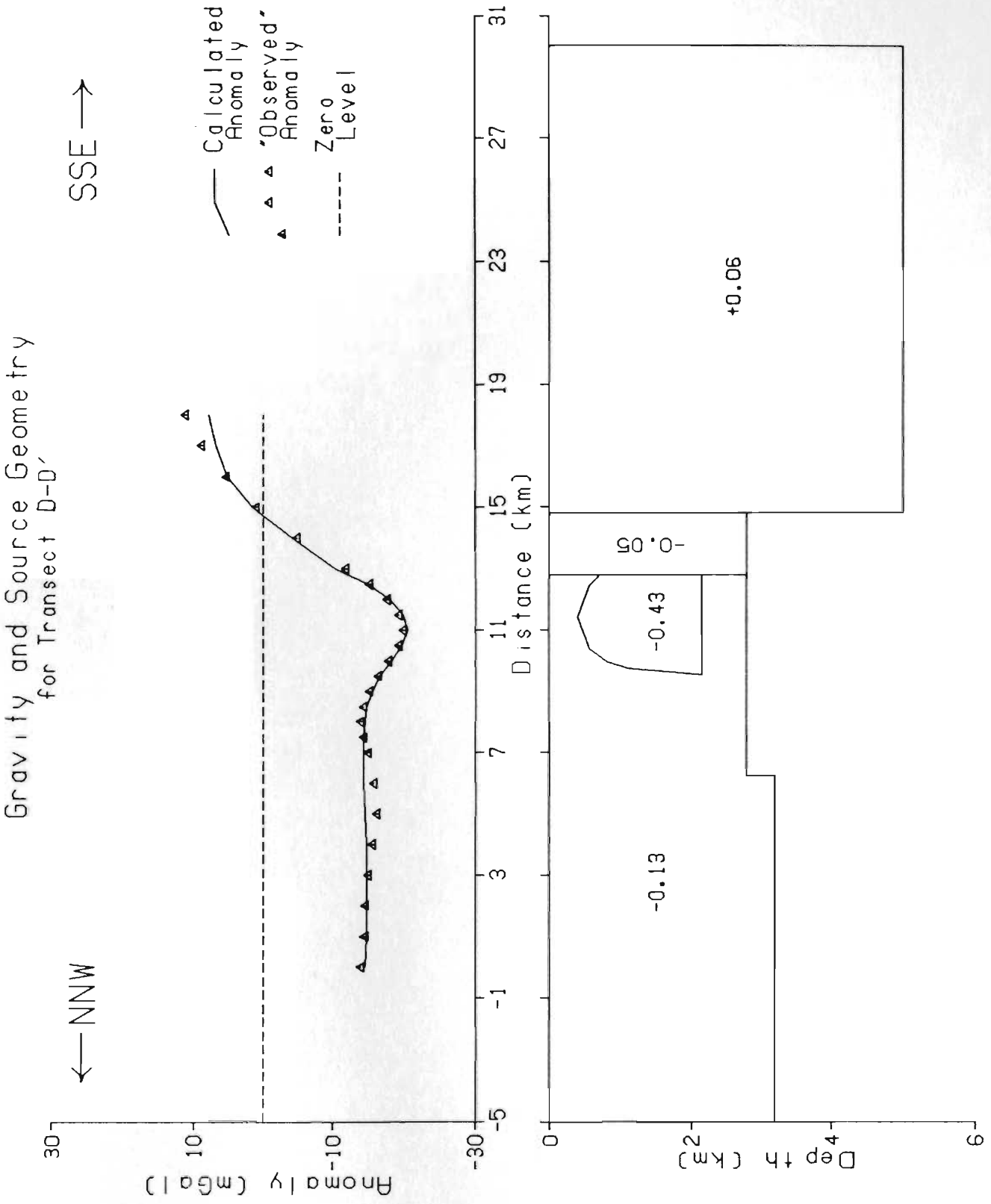

Figure 5.8. Modelled principal profile, $D - D'$, over an interpreted salt body ($\Delta\rho = -0.43\ gm/cm^3$) within Codroy sediments ($\Delta\rho = -0.13\ gm/cm^3$) located near the southwest corner of onshore Codroy exposure. A wedge of Anguille sediments of density contrast -0.05 gm/cm^3 is sandwiched between Codroy sediments to the NNW and denser Long Range Complex rocks to the SSW. Here, the salt structure was modelled as a symmetrically disposed 2.5-D body of 4.0 km strike length.

dity is subject to the following limitations:

- depth to basement is uncertain and highly density dependent. Peavy (1985)'s modelling showed found depths to be highly variable within the area adjacent to the Long Range Complex.
- the density of Codroy Group clastic sediments may be lower than modelled, thereby increasing the magnitude of negative $\Delta\rho$.
- the underlying pre-Carboniferous basement is not assigned a positive $\Delta\rho$ onshore, as it would increase the depth to basement of this portion of the subbasin.
- hand-drawn contours were used to define the gravity field values used in modelling.
- the density of Long Range rocks is uncertain. The large variabilities observed in the gravity field along its length indicate a laterally heterogeneous density distribution within the Complex.
- Stations located southeast of the Long Range Fault have not been corrected for the effects of variable terrain. The field within the Complex is not of prime concern for this study.
- All bodies, other than salt, are modelled as being nearly two dimensional in shape and oriented perpendicular to the profile. In reality, these blocks have finite strike lengths. The profile is oriented to give the best approximation to two dimensionality of all units transected.
- Barachois sediments, present in the upper section at the northwest end of Transect $D-D'$, increase the average density of the section and are likely responsible for the slight "rise" in gravity observed.
- Geologic boundaries are those mapped at the surface by Knight (1983). For model simplicity vertical contacts are assumed.

The 2.8 to 3.2 km thickness of sediments depicted is probably close to the lower limit of actual thicknesses in this area. The presence of a positive density contrast basement block would increase the depth while a larger negative density contrast for Codroy sediments would decrease depth estimates. The thickness of salt required to give rise to the anomaly near the subbasin margin (to the southeast on Figure 5.8) places a lower limit on basement depths here. The low amplitude feature to the NW of the large negative is a relict of local contouring which, from its short wavelength nature, indicates the presence of a near-surface mass deficiency. The model presented does illustrate the excellent agreement of data with the geologic interpretation; contacts are mapped at the positions that gravity data would suggest they occur. Regardless of the configuration of sediment blocks, a massive salt body is inferred to give rise to the short wavelength

negative gravity anomaly of cross-section D–D′.

In comparison with gravity modelling, attempts to model a two dimensional structure from magnetic data profiles were unsuccessful for the following reasons:

1) the large depth to basement throughout most of the subbasin introduces much ambiguity into the modelling
2) single transects contain data from different sources
3) assumptions of two-dimensionality of structure and uniformity in magnetic susceptibility are overly simplistic and are not valid.

The magnetic data for the Bay St. George subbasin is considered better interpreted from a qualitative viewpoint to obtain relative rather than absolute depths to sources.

6. Conclusions

The internal structure of the Bay St. George Subbasin is strongly expressed on maps of compiled surface potential field data collected throughout the subbasin as well as on reflection seismic profiles for offshore areas. Steep gravity and magnetic gradients characterize the Long Range Fault on the subbasin's southeast margin. Both potential field datasets, in particular the magnetic dataset, display an eastward jog in the marginal trend near 5325 to 5330 N UTM (Maps 2,3). It is interesting to note that a prominent east-west fault coincides in location with this offset in data trends along the Long Range Fault front. Possible explanations for this phenomenon are compositional variation within the anorthositic to metasedimentary/metavolcanic suite of rocks locally comprising Long Range Complex (van Berkel *et al*, 1986; Chorlton, 1983) leading to lateral density variations or eastward sediment underthrusting along the Long Range Fault. From steep dips measured at the Fault front, the former seems the more plausible. Significant density variations are reported within anorthositic suites elsewhere (Kearey and Thomas, 1979).

Strong gravity and magnetic gradients similarly mark the northwestern and northern boundaries of the early Anguille graben. A magnetic interpretation would place magnetic basement at great depth beneath the Anguille Group, suggesting that earliest Anguille sediments were deposited upon a layer of uncertain rock type, but having low magnetic content.

Gradients along the northwest and southeast sides of the Flat Bay Anticline indicate that an uplifted fault-bounded basement block, similar in magnetic character to Indian Head Complex rocks outcropping in its core, underlies sediments here.

Gentle gravity gradients offshore indicate a basin dipping to the southeast. Basement reflection picks from seismic profiles have confirmed a half-graben structure filled

with predominantly Codroy sediments for the subbasin offshore. The subbasin attains depths to basement of greater than 5 km just northeast of the southeast coastline. The resultant features are superimposed on a broad positive gravity field and associated with high magnetic values which identify the offshore portion of the subbasin as underlain by Precambrian rocks of Indian Head affinity. Magnetite-rich lenses and stringers within the basement as mapped within Indian Head outcrop east of Stephenville and in the Flat Bay Anticline core give rise to the variable magnetic fields recorded. A series of east-west strike-slip faults spaced on the order of 10 km are interpreted as transecting the subbasin and individually displacing features locally on the order of 5 km (Map 5). The resultant distribution of sediments within the subbasin reflect a complex configuration of rhomb-shaped (Aydin and Nur, 1982) basement blocks.

The northwest trend of St. David's Syncline is anomalous and it has been difficult to explain its orientation as it is not a member of the conjugate pair for the northeast directed strike slip regime in the early basin opening. It is interesting to note that a mental "unfaulting" of the subbasin to its configuration previous to these east-west displacements, would re-orient the interpreted north-south fault at the western basin margin to a similar northwest trend, provided that the latter fault pre-dates those of east-west orientation.

Positioning of faults is a bit uncertain as each dataset would suggest their placement at slightly differing positions. Identified "faults" are more likely fault zones of finite width, and may consist of several subparallel faults and fault splays. Faults as indicated herein are generally positioned at the best location to satisfy all datasets. More detailed surveys would be necessary to pinpoint individual faults. If this late faulting were contemporaneous with deposition, then the uppermost sediments in the section should show draping and roll-over features, the locations of which could provide drilling

targets for hydrocarbon exploration. However, apparent discontinuity of intra-sediment reflectors on seismic sections indicates that these faults have experienced a significant portion of their displacement since Carboniferous deposition. Fractured sedimentary units in the subbasin may thus have low potential for reservoir preservation.

Warped sediments comprising the upsection half-graben fill offshore are interpreted here as being Vis\an in age on the basis of the presence of Codroy evaporite sequences sequences onshore. However, there is no evidence on seismic sections that the uppermost section does not contain Barachois sediments. Acquisition of seismic reflection profiles over the belt of Barachois exposure of the St. George's lowlands, adjacent to the Long Range Complex onshore where correlation may be made with available drill core data, should be attempted to aid in defining the nature of uppermost offshore sediments.

Follow-up surveys should be carried out to investigate the anticline defined by the largest negative gravity anomaly, located immediately offshore from the Anguille mountains, as it contains the most extensive and most prospective salt occurrence anywhere in the subbasin and seismic data indicate that salt may outcrop in its core. In particular, the area near St. David's Syncline requires detailed survey in the difficult to access region of the near-shore. At this locality, the presence of an east-west strike-slip fault having minimal vertical displacement is best indicated by seismic and gravity data that indicate lateral offset of an evaporite cored anticline.

The availability of seismic reflection lines for the offshore region was an invaluable addition to this project in delineating the basin shape and locating some of the internal sediment structure, and thus providing a constraining model for the interpretation of gravity and magnetic data. However, as a result of the generally poor seismic quality, several of the features illustrated as seismically defined in Appendix C were not identified from the sections previous to their integration with gravity and magnetic data.

Gravity profiles along sections lent confidence in locating several of the major evaporite structures. Hand-contoured potential field maps identified the locations of faults having solely strike-slip displacements and that were therefore only subtly expressed on seismic sections. While magnetic data were of less value than gravity and seismic data in interpreting offshore areas, particularly in the deeper portions of the subbasin, anomalous magnetic features played an integral role in determining the basement topography and interpreting the tectonic history of onshore regions.

In summary, the author found the various datasets to be handsome complements to each other. While realizing the limitations of potential field data, one must pose explanations for their anomalous features rather than discredit their validity. Onshore areas are well covered by gravity stations. However, detailed follow-up surveys of areas where evaporite sequences of interest have been identified might well be undertaken. A few well-positioned quality reflection profiles in onshore regions would be a welcome complement to the present potential field dataset in defining the subsurface extent of sediments as well as the configurations of major faults. Of particular interest is the orientation of pre-Carboniferous basement beneath these sediments leading to a better understanding of the regional tectonic history. Studies to date suggest that the basement beneath the onshore portion of the subbasin is highly faulted and irregular near the Long Range margin (Peavy, 1985; Knight, 1983).

In the offshore area, seismic and gravity data combine to define structural features in the outer St George's Bay region from the western tip of Port au Port to the southeast coastline. Gravity data has delimited two large parallel anticlinal structures in Codroy strata. A detailed gravity survey over the features would aid in pinpointing positions of local gravity lows and thus would accurately locate the crests of these structures. Anticlinal features trend to the northeast, obliquely to the data grid of the

present gravity survey such that, where stations are located near the crests, local minima are defined. On rows of gridded gravity data intermediate between these minimum locations, where stations were positioned over anticline flanks, the contours of the gravity field give the overall impression of periodic structure pinch out along strike. In the inner bay area where no seismic data presently exists, the scale of basement blocks is necessarily smaller due to basin narrowing. Here, the regional gravity survey grid is obviously too coarse to accurately define the basement blocks configuration. The broad gravity low indicated may actually be the cumulative result of several low density short-wavelength features. Further gravity survey is recommended for the region north of Flat Bay and east to the mouth of St. George's River, an area which corresponds to a gap in the present gravity dataset. This small area is of particular interest since the strong negative magnetic gradient and large gravity gradients to either side are interpreted as caused by an extension of an east-west directed fault. The southern closure of a relative gravity high associated with Indian Head Complex rocks to the north is particularly ill-defined due to this data gap.

It is recommended that in future, interpretations elsewhere in the Maritimes Basin be made in light of the new evidence for east-west strike-slip faulting, in particular, within the East Magdalen Basin and the Carboniferous subbasins of Cape Breton and offshore from the south coast of Newfoundland. The Chedabucto Fault extending eastward from Cape Breton Island (Webb, 1972) provides an excellent correlative. On the large scale, such faults have altered the apparent orientation of major basin features and contorted the subbasin to its present elongate shape. East-west faults did not control early basin formation, but are interpreted as post-dating depostion of the Codroy Group, since warped late Mississippian sediments are transected and displaced. However, exact timing of this tectonic event remains uncertain in that there is little evidence to support

a dating as early as Carboniferous other than the unconformity which exists at the base of Barachois Group sediments. A pre-Pennsylvanian timing of east-west faulting may be put forth to explain late basin opening and renewed sedimentation of Barachois rocks apparently confined to isolated pockets adjacent to the Long Range Fault.

Although the major structural trends in Newfoundland oriented northeast are the more easily recognizable and control deposition within the Bay St. George Subbasin, the east-west faults which later deform the basin are of equal importance in understanding the present geological configuration observed at the surface. Through the use of integrated datasets as used here, these secondary trends and offsets may be enhanced in other areas of Newfoundland to bring about a better understanding of the complex structural geology.

Acknowledgements

I would like to thank the following for the support and resources that they have provided me during my graduate studies at Memorial University:

Dr. H.G. Miller, my thesis supervisor, for his enthusiastic encouragement and for openly providing the advice, stimulation, and freedom of thought necessary to produce this paper.

Dr. G. Quinlan for his counsel and friendship throughout my studies at Memorial.

Drs. J.P. Hodych, J.A. Wright, J.B. Merriam, M.G. Rochester, E.R. Deutsch, and J. Hall of the Geophysics Group at MUN for their teaching and numerous constructive discussions.

Dr. J. Woodside, Atlantic Geoscience Center, Dartmouth, N.S., for availing the Bedford sea magnetometer data on digital tape.

Dr. I. Knight of the Newfoundland Department of Mines and Energy for valuable discussions on the geology mapped onshore and its structural implications. In addition, Alvin Harris, Norm Mercer and other staff members of the Mines Branch are thanked for allowing access to rock storage facilities, documents and reproduction services.

Dr. Hank Williams, Dept. of Earth Sciences, MUN, for consultation on the character and structure of Early Paleozoic rocks in the norther part of the subbasin.

Mr. T.E. Laidley, J. Everard, W. Marsh, and other members of the Dept. of Earth Sciences Technical Support staff for their assistance in resolving the many logistical obstacles encountered.

The staff of Computing Services, MUN, for affording access to computer utilities and guidance in their usage.

The School of Graduate Studies and the Department of Earth Sciences at Memorial

University for financial support granted in the form of a university fellowship and departmental bursary, respectively.

My fellow graduate students, in particular, S.T. Peavy, C.L. Fang, C. Garrity, J.N. Prasad, R. Quick, S. Webb, Z. Peng and the many undergraduates whose friendship proved invaluable during the course of my studies.

Bibliography

Al-Chalabi, M., 1971. Interpretation of gravity anomalies by non-linear optimisation, Geophys. Prosp., **20**, 1-16.

Aydin, A. and Nur A., 1982. Evolution of pull-apart basins and their scale independence, Tectonics, **1**, 91-105.

Baldwin, B. and Butler, C.O., 1985. Compaction curves, AAPG Bull., **69**, 622-626.

Banerjee, B. and Das Gupta, S.P., 1977. Short Note: Gravitational attraction of a rectangular parallelepiped, Geophysics, **42**, 1053-1055.

Barr, S.M. and Raeside, R.P., 1986. Pre-Carboniferous tectonostratigraphic subdivisions of Cape Breton Island, Nova Scotia, Maritime Sediments and Atlantic Geology, **22**, 252-263.

Belt, E.S., 1968. Post-Acadian rifts and related facies, Eastern Canada, *in* Studies of Appalacian geology: Northern and Maritime, *eds*. E-An Zen, W.S. White, J.B. Hadley and J.S. Thompson, Jr., New York: Wiley Interscience, pp. 95-113.

Belt, E.S., 1969. Newfoundland Carboniferous stratigraphy and its relation to the Maritimes and Ireland, *in* Symposium on stratigraphy and structure bearing on continental drift in the North Atlantic Ocean, Gander meeting, 1967, *ed*. M. Kay, AAPG Memoir **12**, pp. 734-753.

Bott, M.H.P., 1967. The use of rapid computing methods for direct gravity interpretation of sedimentary basins, Geoph. J. R. astr. Soc. **3**, 63-67.

Bott, M.H.P., 1967. Solution of the linear inverse problem in magnetic interpretation with application to oceanic magnetic anomalies, Geoph. J. R. astr. Soc., **13**, 313-323.

Bradley, D.C., 1982. Subsidence in Late Paleozoic basins in the Northern Appalachians, Tectonics., **1**, 107-127.

Chorlton, L.B., 1983. Geology of the Grandy's Lake area (11O/15), Newfoundland, Part I: Geology of the southern Long Range Mountains, Newfoundland Department of Mines and Energy Report **83-7**, 1-116.

Chorlton, L.B. and Dingwell, D.B., 1981. Grandy's Lake, Newfoundland, *in* Current Research. *Edited by* C.F. O'Driscoll and R.V. Gibbons. Mineral Development Division, Newfoundland Department of Mines and Energy Report **81-1**, 57-69.

Corbato, C.E., 1965. A least-squares procedure for gravity interpretation, Geophysics, **30**, 228-233.

Dainty, A.M., Keen, C.E., Keen, M.J., and Blanchard, J.E., 1966. Review of geophysical evidence on crust and upper mantle structure on the Eastern Seaboard of Canada, *in* The earth beneath the continents, *eds*. Steinhart, J.S., and Smith, T.J., Am. Geophys. Un., Monograph **10**, 349-369.

Forsythe, G.E., Malcolm, M.A. and Moler, C.B., 1977. Computer methods for mathematical computations, Prentice-Hall, Inglewood Cliffs, N.J., USA.

Fournier, K.P. and Krupicka, S.F., 1973. Technique for improved convergence in iterative analysis of gravity anomaly profiles, Geophysics, **38**, 500-506.

Geldsetzer, H.H.J., 1978. The Windsor Group in Atlantic Canada - An update, *in* Current Research, Part C, Geol. Surv. Can., Paper **78-1C**, 43-48.

Geological Survey of Canada, Aeromagnetic Map Series: Geophysical Paper
206, Map 206G(Revised) - "Dashwoods Pond", 1968-69
251, Map 251G(Revised) - "Main Gut", 1968-69
268, Map 268G(Revised) - "Stephenville", 1968-69
269, Map 269G(Revised) - "Harry's River", 1968-69
274, Map 274G(Revised) - "Mainland", 1968-69
316, Map 316G(Revised) - "St. Fintan's", 1968-69
317, Map 317G(Revised) - "Little Friars Cove", 1968-69
318, Map 318G(Revised) - "Flat Bay", 1968-69
4489, Map 4489G - "Codroy", 1970
4490, Map 4490G - "Grandy's Lake", 1970
4503, Map 4503G - "Port aux Basques", 1970

Guillen, A. and Menichetti, V., 1984. Gravity and magnetic inversion with minimization of a specific functional, Geophysics, **49**, 1354-1360.

Haworth, R.T., 1974. Gravity and magnetic Natural Resource Maps (1972), offshore Eastern Canada: Philosophy and technique in preparation by computer, International Hydrographic Review, **51**, 131-155.

Haworth, R.T., 1975. Paleozoic continental collision in the Northern Appalacians in light of gravity and magnetic data in the Gulf of St. Lawrence, *in* Geology of Offshore Eastern Canada, *eds.* van der Linden, W.J.M., and Wade, J.A., Geol. Surv. Can., Paper **74-30**(2), 1-10.

Haworth, R.T., 1978. Interpretation of geophysical data in the northern Gulf of St. Lawrence and its relevance to Lower Paleozoic geology, Geol. Soc., **89**, 1091-1110.

Haworth, R.T. and MacIntyre, J.B., 1975. The gravity and magnetic fields of Atlantic Offshore Canada, Geol. Surv. Can., Paper **75-9**. (*also as* Marine Sciences Paper **15**)

Haworth, R.T. and Watts, A.B., 1974. Geological interpretation of Bouguer anomaly and magnetic anomaly maps east of the Magdalen Islands, southern Gulf of St. Lawrence, Geol. Surv. Can., Paper **74-55**. (*also as* Marine Sciences Paper **10**)

Heyl, A.V. and Ronan, J.J., 1954. The iron deposits of Indian Head area, Geol. Soc. Can. Bull., **22**, 42-62.

IMSL Library: FORTRAN subroutines for mathematics and statistics (with user manuals), Edition **9.2**, November 1984, *IMSL Inc.*, Houston, U.S.A.

International Association of Geodesy, 1967. International gravity formula, Geodetic Reference System (GRS67), Special Publication No. **3**, Paris, France.

Kearey, P. and Thomas, M.D., 1979. Interpretation of the gravity field of the lac Fournier & Romaine River anorthosite massifs, eastern Grenville Province: significance to the origin of anorthosite, J. Geol. Soc., **136**, 725-736.

Knight, I., 1979. Geology map of the Carboniferous Bay St. George Subbasin, Western Newfoundland, Map **82-1**, Mineral Development Div., Newfoundland and Labrador Dept. of Mines and Energy.

Knight, I., 1983. Geology of the Carboniferous Bay St. George Subbasin, Western Newfoundland, Memoir **1**, Mineral Development Div., Newfoundland and Labrador Dept. of Mines and Energy.

Last, B.J. and Kubik, K., 1983. Compact gravity inversion, Geophysics, **48**, 713-721.

Leaton, B.R. and Barraclough, D.R., 1971. Grid Values for the IGRF 1965.0, International Association of Geomagnetism and Aeronomy, Bulletin **29**.

Levenberg, K., 1944. A method for the solution of certain nonlinear problems in least-squares, Quart. Appl. Math., **2**, 164-168.

Lines, L.R. and Treitel, S., 1984. Tutorial: A review of least-squares inversion and its applications to geophysical problems, Geophys. Prosp., **32**, 159-186.

Marquardt, D.W., 1963. An algorithm for least-squares estimation of nonlinear parameters, SIAM J. Appl. Math., **11**, 431-441.

Miller, H.G., 1970. A gravity survey of Eastern Notre Dame Bay, Newfoundland, unpublished MSc. Thesis, Memorial University of Newfoundland.

Miller, H.G. and Weir, H.C., 1982. The northwest Gander Zone - a geophysical interpretation, Can. J. Earth Sci., **19**, 1371-1381.

Miller, H.G. and Wright, J.A., 1984. Gravity and magnetic interpretation of the Deer Lake Basin, Newfoundland, Can. J. Earth Sci., **21**, 10-18.

Mittal, P.K., 1984. Short Note: Algorithm for error adjustment of potential field data along a survey network, Geophysics, **49**, 467-469.

Mobil Oil Canada, Ltd. Project reports: projects **8624-M3-7E**(1971) and **8624-M3-17E**(1973), Port au Port area. (*courtesy* COGLA, Ottawa, Ontario)

Morelli, C., Gantar, C., Honkasalo, T., McConnell, R.K., Szabo, B., Tanner, J.G., Uotila, U. and Whelan, C.T., 1971. The International Standardization Gravity Net 1971 (IGSN71), International Association of Geodesy, Paris, France.

Murthy, G.S. and Rao, K.V., 1976. Paleomagnetism of Steel Mountain and Indian Head anorthosites from Western Newfoundland, Can. J. Earth Sci., **13**, 75-83.

Nagy, D., 1966. The gravitational attraction of a right rectangular prism, Geophysics, **31**, 362-371.

Nettleton, L.L. Gravity and magnetics in oil prospecting, McGraw-Hill, Inc., New York: 1976.

Peavy, S.T., 1985. A gravity and magnetic interpretation of the Bay St. George Carboniferous Subbasin in Western Newfoundland, unpublished MSc. Thesis, Memorial University of Newfoundland.

Pedersen, L.B., 1979. Constrained inversion of potential field data, Geoph. Prosp., **27**, 726-748.

Rasmussen, R. and Pedersen, L.B., 1979. End corrections in potential field modelling, Geoph. Prosp., **27**, 749-760.

Riley, G.C., 1962. Stephenville map-area, Newfoundland, Geological Survey of Canada, Memoir **232**, 72p.

Safon, C., Vasseur, G. and Cuer, M., 1977. Some applications of linear programming to the inverse gravity problem, Geophysics, **42**, 1215-1229.

Schillereff, S. and Williams, H., 1979. Geology of Stephenville Map Area, Newfoundland *in* Current Research, Part A, Geol. Surv. Can. Paper **79-1A**, 327-332.

Scott, H.S. and Evans, A.G., 1952. Geological interpretation of aeromagnetic surveys in two areas on the west coast of Newfoundland, Geology Division, Aeromagnetic Surveys Corporation Limited, Toronto. (*in* Nfld. studies)

Sheridan R.E. and Drake, C.L., 1968. Seaward extension of the Canadian Appalacians, Can. J. Earth Sci., **5**, 337-373.

Spector, A., 1968. Spectral analysis of aeromagnetic data, unpublished Phd. Thesis, University of Toronto, Toronto.

Spector, A., 1969. Report on interpretation of aeromagnetic data, St. George's Bay, Newfoundland. British Newfoundland Exploration Limited, Unpub. report, Open File **12B**(157), Newfoundland and Labrador Dept. of Mines and Energy.

Talwani, M., 1960. Rapid computation of gravitational attraction of three-dimensional bodies of arbitrary shape, Geophysics, **25**, 203-225.

Talwani, M., Worzel, J.L. and Landisman, M., 1959. Rapid gravity computations for two-dimensional bodies with application to the Mendocino Submarine Fracture Zone, J. Geophys. Res., **64**, 49-59.

Talwani, M. and Heirtzler, J.R., 1964. Computation of magnetic anomalies caused by two dimensional structures of arbitrary shape, *in* Computers in the mineral industries, Part 1, Stanford University Publications, Geol. Sciences, **9**, 464-480.

Tanner, J.G., 1967. An automated method of gravity interpretation, Geophys. J. R. astr. Soc., **13**, 339-347.

Telford, W.H., Geldhart, L.P., Sheriff, R.E. and Keys, D.A. Applied Geophysics, Cambridge University Press, New York, 1976.

Verrall, P., 1954. Gravity survey of Bay St. George area, S.W. Newfoundland, Geological Survey of Newfoundland, unpub. report, Open File **12B**(63), Newfoundland and Labrador Deptartment of Mines and Energy.

Vigneresse, J.L., 1978. Damped and constrained least squares method with application to gravity interpretation, J. Geophys., **45**, 17-28.

Watts, A.B., 1972. Geophysical investigation east of the Magdalen Islands, Southern Gulf St. Lawrence, Can. J. Earth Sci., **9**, 1504-1528.

Weaver, D.F., 1967. Geological interpretation of the Bouguer anomaly field of Newfoundland, Dom. Observ. Pub., Ottawa, Vol. **XXXV**, 223-251.

Weir, H.C., 1971. A gravity profile across Newfoundland, unpublished MSc. Thesis, Memorial University of Newfoundland.

Whitten, E.T.H., 1973. Orthogonal polynomial contoured trend surface maps for irregularly spaced data, Computer Applications, **1**, 171-192.

Williams, E.P., 1974. Geology and petroleum possibilities in and around the Gulf of St. Lawrence, AAPG Bull., **58**, 1136-1155.

Williams, H., 1964. The Appalachians in Northeastern Newfoundland - A two-sided symmetrical system, Am. J. of Science, **262**, 1137-1158.

Williams, H., 1978. Tectonic-Lithofacies Map of the Appalacian Orogen, Memorial University of Newfoundland, Map No. **1** (1:1,000,000).

Williams, H., 1985. Geology, Stephenville Map Area, Newfoundland, Geological Survey of Canada Map **1579A**, Scale 1:100,000.

Williams, H., Kennedy, M.J., and Neale, E.R.W., 1970. The Hermitage Flexure, the Cabot Fault, and the disappearance of the Central Mobile Belt, Geol. Soc. Am. Bull., **81**, 1563-1568.

Wilson, J.T., 1962. Cabot Fault, an Appalachian equivalent of the San Andreas and Great Glen Faults and some implications for continental displacement, Nature, **195**, 135-138.

Won, I.J. and Bevis, M., 1987. Computing the gravitational and magnetic anomalies due to a polygon: Algorithms and Fortran subroutines, Geophysics, **52**, 232-238.

van Berkel, J.T., Johnston, H.P. and Currie, K.L., 1986. A preliminary report on the geology of the southern Long Range, southwest Newfoundland *in* Current Research, Part B, Geol. Surv. Can. Paper **86-1B**, 157-170.

Appendix A1

Appendix A1.1

Referencing Old Potsdam Data

Gravity data collected during the surveys of Weaver (1969) and Weir (1971) were referenced to the previous Potsdam system. The following equation (Anonymous) enables conversion to the appropriate values that would be obtained using the 1967 International Gravity Formula:

$$g_{1967} = g_{Pot} - 0.95 - 13.6 \times \sin^2(\phi) + 0.05 \times \phi$$

where: g is the Bouguer anomaly in mGal

$1967, Pot$ refer respectively to the reference systems

ϕ is the geodetic latitude (degrees) of gravity measurement.

An approximate correction of -6.1 mGal, representing the offset for an average latitude in the present area of study, was added to all data from older datasets. Offsets vary from this value by a maximum of 0.1 mGal over the range of latitudes represented.

Appendix A1.2

Calculation of Observed Gravity

During the summer of 1983, a Lacoste and Romberg temperature compensated gravity meter, # 444, on loan from Earth Physics Branch (EPB) was used for all onshore stations occupied. A similar land instrument, # 172, was used during the 1984 season. A constant temperature Lacoste and Romberg underwater gravimeter, EPB's # G-25 was deployed for all offshore stations occupied during 1984. All meters were readable to the nearest 0.01 meter units (approx. 0.01 mGal).

Gravity measured as meter readings at stations along a traverse, was first transformed to mGal equivalents by linear extrapolation from calibration charts listing

coefficients at 100 reading unit intervals specific to each instrument. Observed gravity was then calculated as:

$$g_{obs} = g_{base} + k(R_{sta} - R_{base,1}) - D(t_{sta} - t_{base,1})$$

where: g_{obs} is the corrected gravity value observed at each the field station on traverse.

g_{base} is the accepted gravity value at the base station

k is an instrument calibration factor

= 1.00078 for # 444

= 1.00001 for # 172

= 1.0004 for G-25

R is a mGal equivalent gravimeter reading

t is time in UT to the nearest minute

subscripts *base* and *sta* distinguish base station and traverse station occupations

D is the drift correction (per unit time), calculated as:

$$D = \frac{(R_{base,2} - R_{base,1})}{(t_{base,2} - t_{base,1})}$$

and subscripts 1 and 2 denote readings at start and end of traverse.

It should be noted here that no corrections have been applied to g_{obs} to account for the effects of earth tides. Base stations were members of the Canadian Standardization Network, whose gravity values are referenced to the IGSN71 standard. Gravity meter drift is assumed linear over the traverse time interval.

Appendix A1.3

Calculation of Theoretical Gravity

The theoretical value of gravity at any point on the reference ellipsoid is dependent only on geodetic latitude and may be obtained from the 1967 International Formula:

$$g_\phi = g_0[1 + C_1\sin^2(\phi) + C_2\sin^2(2\phi)]$$

where g_ϕ is the theoretical value of g at latitude ϕ whose constants in units of mGal are:

$$g_0 = 978031.85$$

$$C_1 = +5.3024\text{E-}3$$

$$C_2 = -5.85\text{E-}6.$$

Appendix A1.4

Elevation Corrections

To determine elevations for gravity stations occupied on land, barometric pressures from two Wallace and Tiernan altimeters were recorded with wet and dry bulb temperatures obtained from sling psychrometers at each station. A similar altimeter and a sling psychrometer were also monitored at 5 minute time intervals at the gravity base station. Thus, by linear interpolation of base station data, simultaneous altimeter and psychrometer data were available for base and station altimeters at the recorded time of station occupation. A reading from all instruments was recorded for calibration at the beginning and end of traverses. Differences in recorded values between each roving and the base station altimeters at the start of the traverse provided offsets for roving altimeters. Linear drifts for roving altimeters were determined as the differences from start to end of traverse relative to the difference recorded for the base altimeter divided by the total traverse time.

Elevations were evaluated as:

$$E = E_{base} + F_{alt}\,[A_{R,t} - A_{base,t} - O_R - D_R\,(t - t_1)] \qquad \text{(A1.1)}$$

where: E is elevation

F_{alt} is the altimeter correction factor

t (also in subscript) is the time of station reading

t_1 is the time of base reading at beginning of traverse

$A_{R,t}$ is the roving altimeter reading at time t

$A_{base,t}$ is the base altimeter reading at time t

O_R is calculated offset for the roving altimeter

D_R is the drift of the roving altimeter

base subscript refers to the base station.

The altimeter correction factor, F_{alt}, is a function of relative humidity, H, and the dry bulb temperature in Fahrenheit degrees, T_f, approximated by the relation (to first powers of variables):

$$F_{alt} = C_1 + C_2 \times H + C_3 \times T_f + C_4 \times H \times T_f \qquad \text{(A1.2)}$$

with coefficients $C_1 = +0.90062$

$C_2 = -1.18954\text{E-}4$

$C_3 = +1.98156\text{E-}3$

$C_4 = +3.26149\text{E-}6$

Coefficients C_i, $(i = 1,4)$ are those of a best-fit polynomial to values digitized from the manufacturer's (Wallace and Tiernan) correction charts accompanying altimeters. Equation (A1.2) gives values marginally different from those of the corresponding charts only in the immediate vicinity of 100% relative humidity. The relative humidity, H, in this equation is an average of relative humidities determined from the roving and base

station observations since the factor is applied to altimeter data from both sources. The relative humidity is obtained from wet and dry bulb psychrometer temperatures, T_w and T_d, respectively using the August-Upjohn equation:

$$H = 100.0 \times \left[\frac{VP_{T_w} - 0.00066 \times B \times (T_d - T_w) \times (1.0 + 0.00115 \times T_w)}{VP_{T_d}} \right]$$

where: T is temperature in Fahrenheit degrees

VP_T is vapour pressure in millibars (mb)

B is barometric pressure

(standard assumption of 1000 mb)

w, d are subscripts indicating wet and dry bulb temperatures.

Finally, the vapour pressure, VP_T is related to temperature by the Clausius-Claperon equation:

$$VP_{T_k} = VP_0 e^{-L_v / RT_k}$$

where: T_k is the temperature in degrees Kelvin

VP_0 is a constant for H_2O (=4.15E5)

L_v is the latent heat of vapourization of water

R is the universal gas constant.

Elevation at each station was taken as the average of values calculated via equation (A1.1) for each of the two roving altimeters.

Appendix A1.5

Bouguer Reduction for Onshore Stations

Gravity observed at various elevations requires corrections to bring all values to a common sea level reference. Anomalies are obtained as the differences between observed

and theoretical values. A free air correction is required to account for differences in distances from the center of mass of the earth. For low order elevation variations from the sea level reference, the gravitational field and hence the free air correction is approximately linear and may be obtained by:

$$\Delta g_{FA} = g_{SL} \left[\frac{E}{R} \right] \tag{A1.3}$$

where: Δg_{FA} is the free air correction

g_{SL} is the value of gravity at sea level

E, R are the elevation and earth's radius in kilometers.

As a first approximation, Equation (A1.3) neglects a small change in the vertical gradient. The neglected terms of the expression account for 0.07, 0.3 and 1.7 mGal at elevations of 1, 2, and 5 km, respectively (Nettleton, 1976). For the maximum of station elevations recorded within the study area (575 m), the neglected portion of Equation (A1.3) accounts for only about 0.03 mGal.

In addition, a Bouguer correction is required to remove the gravitational effect of rock mass between the elevation of measurement and sea level. The Bouguer correction is approximated by a slab of crustal rock constant in density and infinite in horizontal dimensions (the Bouguer slab) having 2π geometry. Thus,

$$\Delta g_B = 2\pi G \rho_c E$$

where: Δg_B is the Bouguer correction

G is the universal gravitational constant

ρ_c is the crustal density, here taken as 2.67 g/cm^3

E is relative station elevation.

All corrections are combined into a single equation,

$$g_B = g_{obs} - g_\phi + \Delta g_{FA} - \Delta g_B$$

which reduces to

$$g_B = g_{obs} - g_\phi + 0.06 \times E + 0.0078 \times h$$

where: g_B is the Bouguer anomaly

E is elevation in feet

and h is the instrument height above the rock surface in inches.

No corrections were applied to stations for the effects of variable terrain or for earth tides.

Appendix A1.6

Bouguer Reduction for Underwater Stations

Gravity values observed offshore were corrected by first approximating the gravitational effect of the water column as that of a slab of thickness equal to the water depth and infinite in horizontal dimensions. As well, to correct for the Bouguer effect of the absence of rock mass between the station depth and sea level reference, an infinite slab of constant density was added. Values of 1.03 and 2.67 g/cm^3 were taken as the densities of sea water and crustal rock, respectively. A free-air correction was applied to account for variable depth below sea level. These corrections were combined into a single equation:

$$g_B = g_{obs} - g_\phi + (0.068735 - 0.22216) \times D_w \qquad \text{(A1.4)}$$

where: g_B is the Bouguer anomaly

g_{obs} is the observed gravity

g_ϕ is the theoretical gravity

and D_w is the water depth of the station.

Water depths were scaled to the nearest fathom (6 ft) from calibrated analog depth sounder records. A constant correction of 6.0 m was added to all resultant water depths to correct for the vessel's draught. Bouguer anomalies, as obtained from Equation (A1.4), were not corrected for variable submarine terrain or for the effects of tides.

Appendix A2

The principal facts for the complete gravity dataset used to generate Map 2 as well as for gravity modelling is listed in Appendix A2.1. Easting and northing coordinates are UTM $\times 10^3$, that is, in kilometers. The data source code key, located at the end of Appendix A2.1, identifies data sources.

A FORTRAN routine listed in Appendix A2.2 allows user selection of either 2-D or 2.5-D gravity data inversion to bodies of polygonal cross-section. This program is based on the forward formulations of Talwani *et al.* (1959) for the 2-D routine and Rasmussen and Pedersen (1979) for the corresponding 2.5-D case.

Appendix A2.1

Station	Easting (km)	Northing (km)	Elevation (m)	Bouguer Anomaly (mGal)	Source Code
85	339.182	5271.812	0.0	11.3	1
86	333.628	5275.177	0.0	7.3	1
87	328.538	5277.650	0.0	2.7	1
88	335.397	5284.092	0.0	4.9	1
89	341.276	5286.521	0.0	1.1	1
90	329.872	5292.056	6.1	-16.0	1
91	321.174	5305.200	1.5	-4.4	1
92	332.473	5301.817	0.0	-11.4	1
93	341.857	5303.584	29.0	-14.7	1
94	355.973	5298.425	391.7	6.7	1
95	365.121	5313.376	295.7	17.5	1
96	353.313	5312.143	42.7	-9.8	1
97	342.381	5313.180	431.3	-5.7	1
98	333.493	5313.465	410.0	-3.9	1
99	327.503	5314.180	0.0	-9.2	1
100	337.538	5323.938	0.0	-15.1	1
101	349.034	5331.299	0.0	-16.1	1
102	360.694	5325.553	173.7	-11.6	1
103	362.585	5342.189	22.9	-24.4	1
104	368.117	5324.266	259.1	-3.9	1
105	367.655	5336.508	76.2	-17.0	1
106	370.780	5343.109	77.7	-14.7	1
107	372.736	5330.833	112.8	-14.5	1
108	373.235	5319.703	381.0	22.2	1
109	373.231	5353.062	1.5	-20.9	1
110	378.666	5329.593	281.9	0.7	1
111	381.061	5337.326	187.5	-15.9	1
112	384.305	5350.602	138.7	-24.0	1
113	387.729	5336.079	312.4	0.8	1
114	386.034	5362.798	29.0	-9.8	1
115	389.065	5328.270	472.4	12.8	1
116	389.324	5341.607	350.5	-4.8	1
117	398.456	5353.668	359.7	-0.9	1
118	390.895	5346.024	274.3	-9.6	1
119	392.652	5360.445	79.2	-17.6	1
120	394.000	5371.655	0.0	-16.3	1
121	395.327	5344.829	198.1	3.4	1
122	398.198	5339.218	341.4	14.8	1
123	403.093	5364.705	274.3	-12.1	1
124	405.959	5359.098	289.6	4.2	1
125	409.821	5369.041	243.8	-9.2	1
126	404.087	5350.106	449.6	14.8	1
127	408.219	5349.925	458.7	23.6	1

Appendix A2.1

Station	Easting (km)	Northing (km)	Elevation (m)	Bouguer Anomaly (mGal)	Source Code
128	413.338	5367.523	350.5	9.3	1
129	416.281	5369.448	379.5	16.3	1
130	420.288	5366.136	234.7	34.0	1
131	419.784	5380.827	0.0	5.4	1
132	413.933	5378.811	0.0	-12.3	1
133	406.288	5374.657	29.0	-19.6	1
134	409.414	5385.578	152.4	-15.1	1
135	413.865	5392.786	138.7	-8.7	1
136	405.127	5392.020	274.3	-12.9	1
137	399.046	5381.115	36.6	-18.4	1
138	390.163	5380.203	76.2	-16.5	1
139	383.648	5377.354	4.6	-19.6	1
140	389.629	5391.478	364.2	-13.5	1
141	400.354	5402.359	0.0	-18.7	1
142	376.493	5395.123	0.0	-16.5	1
143	376.641	5385.990	0.0	-6.3	1
144	372.080	5379.632	6.1	-1.7	1
145	366.346	5376.785	33.5	4.4	1
146	365.455	5381.060	6.1	3.7	1
147	364.249	5389.477	0.0	-5.8	1
148	359.544	5395.528	0.0	-13.2	1
149	352.713	5390.943	0.0	-7.8	1
150	358.980	5383.638	0.0	5.9	1
151	357.814	5376.147	74.7	11.9	1
152	347.258	5375.720	48.8	13.6	1
153	342.191	5373.871	93.0	9.9	1
154	337.272	5371.976	27.4	8.0	1
155	332.762	5370.480	62.5	4.2	1
156	338.830	5381.115	0.0	-0.7	1
157	344.735	5387.670	0.0	-4.9	1
211	422.892	5405.610	188.4	-8.1	2
212	422.031	5405.307	175.3	-8.3	2
213	421.292	5404.965	195.4	-8.9	2
214	420.672	5404.436	190.8	-8.9	2
215	420.173	5403.795	189.3	-8.8	2
216	419.553	5403.248	163.1	-9.4	2
217	418.815	5403.018	152.7	-11.4	2
218	418.074	5402.621	167.3	-10.8	2
219	417.575	5401.980	195.7	-10.7	2
220	417.076	5401.357	216.4	-10.7	2
221	416.942	5400.618	226.5	-10.5	2
222	416.934	5400.025	218.8	-10.3	2
223	416.554	5399.234	208.5	-10.1	2

Appendix A2.1

Station	Easting (km)	Northing (km)	Elevation (m)	Bouguer Anomaly (mGal)	Source Code
224	416.177	5398.628	193.9	-10.4	2
225	415.921	5397.909	198.4	-10.6	2
226	415.784	5396.929	206.3	-9.9	2
227	415.528	5396.210	191.4	-10.1	2
228	415.391	5395.249	148.7	-9.5	2
229	415.135	5394.567	143.3	-10.1	2
230	414.636	5393.981	147.5	-9.5	2
231	414.255	5393.172	124.7	-9.1	2
232	413.876	5392.418	122.5	-10.1	2
233	413.133	5392.003	147.8	-9.5	2
234	412.523	5391.605	189.0	-9.8	2
235	412.382	5391.033	209.1	-9.6	2
236	412.125	5390.314	203.3	-9.8	2
237	411.622	5389.581	198.1	-10.4	2
238	411.365	5388.862	207.0	-10.5	2
239	411.230	5388.067	177.7	-10.4	2
240	410.853	5387.499	175.9	-10.8	2
241	410.227	5386.786	171.6	-11.7	2
242	410.093	5386.066	158.2	-12.2	2
243	409.469	5385.464	144.2	-13.4	2
244	409.092	5384.970	135.9	-14.4	2
245	408.960	5384.379	103.6	-15.4	2
246	408.946	5383.508	150.3	-15.8	2
247	408.811	5382.788	162.2	-16.5	2
248	408.433	5382.220	159.4	-17.7	2
249	407.933	5381.709	150.6	-18.7	2
250	407.185	5381.073	142.6	-19.5	2
251	406.808	5380.578	153.3	-20.1	2
252	406.673	5379.858	130.8	-20.3	2
253	406.537	5379.082	133.2	-20.0	2
254	406.523	5378.248	117.0	-21.2	2
255	406.509	5377.415	85.6	-20.2	2
256	406.371	5376.509	33.8	-20.3	2
257	406.360	5375.842	48.5	-20.1	2
258	406.347	5375.008	25.3	-20.3	2
259	406.207	5374.010	9.8	-20.2	2
260	405.826	5373.315	25.3	-18.8	2
261	405.324	5372.765	49.7	-18.7	2
262	404.945	5372.160	109.4	-18.7	2
263	404.934	5371.530	101.8	-18.0	2
264	404.676	5370.867	117.7	-18.4	2
265	404.052	5370.359	116.4	-19.0	2
266	403.428	5369.906	110.6	-19.5	2

Appendix A2.1

Station	Easting (km)	Northing (km)	Elevation (m)	Bouguer Anomaly (mGal)	Source Code
267	402.681	5369.474	95.7	-19.8	2
268	401.936	5369.116	61.3	-20.0	2
269	401.314	5368.812	50.3	-20.0	2
270	400.448	5368.586	41.5	-19.9	2
271	399.458	5368.363	39.0	-19.8	2
272	398.959	5368.057	23.8	-19.7	2
273	398.088	5367.572	36.0	-19.8	2
274	397.341	5367.196	25.0	-20.3	2
275	396.718	5366.800	29.6	-19.9	2
276	396.093	5366.367	15.8	-19.1	2
277	395.346	5365.936	30.2	-18.7	2
278	394.720	5365.466	45.4	-18.8	2
279	394.095	5364.995	79.9	-18.5	2
280	393.591	5364.449	95.4	-18.4	2
281	393.208	5363.715	113.7	-18.0	2
282	393.193	5362.918	103.3	-16.8	2
283	393.180	5362.233	109.1	-16.8	2
284	393.166	5361.510	100.9	-17.5	2
285	392.906	5360.830	105.2	-17.3	2
286	392.406	5360.469	81.7	-17.1	2
287	391.659	5360.131	76.8	-16.9	2
288	391.157	5359.696	68.9	-16.7	2
289	390.895	5358.941	70.1	-17.3	2
290	390.881	5358.218	69.2	-17.9	2
291	390.254	5357.823	112.8	-16.6	2
292	389.502	5357.259	141.7	-16.0	2
293	389.243	5356.542	161.8	-15.9	2
294	389.103	5355.822	201.2	-15.6	2
295	388.970	5355.068	210.0	-15.1	2
296	388.460	5354.389	217.9	-16.0	2
297	387.835	5353.923	215.5	-15.9	2
298	387.085	5353.459	215.5	-17.2	2
299	386.577	5352.925	195.1	-18.5	2
300	385.952	5352.426	176.8	-18.5	2
301	385.319	5351.949	139.0	-21.0	2
302	384.695	5351.517	153.6	-22.8	2
303	383.945	5351.132	147.5	-24.2	2
304	383.198	5350.869	139.6	-21.2	2
305	382.331	5350.954	120.1	-18.6	2
306	381.472	5351.027	117.7	-18.1	2
307	380.738	5351.365	97.5	-16.8	2
308	379.874	5351.583	80.5	-15.9	2
309	379.365	5351.016	78.0	-14.6	2

Appendix A2.1

Station	Easting (km)	Northing (km)	Elevation (m)	Bouguer Anomaly (mGal)	Source Code
310	378.864	5350.471	80.2	-14.1	2
311	378.847	5349.659	102.1	-15.0	2
312	378.338	5349.114	113.1	-14.4	2
313	377.711	5348.627	125.9	-13.2	2
314	377.077	5348.107	127.1	-12.5	2
315	376.324	5347.623	142.0	-11.5	2
316	375.822	5347.078	147.5	-11.4	2
317	375.310	5346.433	141.1	-12.1	2
318	374.800	5345.855	124.4	-12.3	2
319	374.171	5345.257	106.1	-12.7	2
320	373.545	5344.826	87.2	-13.3	2
321	372.794	5344.487	79.9	-13.3	2
322	372.052	5344.504	61.6	-13.5	2
323	371.307	5344.398	41.8	-14.3	2
324	370.795	5343.798	40.2	-14.7	2
325	370.167	5343.257	52.1	-15.8	2
326	369.533	5342.860	43.0	-15.7	2
327	368.904	5342.318	66.4	-17.4	2
328	368.388	5341.551	83.2	-18.0	2
329	367.882	5340.840	70.1	-18.7	2
330	367.246	5340.377	88.7	-19.3	2
331	366.744	5339.866	68.0	-20.5	2
332	366.729	5339.221	48.8	-21.6	2
333	366.835	5338.663	63.1	-21.6	2
334	367.448	5338.159	77.7	-19.4	2
335	367.924	5337.536	46.9	-17.1	2
336	368.033	5336.778	52.4	-16.2	2
337	368.015	5336.000	100.3	-14.6	2
338	367.997	5335.222	127.7	-12.7	2
339	367.609	5334.530	150.9	-12.1	2
340	367.220	5333.816	143.3	-10.6	2
341	367.330	5333.091	114.0	-9.6	2
342	367.429	5332.199	101.5	-9.9	2
343	367.289	5331.313	76.5	-10.0	2
344	367.144	5330.516	80.5	-10.2	2
345	367.370	5329.654	78.0	-10.3	2
346	367.235	5328.979	96.6	-11.5	2
347	366.723	5328.434	110.9	-11.2	2
348	366.211	5327.868	144.8	-10.8	2
349	365.708	5327.402	182.6	-8.8	2
350	365.196	5326.858	197.8	-7.8	2
351	364.694	5326.625	186.8	-8.4	2
352	364.068	5326.625	205.7	-8.7	2

Appendix A2.1

Station	Easting (km)	Northing (km)	Elevation (m)	Bouguer Anomaly (mGal)	Source Code
353	363.200	5326.436	180.1	-10.5	2
354	362.447	5326.141	171.3	-12.3	2
355	361.573	5325.958	161.8	-12.8	2
356	360.694	5325.590	172.2	-11.3	2
357	359.939	5325.164	180.4	-11.5	2
358	359.184	5324.812	173.4	-11.7	2
359	358.554	5324.438	176.8	-11.9	2
360	357.800	5324.086	161.8	-10.6	2
361	357.288	5323.487	158.5	-10.9	2
362	357.148	5322.860	143.6	-11.2	2
363	356.505	5321.986	144.5	-9.9	2
364	356.114	5321.273	153.3	-9.8	2
365	356.344	5320.526	156.7	-9.6	2
366	356.326	5319.805	146.9	-12.0	2
367	355.931	5318.943	123.4	-12.3	2
368	355.298	5318.514	137.2	-12.3	2
369	354.794	5318.230	132.9	-12.6	2
370	354.290	5318.002	140.2	-12.4	2
371	353.655	5317.462	135.9	-12.5	2
372	353.636	5316.739	121.6	-11.7	2
373	353.367	5315.931	119.2	-12.2	2
374	353.222	5315.137	155.1	-12.1	2
375	353.452	5314.409	147.2	-12.0	2
376	353.683	5313.680	106.7	-11.1	2
377	353.663	5312.902	46.9	-10.2	2
378	353.272	5312.226	43.3	-9.4	2
379	352.758	5311.609	45.4	-8.8	2
380	352.125	5311.180	44.5	-9.4	2
381	351.366	5310.755	39.9	-9.9	2
382	350.854	5310.194	36.6	-9.6	2
383	350.709	5309.400	58.5	-8.9	2
384	349.949	5308.938	60.0	-9.0	2
385	349.196	5308.717	43.0	-9.6	2
386	348.562	5308.326	44.2	-9.9	2
387	348.301	5307.851	62.2	-9.7	2
388	347.661	5307.219	62.5	-10.2	2
389	347.030	5306.920	64.9	-11.0	2
390	346.395	5306.492	61.6	-11.3	2
391	345.642	5306.309	44.5	-11.6	2
392	344.893	5306.275	33.2	-11.8	2
393	344.145	5306.275	25.9	-12.1	2
394	343.262	5305.891	35.4	-12.2	2
395	342.623	5305.334	38.4	-12.9	2

Appendix A2.1

Station	Easting (km)	Northing (km)	Elevation (m)	Bouguer Anomaly (mGal)	Source Code
396	342.354	5304.618	22.9	-14.1	2
397	341.959	5303.832	21.9	-15.1	2
398	341.324	5303.441	18.0	-15.1	2
399	340.689	5303.014	30.2	-15.7	2
400	340.048	5302.383	65.8	-16.3	2
401	339.535	5301.878	64.6	-16.2	2
402	338.773	5301.417	63.7	-15.9	2
403	338.136	5300.953	58.5	-15.5	2
404	337.380	5300.696	50.9	-14.8	2
405	336.991	5300.170	50.0	-14.9	2
406	336.352	5299.632	37.2	-15.2	2
407	335.714	5299.168	31.4	-15.3	2
408	335.194	5298.422	20.7	-15.7	2
409	334.681	5297.937	12.5	-17.1	2
410	334.165	5297.358	18.9	-17.8	2
411	333.773	5296.758	13.7	-18.1	2
412	333.008	5296.224	9.1	-17.3	2
413	332.988	5295.538	6.4	-17.7	2
414	333.228	5295.198	13.7	-17.7	2
415	332.706	5294.416	16.2	-15.4	2
416	332.066	5293.878	14.6	-14.3	2
417	331.307	5293.566	8.5	-14.5	2
418	330.795	5293.173	4.6	-14.4	2
419	330.277	5292.558	4.9	-15.1	2
420	329.884	5291.921	13.4	-16.1	2
421	329.613	5291.206	21.6	-17.4	2
422	329.215	5290.439	24.7	-17.3	2
423	329.069	5289.720	32.9	-15.0	2
424	328.549	5289.050	40.5	-11.8	2
425	327.786	5288.627	26.5	-11.7	2
426	327.394	5288.083	29.6	-9.7	2
427	327.122	5287.331	32.0	-8.4	2
428	326.724	5286.564	25.6	-6.0	2
429	326.574	5285.735	18.6	-3.5	2
430	326.548	5284.883	43.9	-0.4	2
431	326.902	5284.149	43.3	0.4	2
432	327.638	5283.645	37.5	-1.1	2
433	327.616	5282.886	14.6	-1.5	2
434	327.850	5282.341	18.3	-2.8	2
435	328.462	5281.878	29.9	-0.1	2
436	328.823	5281.386	52.7	2.3	2
437	329.182	5280.819	59.7	3.8	2
438	330.058	5280.793	65.2	4.0	2

Appendix A2.1

Station	Easting (km)	Northing (km)	Elevation (m)	Bouguer Anomaly (mGal)	Source Code
439	330.800	5280.438	95.1	4.5	2
440	331.664	5280.005	110.0	3.6	2
441	332.022	5279.401	96.6	4.0	2
442	331.999	5278.605	54.3	3.1	2
443	331.975	5277.753	64.3	3.0	2
444	331.827	5276.997	36.3	3.4	2
445	332.442	5276.572	19.8	2.9	2
446	332.930	5276.113	24.1	4.7	2
447	333.547	5275.780	20.4	5.6	2
448	333.786	5275.365	15.5	8.1	2
449	334.659	5275.211	31.7	9.0	2
450	335.409	5275.152	21.0	10.0	2
451	336.154	5274.890	17.4	10.5	2
452	336.767	5274.391	27.4	11.1	2
453	337.379	5273.855	37.2	12.5	2
454	337.233	5273.136	7.9	12.4	2
455	337.597	5272.681	15.2	12.3	2
500	374.500	5345.540	122.8	-12.5	3
501	375.375	5344.920	104.2	-13.7	3
502	376.390	5344.605	117.3	-14.6	3
503	377.400	5344.330	127.1	-16.3	3
504	378.330	5344.040	126.2	-16.4	3
505	379.060	5343.565	144.8	-15.8	3
506	379.930	5343.080	157.6	-15.6	3
507	380.840	5342.630	167.9	-15.9	3
508	381.710	5342.100	178.3	-17.3	3
509	382.470	5341.510	177.4	-18.1	3
510	383.300	5340.875	185.0	-17.0	3
511	384.375	5340.360	201.5	-15.4	3
512	385.490	5339.690	179.2	-14.4	3
513	386.505	5339.590	144.8	-13.6	3
514	387.490	5339.515	164.3	-12.0	3
515	388.510	5339.465	152.7	-11.5	3
516	389.520	5339.290	164.9	-9.2	3
517	390.975	5338.950	159.7	-7.5	3
518	383.480	5342.530	201.8	-20.2	3
519	382.750	5343.960	194.5	-20.4	3
520	366.740	5339.825	68.0	-20.2	3
521	367.505	5339.415	77.1	-19.6	3
522	368.400	5339.350	90.2	-18.4	3
523	369.865	5339.735	109.4	-16.9	3
524	370.640	5339.550	98.8	-17.6	3
525	371.900	5338.625	115.8	-15.4	3

Appendix A2.1

Station	Easting (km)	Northing (km)	Elevation (m)	Bouguer Anomaly (mGal)	Source Code
526	373.030	5338.410	107.0	-15.0	3
527	374.025	5337.965	127.7	-14.4	3
528	374.900	5337.630	160.6	-14.2	3
529	376.000	5337.160	186.2	-14.1	3
530	376.855	5336.350	175.9	-13.8	3
531	377.860	5335.540	190.5	-15.8	3
532	378.275	5335.150	196.6	-17.8	3
533	379.250	5335.145	198.7	-18.7	3
534	380.010	5334.965	182.0	-19.0	3
535	380.980	5334.910	176.2	-17.4	3
536	368.135	5336.425	55.2	-17.0	3
537	365.365	5337.600	62.5	-22.3	3
538	363.135	5338.230	47.9	-27.0	3
539	362.175	5339.425	28.7	-29.5	3
540	361.010	5340.940	25.0	-26.4	3
541	360.510	5339.940	24.1	-27.2	3
542	361.575	5336.450	38.4	-25.2	3
543	359.875	5334.490	59.1	-21.9	3
544	357.010	5336.000	25.6	-26.5	3
545	355.400	5335.140	13.7	-23.9	3
546	353.485	5333.300	35.4	-19.6	3
547	356.975	5337.925	26.5	-26.1	3
548	359.275	5338.450	27.7	-25.9	3
549	379.250	5350.830	78.9	-14.2	3
550	382.000	5349.800	136.2	-16.4	3
551	382.500	5349.450	135.3	-20.3	3
552	383.000	5349.640	131.1	-21.6	3
553	386.530	5349.470	197.8	-20.7	3
554	388.920	5348.370	258.5	-15.4	3
555	387.710	5347.010	307.8	-12.6	3
556	368.380	5345.220	40.8	-21.7	3
557	366.620	5345.960	42.4	-24.1	3
558	368.810	5348.210	21.3	-21.3	3
559	370.960	5350.090	10.4	-19.0	3
560	365.520	5343.100	33.8	-23.3	3
561	363.440	5343.470	22.6	-24.8	3
562	364.680	5340.530	50.0	-24.2	3
563	369.240	5336.380	76.5	-13.3	3
564	370.220	5335.590	71.6	-12.2	3
565	371.910	5334.640	96.6	-12.7	3
566	372.510	5332.330	116.1	-13.9	3
567	374.110	5330.330	125.0	-12.3	3
568	375.620	5328.810	107.0	-3.5	3

Appendix A2.1

Station	Easting (km)	Northing (km)	Elevation (m)	Bouguer Anomaly (mGal)	Source Code
569	377.300	5330.830	244.1	-6.8	3
570	365.550	5333.570	55.2	-11.7	3
571	374.890	5357.005	0.9	-23.8	3
572	377.710	5357.000	56.7	-25.1	3
573	380.425	5357.060	96.3	-12.1	3
575	386.510	5356.660	114.9	-10.6	3
576	391.675	5357.250	250.5	-14.3	3
577	395.490	5356.950	339.2	-11.6	3
578	397.475	5356.800	243.5	-7.1	3
579	400.690	5356.735	362.1	-0.1	3
580	403.995	5356.900	82.3	-1.2	3
581	406.340	5356.500	94.2	4.6	3
582	403.865	5354.150	406.0	8.5	3
583	401.350	5354.360	234.1	0.3	3
584	395.075	5354.080	376.1	-8.2	3
585	391.915	5353.660	251.5	-13.4	3
586	384.300	5354.100	151.2	-16.1	3
587	381.450	5354.300	107.9	-11.5	3
588	377.660	5354.560	50.6	-22.7	3
589	374.870	5354.970	4.0	-22.9	3
590	388.400	5350.950	167.9	-19.7	3
591	391.220	5350.810	194.2	-14.4	3
592	395.375	5351.350	400.8	-5.9	3
593	397.990	5351.275	435.3	0.2	3
594	401.560	5351.315	435.9	6.1	3
595	399.875	5348.760	449.0	5.8	3
596	396.950	5348.215	330.7	1.1	3
597	397.610	5346.025	470.9	5.2	3
598	392.830	5348.760	343.2	-9.2	3
599	393.175	5347.330	460.9	-8.3	3
600	391.620	5344.275	438.3	-5.2	3
601	394.360	5342.150	350.5	3.3	3
602	392.090	5339.905	378.3	0.9	3
603	390.355	5336.805	444.4	3.4	3
604	388.510	5334.935	410.6	5.3	3
605	386.725	5332.700	293.5	5.7	3
606	384.650	5330.320	293.2	6.6	3
607	382.990	5328.050	444.7	10.3	3
608	380.380	5325.540	346.9	13.2	3
609	379.300	5323.635	345.6	11.6	3
610	376.830	5320.900	450.8	20.8	3
611	373.600	5322.240	453.8	13.5	3
612	375.705	5323.640	490.1	15.8	3

Appendix A2.1

Station	Easting (km)	Northing (km)	Elevation (m)	Bouguer Anomaly (mGal)	Source Code
613	377.140	5325.850	99.4	8.4	3
614	378.645	5327.175	306.0	8.4	3
615	381.190	5329.920	345.3	4.6	3
616	383.190	5332.430	253.6	-3.6	3
617	385.255	5335.140	253.6	-5.0	3
618	387.525	5337.835	289.3	-5.4	3
619	384.675	5338.400	296.6	-10.1	3
620	384.160	5348.245	213.4	-20.3	3
621	380.640	5347.885	186.8	-17.0	3
622	378.950	5345.800	179.8	-14.8	3
623	381.160	5345.870	199.3	-17.3	3
624	383.550	5346.015	222.5	-19.1	3
625	386.655	5345.210	268.5	-16.4	3
626	388.840	5344.010	313.9	-9.1	3
627	386.550	5341.685	294.1	-10.9	3
628	381.190	5339.700	197.5	-15.9	3
629	378.580	5341.330	85.3	-17.6	3
630	376.000	5341.800	148.7	-14.9	3
631	373.740	5342.615	101.2	-14.4	3
632	370.930	5341.600	50.0	-16.3	3
633	373.035	5340.715	73.2	-16.3	3
634	374.900	5339.500	94.5	-15.9	3
635	377.625	5338.200	117.3	-16.4	3
636	379.845	5336.350	151.8	-16.2	3
637	383.180	5336.570	219.5	-13.7	3
638	381.860	5333.830	229.5	-13.3	3
639	379.690	5332.730	226.8	-15.5	3
640	378.130	5333.055	210.9	-18.1	3
641	375.450	5334.725	158.5	-15.3	3
642	374.850	5332.870	164.0	-14.6	3
643	372.950	5336.055	118.9	-12.9	3
644	370.400	5337.310	62.8	-14.7	3
645	369.800	5332.460	166.1	-11.1	3
646	370.420	5330.800	218.5	-15.0	3
647	372.090	5328.460	236.2	-5.4	3
648	374.070	5325.535	328.3	3.3	3
649	372.090	5325.915	292.6	-1.5	3
650	371.330	5323.575	207.3	1.5	3
651	369.050	5327.890	116.1	-10.2	3
652	376.460	5351.530	56.7	-13.7	3
653	374.495	5349.710	55.2	-11.4	3
654	371.235	5347.270	50.6	-17.6	3
655	368.060	5343.045	36.9	-15.9	3

Appendix A2.1

Station	Easting (km)	Northing (km)	Elevation (m)	Bouguer Anomaly (mGal)	Source Code
656	365.340	5335.745	107.0	-19.1	3
657	362.495	5335.005	36.3	-21.8	3
658	356.735	5333.895	53.3	-22.2	3
659	361.010	5332.765	75.6	-20.3	3
660	360.310	5330.750	376.4	-12.7	3
661	357.280	5330.225	307.5	-9.9	3
662	363.230	5331.010	282.9	-15.1	3
663	361.600	5328.155	385.3	-7.9	3
700	371.000	5377.690	18.9	-0.9	4
701	368.850	5376.750	31.7	1.0	4
702	366.250	5376.500	21.0	4.1	4
703	364.225	5376.105	35.1	8.8	4
704	361.775	5375.940	22.6	9.4	4
705	359.675	5375.375	42.1	10.5	4
706	358.100	5376.290	69.5	12.4	4
707	355.835	5375.590	39.3	13.5	4
708	353.615	5375.525	41.1	14.1	4
709	351.890	5376.050	13.1	13.7	4
710	350.000	5376.650	107.0	13.0	4
711	347.960	5375.810	22.3	13.0	4
712	346.000	5375.375	43.3	11.0	4
713	343.725	5374.460	30.8	8.9	4
714	341.555	5373.425	25.6	10.2	4
715	339.335	5372.580	23.5	9.1	4
716	337.360	5371.700	13.1	7.7	4
717	335.930	5370.825	14.6	5.1	4
718	332.300	5370.250	17.4	2.9	4
719	358.280	5378.665	19.2	12.4	4
720	358.950	5380.685	8.8	9.0	4
721	359.500	5382.930	31.4	6.7	4
722	357.610	5383.735	9.1	5.2	4
723	355.835	5384.865	11.3	3.6	4
724	354.600	5386.750	17.7	0.2	4
725	354.290	5388.725	13.4	-3.5	4
726	352.760	5390.025	32.0	-5.8	4
727	350.620	5389.515	47.5	-6.0	4
728	348.360	5388.725	66.1	-6.7	4
729	346.375	5387.695	14.9	-4.7	4
730	344.570	5386.425	1.8	-2.1	4
731	342.550	5384.820	47.2	0.1	4
732	340.730	5383.285	18.0	-0.9	4
733	339.445	5381.790	5.5	-0.8	4
734	338.575	5380.350	4.3	0.6	4

Appendix A2.1

Station	Easting (km)	Northing (km)	Elevation (m)	Bouguer Anomaly (mGal)	Source Code
735	354.100	5391.675	33.8	-9.0	4
736	356.200	5393.465	18.6	-11.5	4
737	357.770	5394.835	19.8	-11.1	4
738	359.330	5394.525	31.4	-12.5	4
739	361.160	5396.225	19.8	-15.2	4
740	363.290	5398.275	19.5	-17.8	4
741	365.670	5400.585	15.2	-20.3	4
742	368.250	5402.870	6.1	-23.2	4
743	371.175	5379.585	12.2	0.3	4
744	370.035	5379.480	59.1	2.6	4
745	367.760	5380.110	19.8	4.8	4
746	365.760	5380.500	26.8	6.0	4
747	364.875	5381.985	7.3	3.7	4
748	369.226	5378.770	65.5	2.8	4
749	373.625	5379.425	37.8	-2.8	4
750	374.710	5381.235	83.8	-3.3	4
751	375.725	5383.320	52.7	-4.7	4
752	376.650	5385.500	11.9	-5.8	4
753	377.675	5387.360	11.3	-7.4	4
754	378.250	5389.535	7.0	-10.3	4
755	376.210	5391.735	12.2	-13.5	4
756	375.880	5393.770	6.7	-15.7	4
757	376.335	5394.700	5.2	-16.0	4
758	378.650	5391.460	25.3	-13.5	4
759	377.925	5393.340	64.3	-15.2	4
760	375.740	5379.315	42.4	-7.9	4
761	378.050	5378.790	24.1	-12.0	4
762	380.525	5378.325	25.3	-13.4	4
763	383.425	5380.150	44.8	-18.5	4
764	385.155	5381.515	94.5	-20.1	4
765	387.300	5380.475	56.1	-20.9	4
766	389.350	5379.875	32.6	-19.9	4
767	391.625	5379.565	44.8	-14.5	4
768	393.780	5378.525	42.1	-12.0	4
769	395.950	5378.400	31.1	-15.9	4
770	397.445	5379.700	36.6	-16.4	4
771	399.200	5381.225	34.4	-18.4	4
772	401.400	5381.075	48.5	-20.4	4
773	403.560	5381.475	54.9	-21.4	4
774	406.090	5383.275	82.6	-19.7	4
775	408.075	5383.850	95.4	-19.2	4
776	397.475	5382.690	59.4	-17.7	4
777	386.950	5383.180	124.1	-17.6	4

Appendix A2.1

Station	Easting (km)	Northing (km)	Elevation (m)	Bouguer Anomaly (mGal)	Source Code
778	382.275	5380.775	61.3	-15.7	4
779	383.625	5377.415	4.9	-19.5	4
780	381.995	5378.200	17.1	-17.0	4
781	385.315	5375.850	5.2	-24.0	4
782	386.230	5374.075	4.0	-24.3	4
783	385.660	5379.525	25.3	-20.1	4
784	387.945	5378.825	31.4	-22.4	4
785	386.590	5377.535	10.7	-22.7	4
786	387.700	5375.950	7.3	-24.2	4
787	389.220	5377.320	32.3	-16.0	4
788	390.245	5375.675	114.0	-11.9	4
789	391.935	5375.050	7.9	-10.2	4
790	392.400	5377.325	56.7	-10.6	4
791	393.895	5373.175	3.0	-17.7	4
792	395.090	5375.095	13.7	-17.4	4
793	395.480	5377.425	20.1	-16.4	4
794	394.725	5370.950	2.4	-16.3	4
795	395.300	5368.625	9.8	-17.1	4
796	396.725	5366.715	21.9	-19.7	4
797	406.760	5370.335	26.2	-17.1	4
798	407.575	5371.450	35.1	-14.8	4
799	329.640	5293.915	14.9	-15.0	4
800	327.400	5293.060	11.3	-15.9	4
801	325.925	5293.320	7.9	-16.6	4
802	328.745	5296.105	77.4	-13.1	4
803	327.790	5298.315	73.8	-11.1	4
804	326.070	5299.465	1.2	-11.2	4
805	325.770	5297.225	22.9	-14.0	4
806	325.415	5295.520	16.5	-15.6	4
807	324.800	5301.125	18.0	-10.4	4
808	323.860	5303.120	51.5	-8.8	4
809	322.360	5304.164	41.5	-6.7	4
810	320.765	5306.290	25.6	-3.8	4
811	319.800	5307.735	11.3	-3.9	4
812	320.295	5309.100	35.7	-5.9	4
813	333.375	5300.340	26.8	-15.5	4
814	331.545	5301.175	8.8	-10.2	4
815	329.350	5300.635	1.8	-10.0	4
816	327.450	5299.790	21.9	-10.7	4
817	326.340	5302.310	5.2	-8.3	4
818	328.235	5302.155	7.6	-9.2	4
819	330.445	5302.220	39.6	-8.9	4
820	332.700	5302.555	18.6	-8.4	4

Appendix A2.1

Station	Easting (km)	Northing (km)	Elevation (m)	Bouguer Anomaly (mGal)	Source Code
821	334.830	5303.405	11.6	-11.6	4
822	336.900	5304.245	19.5	-11.5	4
823	335.150	5301.090	4.3	-17.6	4
824	331.125	5298.520	95.4	-13.3	4
825	330.450	5296.315	95.1	-13.9	4
826	331.745	5294.845	5.8	-15.0	4
827	397.180	5371.725	9.4	-20.5	4
828	394.450	5368.990	15.2	-16.4	4
829	393.800	5366.880	17.1	-17.1	4
830	391.960	5365.800	29.3	-17.0	4
831	390.230	5364.650	15.2	-15.5	4
832	387.625	5363.860	14.0	-12.4	4
833	385.825	5363.475	21.3	-9.8	4
834	383.600	5362.945	12.8	-13.3	4
835	391.925	5362.675	91.1	-17.1	4
836	388.650	5359.925	49.1	-15.6	4
837	386.430	5359.925	61.3	-13.1	4
838	384.000	5359.600	50.3	-9.5	4
839	394.835	5359.050	61.3	-13.8	4
840	396.845	5358.255	66.1	-13.4	4
841	398.750	5358.310	64.0	-11.2	4
842	401.175	5358.950	67.1	-8.9	4
843	403.680	5358.035	84.4	-0.9	4
844	382.175	5359.625	39.6	-11.5	4
845	382.335	5361.675	26.5	-16.0	4
846	380.090	5361.500	16.8	-24.0	4
847	378.240	5360.020	34.1	-24.2	4
848	376.425	5358.625	43.3	-24.0	4
849	375.375	5356.980	54.9	-24.7	4
850	378.265	5357.920	39.0	-23.9	4
851	341.790	5375.660	332.8	9.2	4
852	338.245	5375.740	209.1	6.0	4
853	341.540	5380.770	134.7	5.6	4
854	345.925	5379.425	287.4	10.0	4
855	349.805	5384.980	85.3	4.8	4
856	353.300	5381.625	114.3	10.4	4
857	355.125	5378.780	113.4	13.5	4
858	361.260	5380.285	5.2	9.1	4
859	383.725	5393.780	214.0	-12.9	4
860	386.640	5393.260	307.5	-14.0	4
861	387.553	5389.110	360.6	-13.4	4
862	381.750	5389.855	387.4	-11.3	4
863	381.540	5386.500	122.5	-12.3	4

Appendix A2.1

Station	Easting (km)	Northing (km)	Elevation (m)	Bouguer Anomaly (mGal)	Source Code
864	385.805	5386.285	329.5	-13.5	4
865	380.640	5381.710	99.4	-11.3	4
866	407.325	5390.600	113.7	-14.7	4
867	407.255	5386.400	153.3	-16.4	4
868	403.230	5387.925	109.7	-17.5	4
869	402.985	5384.150	46.0	-20.7	4
870	399.650	5384.175	61.0	-18.5	4
871	399.925	5388.090	174.7	-17.3	4
872	401.875	5392.345	254.5	-13.6	4
873	395.600	5391.875	492.3	-13.7	4
874	395.035	5387.730	444.4	-19.0	4
875	390.720	5387.100	387.4	-16.3	4
876	388.785	5383.330	191.1	-17.6	4
877	394.075	5383.230	296.0	-18.0	4
878	403.080	5379.030	64.0	-21.2	4
879	400.415	5370.925	38.4	-19.5	4
880	411.450	5384.575	267.6	-11.6	4
881	411.800	5379.275	136.2	-14.7	4
882	409.695	5376.565	39.9	-18.2	4
883	409.675	5373.035	68.3	-12.2	4
884	405.775	5368.190	319.4	-11.7	4
885	407.625	5362.990	397.5	2.2	4
886	402.930	5361.090	357.8	-2.0	4
887	400.045	5364.780	215.5	-16.5	4
888	396.930	5362.570	221.6	-12.9	4
889	388.650	5362.260	79.6	-12.7	4
890	350.370	5328.565	465.7	-8.2	4
891	354.755	5324.335	545.0	-9.9	4
892	351.140	5320.745	406.6	-9.4	4
893	347.425	5322.560	392.9	-6.2	4
894	343.300	5322.800	452.6	-5.4	4
895	343.980	5316.390	402.6	-6.8	4
896	339.850	5320.225	421.2	-3.6	4
897	337.080	5314.810	430.4	-3.5	4
898	335.880	5308.175	372.5	-9.2	4
899	330.585	5310.735	430.7	-3.4	4
900	326.425	5310.590	134.7	-3.6	4
901	323.820	5306.625	417.9	-3.6	4
902	326.535	5306.520	226.8	-2.8	4
903	330.865	5305.875	34.4	-8.2	4
904	334.810	5305.580	46.9	-8.2	4
905	340.160	5308.450	384.7	-8.4	4
906	338.705	5311.305	406.9	-5.6	4

Appendix A2.1

Station	Easting (km)	Northing (km)	Elevation (m)	Bouguer Anomaly (mGal)	Source Code
907	345.150	5312.095	455.7	-8.1	4
908	348.580	5314.450	84.1	-10.5	4
909	356.505	5316.625	258.8	-8.3	4
910	359.995	5316.095	249.6	-5.2	4
911	364.380	5318.765	183.8	-4.1	4
912	368.935	5321.060	251.2	4.8	4
913	364.535	5322.760	467.6	-4.7	4
914	359.465	5321.150	360.6	-8.5	4
915	358.205	5326.335	424.9	-9.7	4
916	354.580	5328.210	437.1	-8.0	4
917	350.955	5324.570	456.6	-7.8	4
918	346.430	5325.625	396.8	-6.1	4
919	343.580	5325.895	458.4	-8.6	4
920	348.125	5328.775	384.7	-11.3	4
921	399.700	5375.675	86.9	-20.2	4
922	359.130	5379.815	4.6	9.7	4
923	359.855	5379.725	3.7	9.8	4
924	360.620	5379.825	3.0	9.2	4
925	361.600	5380.580	3.4	8.0	4
926	362.255	5381.260	3.7	6.2	4
927	362.680	5381.980	3.7	4.9	4
928	363.475	5382.020	14.3	4.4	4
929	364.315	5382.000	18.3	4.5	4
930	341.055	5324.315	452.9	-12.5	4
931	338.745	5322.955	420.3	-12.6	4
932	335.970	5320.080	376.4	-8.2	4
933	332.130	5318.395	358.7	-10.7	4
934	332.575	5315.275	381.9	-5.6	4
935	329.320	5313.160	403.3	-6.8	4
936	332.630	5306.905	64.3	-8.2	4
937	334.620	5310.440	410.0	-4.7	4
938	340.815	5317.510	466.3	-3.9	4
939	343.710	5319.725	451.7	-5.7	4
940	347.815	5318.235	182.9	-9.3	4
941	351.400	5317.350	170.1	-9.7	4
942	368.065	5317.725	343.8	18.6	4
943	364.720	5315.830	447.1	10.5	4
944	362.285	5314.075	437.7	9.6	4
945	358.970	5312.335	355.1	3.5	4
946	356.815	5310.760	411.5	1.7	4
947	354.700	5308.655	462.7	16.2	4
948	352.340	5307.425	577.9	15.3	4
949	349.380	5305.085	499.3	11.4	4

Appendix A2.1

Station	Easting (km)	Northing (km)	Elevation (m)	Bouguer Anomaly (mGal)	Source Code
950	345.235	5301.910	434.6	-0.1	4
951	341.380	5298.605	355.1	-10.7	4
952	337.895	5295.430	424.3	-5.0	4
953	335.260	5293.395	541.9	-2.7	4
7201	318.760	5313.487	-85.0	-17.0	5
7202	324.465	5313.069	-47.0	-12.5	5
7203	324.670	5318.569	-91.0	-13.9	5
7204	324.849	5324.033	-93.0	-28.6	5
7205	325.244	5329.657	-144.0	-12.9	5
7206	330.891	5334.994	-148.0	-7.6	5
7207	336.579	5340.409	-140.0	-0.9	5
7208	330.968	5340.535	-98.0	1.7	5
7209	330.737	5329.344	-120.0	-20.6	5
7210	336.346	5329.218	-91.0	-20.4	5
7211	325.432	5340.701	-135.0	-2.4	5
7212	324.964	5335.524	-118.0	-3.2	5
7213	336.371	5335.279	-137.0	-13.5	5
7214	341.911	5329.247	-56.0	-19.3	5
7215	342.052	5334.823	-100.0	-19.1	5
7216	341.825	5340.520	-131.0	-7.3	5
7217	342.237	5345.978	-124.0	-3.0	5
7218	342.623	5351.454	-102.0	-7.0	5
7219	342.640	5356.978	-71.0	2.8	5
7220	342.721	5362.574	-93.0	0.8	5
7221	342.785	5367.986	-76.0	4.2	5
7222	348.728	5367.916	-86.0	2.3	5
7223	354.090	5367.813	-86.0	2.9	5
7224	348.282	5362.330	-97.0	-0.1	5
7225	353.923	5362.293	-91.0	-1.8	5
7226	348.197	5356.827	-100.0	0.3	5
7227	353.716	5356.682	-109.0	-7.7	5
7228	359.352	5356.743	-111.0	-13.8	5
7229	359.488	5362.227	-93.0	-5.6	5
7230	359.662	5367.727	-74.0	-0.8	5
7231	365.260	5367.721	-40.0	-8.3	5
7232	365.065	5362.147	-64.0	-13.4	5
7233	364.935	5356.682	-80.0	-16.7	5
7234	370.656	5362.146	-31.0	-19.5	5
7235	370.745	5367.630	-27.0	-16.2	5
7236	376.267	5367.581	-53.0	-21.2	5
7237	376.424	5373.063	-27.0	-18.8	5
7238	381.929	5373.020	-51.0	-22.8	5
7239	381.799	5367.389	-89.0	-26.0	5

Appendix A2.1

Station	Easting (km)	Northing (km)	Elevation (m)	Bouguer Anomaly (mGal)	Source Code
7240	375.220	5362.563	-53.0	-24.0	5
7241	370.883	5373.150	-23.0	-8.6	5
7242	365.329	5373.224	-27.0	3.6	5
7243	359.775	5373.304	-42.0	7.8	5
7244	355.367	5371.469	-65.0	9.0	5
7245	349.800	5371.595	-58.0	8.5	5
7246	344.220	5371.728	-53.0	10.3	5
7247	342.809	5367.966	-76.0	3.9	5
7248	337.378	5368.231	-60.0	6.7	5
7249	331.793	5368.339	-82.0	5.1	5
7250	326.232	5368.414	-87.0	0.4	5
7251	320.751	5368.678	-89.0	-6.3	5
7252	315.098	5368.582	-102.0	-8.4	5
7253	309.662	5369.096	-126.0	-11.1	5
7254	303.990	5369.215	-173.0	-12.3	5
7255	303.983	5363.652	-210.0	-12.7	5
7256	303.692	5358.098	-170.0	-10.2	5
7257	303.523	5352.485	-153.0	-9.4	5
7258	303.280	5346.893	-177.0	-12.7	5
7259	303.135	5341.260	-171.0	-11.7	5
7260	302.932	5335.722	-188.0	-14.7	5
7261	302.656	5330.242	-314.0	-25.3	5
7262	302.566	5324.738	-226.0	-15.2	5
7263	302.378	5319.274	-274.0	-14.1	5
7264	302.066	5313.814	-332.0	-20.8	5
7265	307.814	5313.582	-204.0	-16.6	5
7266	308.175	5319.170	-219.0	-20.5	5
7267	308.307	5324.636	-224.0	-15.3	5
7268	308.528	5330.117	-234.0	-14.7	5
7269	308.696	5335.526	-204.0	-21.1	5
7270	308.877	5341.287	-190.0	-9.4	5
7271	309.086	5346.788	-120.0	-11.8	5
7272	309.248	5352.364	-124.0	-7.2	5
7273	309.447	5357.939	-153.0	-7.7	5
7274	309.633	5363.459	-148.0	-10.8	5
7275	309.727	5368.834	-128.0	-10.9	5
7276	314.934	5363.191	-144.0	-8.1	5
7277	314.791	5357.670	-133.0	-5.8	5
7278	314.537	5352.171	-122.0	-5.8	5
7279	314.417	5346.593	-104.0	-9.6	5
7280	314.201	5341.093	-146.0	-8.2	5
7281	313.996	5335.537	-164.0	-14.1	5
7282	313.892	5330.052	-157.0	-10.0	5

Appendix A2.1

Station	Easting (km)	Northing (km)	Elevation (m)	Bouguer Anomaly (mGal)	Source Code
7283	313.598	5324.443	-184.0	-17.4	5
7284	313.443	5318.923	-171.0	-21.6	5
7285	313.216	5313.460	-139.0	-25.1	5
7286	318.912	5313.148	-75.0	-15.5	5
7287	318.888	5318.730	-93.0	-21.9	5
7288	319.109	5324.174	-155.0	-23.7	5
7289	330.585	5323.805	-80.0	-15.6	5
7290	335.219	5324.560	-53.0	-15.5	5
7291	319.324	5329.804	-139.0	-10.3	5
7292	319.811	5335.388	-151.0	-4.4	5
7293	319.606	5341.087	-118.0	-15.4	5
7294	319.859	5346.752	-85.0	-6.1	5
7295	320.188	5352.063	-122.0	-0.8	5
7296	320.266	5357.661	-120.0	0.4	5
7297	320.304	5363.148	-115.0	-2.1	5
7298	326.114	5362.967	-85.0	5.7	5
7299	325.933	5357.465	-109.0	4.5	5
7300	325.677	5351.930	-71.0	2.7	5
7301	325.529	5346.279	-111.0	-4.1	5
7302	325.562	5340.475	-137.0	-1.0	5
7303	331.175	5346.257	-120.0	0.7	5
7304	331.387	5351.757	-87.0	5.5	5
7305	331.552	5357.296	-89.0	5.8	5
7306	331.876	5362.811	-82.0	3.8	5
7307	337.278	5362.635	-87.0	2.6	5
7308	337.097	5357.171	-85.0	5.8	5
7309	336.950	5351.614	-111.0	1.9	5
7310	336.753	5346.039	-69.0	-3.8	5
7311	336.667	5340.443	-140.0	-1.9	5
7312	347.712	5334.484	-60.0	-26.0	5
7313	347.957	5339.964	-111.0	-17.8	5
7314	347.745	5345.920	-122.0	-5.8	5
7315	347.980	5351.475	-82.0	-13.7	5
7316	353.954	5351.004	-122.0	-14.6	5
7317	353.478	5345.492	-109.0	-15.0	5
7318	353.421	5339.914	-49.0	-24.1	5
7319	358.954	5345.632	-51.0	-19.8	5
7320	359.143	5351.281	-104.0	-13.6	5
7321	364.356	5351.061	-53.0	-19.6	5
7322	370.494	5356.664	-31.0	-20.9	5

Source Code Legend

Code	Source
1	Weaver, 1969
2	Weir, 1971
3	Land Stations, 1983
4	Land Stations, 1984
5	Underwater, 1985

Appendix A2.2

```
C
C                    PROGRAM: GN.FOR
C
C     2-D/2.5-D LEAST-SQUARES GRAVITY INVERSION PROGRAM
C          Talwani; Rasmussen and Pedersen Formulation
C                (constraints on the Z-variable)
C     Ref:
C          J. Geoph. Res., 64 (1959), pp. 49-59.
C          Geophysics, 42 (1977), pp. 1053-1055.
C          Geoph. Prosp., 27 (1979), pp. 749-760.
C          Geophysics, 52 (1987), pp. 232-238.
C                                   Author:  G.J. Kilfoil
C                                   Written: February, 1986
C                                   Revised: February, 1987
C
C   This program is designed to invert a gravity profile by calculating
C  the unknown coordinates of a "best-fit" Talwani-type polygonal body in
C  the subsurface.  In this program version, the unknown parameters are the
C  coefficients, A  and B , of a linear regional field of the form Ax + B ,
C  and the z coordinates of a body above or below a reference level, Z_o
C  (ZT in the program).
C
C  Subroutines called:
C    ZXSSQ ..... Member of the IMSL standard subroutines.  Performs damped
C                least squares inversion on the matrix, GG(*,*), containing
C                partial first derivatives of the gravity effect with
C                respect to unknown body parameters.  Dimensioned variables
C                G(*,*), XJTJ(*), WORK(*), PARM(*) are arguemnts to ZXSSQ
C                used as temporary storage locations during inversion.  Other
C                arguments contain convergence criteria (input from a data
C                file) and termination error coding.
C    GCAL2 ..... External routine iteratively called by ZXSSQ to evaluate
C                the gravity effect of a 2-D body.
C    GCAL25 .... External routine iteratively called by ZXSSQ to evaluate
C                the gravity effect of a 2.5-D body.
C    CHOOSE .... Allows interactive choice of a 2-D or 2.5-D inversion scheme.
C
C    Other routines, HEADER, READER, RITE, RITE1, RITE3, carry out the
C     necesary screen and file I/O.
C
C  Notes:
C    The program must be linked to an IMSL subroutine object library at
C     the user's host facility.
C    Gravity evaluating routines presently assume units of dimension in
C     kilometers and density in gm/cm^3.  Other conventions may be accom-
C     modated by inclusion of appropriate scaling factors.
C    The evaluating routines have been revised to properly treat special
C     cases, such as evaluation of the gravity effect when situated on or
C     within the polygonal causative body, in a manner consistent with
C     algorithms of Won and Bevis, 1987.
C    Known parameters describing the body are passed to the External
C     subroutines through COMMON statements.
```

Appendix A2.2

```
C    A positive ZT indicates the body is to be "grown" downward from the
C      Z_o level, ABS(ZT).  A negative ZT causes the body to evolve upward
C      (-z direction) from the Z_o level, ABS(ZT).
C    Unknown body parameters are constrained to the positive z half-space.
C
     EXTERNAL GCAL2, GCAL25
     PARAMETER (L=100)
     DIMENSION GO(L), C(L), GC(L), Y(L), DG(L), GG(L,L), X(L),
    +          Z(L), ZZ(L), XJTJ(5000), WORK(5000), PARM(4)
     COMMON /VARS/ GTERM, ZT, X, C, GC, GO
     COMMON /VARS2/ Y, Y1, Y2

     GK = 6.673
     CALL HEADER(11,' GN.FOR','GRAVITY ')
     READ(11,901) N, RHO, START, XEND, NBEG, NS, ZT, Y1, Y2
     WRITE(6,901) N, RHO, START, XEND, NBEG, NS, ZT, Y1, Y2
     CALL READER(11,NSIG,EPS,DEL,MAX,IOPT,IFLAG,N,GO,C,Y,PARM)
C
C Initialize variables.
     GTERM = GK*RHO
     FACT = 1.0/(41.9*RHO)
     DO 10 I=1,NS
       J = NS + NBEG - I
       X(I) = C(J)
       Z(I) = ABS(ZT+GO(J)*FACT)
       ZZ(I) = Z(I)
  10 CONTINUE
     X(NS+1) = START
     X(NS+2) = START
     X(NS+3) = XEND
     X(NS+4) = XEND
     CALL RITE(NS,X,Z,RHO)
C
C Choose whether a 2-D or 2.5-D inversion is desired.
  20 CALL CHOOSE(II)
     IF (II.LE.2) THEN          ! Perform inversion.
       IF (II.EQ.0) GOTO 900
       IF (II.EQ.1) CALL ZXSSQ(GCAL2,N,NS,NSIG,EPS,DEL,MAX,IOPT,
    +                  PARM,Z,SSQ,DG,GG,L,XJTJ,WORK,INFER,IER)
       IF (II.EQ.2) CALL ZXSSQ(GCAL25,N,NS,NSIG,EPS,DEL,MAX,IOPT,
    +                  PARM,Z,SSQ,DG,GG,L,XJTJ,WORK,INFER,IER)
     ELSE
       WRITE(6,902)
       GOTO 20
     ENDIF
     CALL RITE1(6,IER,INFER,5,WORK,N,DG)
     WRITE(6,*) ' The Z-values: ', (Z(I),I=1,NS)
C
C  Write data to an output file.
C
     OPEN(12,NAME='GN.OUT',STATUS='UNKNOWN')
     CALL RITE3(N,NS+4,IFLAG,11,12,GO,C,GC,Y,RHO,X,Z,ZZ,ZT)
```

Appendix A2.2

```
      CALL RITE1(12,IER,INFER,5,WORK,N,DG)
  900 CLOSE(UNIT=11)
      CLOSE(UNIT=12)

  901 FORMAT(I5,3F10.3,2I5,3F10.3)
  902 FORMAT(' Value incorrectly typed. Try again:')
      END

C
C The subroutine library for Talwani-type gravity modelling follows.

C -------------------------------------------------------------
      SUBROUTINE GCAL2(Z,N,NS,DG)
C -------------------------------------------------------------
C  Subroutine to evaluate, at N stations, the gravity effect of a 2-D polygonal
C    body having NS variable parameters.
C  Includes treatment of special cases (ie. when on or within the polygonal
C    body) consistent with Won and Bevis, 1987, Geophysics, 52, 232-238.
C
      PARAMETER (L=100, TWO_PI=6.28318530718)
      INTEGER NS, N, M, I
      REAL Z(NS+4), DG(N), X(L), C(L), GC(L), GO(L)
      COMMON /VARS/ GK, ZTT, X, C, GC, GO

      RT = 1.0
      IF (ZTT.LT.0.0) RT = -1.0
      ZT = RT*ZTT
      GRT = GK*RT
      DO 10 I=1,NS
        IF (Z(I).LT.0.0) Z(I) = 0.0
        IF (RT*Z(I).LT.ZTT) Z(I) = ZT
   10 CONTINUE
      Z(NS+1) = Z(NS)
      Z(NS+2) = ZT
      Z(NS+3) = ZT
      Z(NS+4) = Z(1)
      DO 40 M=1,N
        CM = C(M)
        SUM = 0.0
        X1 = X(NS+4) - CM   ! Start body at last vertex
        Z1 = Z(NS+4)
        IF (X1.EQ.0.0 .AND. Z1.EQ.0.0) THEN
          IFLAG = 1
        ELSE
          IFLAG = 0
          AL1 = ALOG(X1*X1+Z1*Z1)
          TH1 = ATAN2(Z1,X1)
        ENDIF
        DO 30 I=1,NS+4
          X2 = X(I) - CM
          Z2 = Z(I)
          IF (X2.EQ.0.0 .AND. Z2.EQ.0.0) THEN
```

Appendix A2.2

```
            IFLAG = 1
            GOTO 30        ! Exit this loop
          ENDIF
          AL2 = ALOG(X2*X2+Z2*Z2)
          TH2 = ATAN2(Z2,X2)
          IF (IFLAG.EQ.1) THEN
            IFLAG = 0
            GOTO 20        ! Exit this loop
          ENDIF

          XZ12 = X1*Z2 - X2*Z1
          IF (SIGN(1.,Z1) .NE. SIGN(1.,Z2)) THEN
            IF (XZ12.GT.0.0) THEN
              IF (Z1.GE.0.0) TH1 = TH1 - TWO_PI
            ELSE IF (XZ12.LT.0.0) THEN
              IF (Z2.GE.0.0) TH1 = TH1 + TWO_PI
            ELSE
              GOTO 20
            ENDIF
          ENDIF

          X21 = X2 - X1
          Z21 = Z2 - Z1
          IF (X21 .EQ. 0.0) THEN
            SUM = SUM + X1*(AL2-AL1)
          ELSEIF (Z21 .EQ. 0.0) THEN
          SUM = SUM - 2.0*Z1*(TH1-TH2)
          ELSE
            SUM = SUM + XZ12*(2.0*X21*(TH1-TH2)+Z21*(AL2-AL1))
     +                /(X21*X21+Z21*Z21)
          ENDIF
   20      X1 = X2
          Z1 = Z2
          AL1 = AL2
          TH1 = TH2
   30    CONTINUE
         GC(M) = GRT*SUM
         DG(M) = GO(M) - GC(M)
   40 CONTINUE
      RETURN
      END

C -------------------------------------------------------------
      SUBROUTINE GCAL25(Z,N,NS,DG)
C -------------------------------------------------------------
C  Subroutine to evaluate, at N stations, the gravity effect of a 2.5-D
C    polygonal body having NS variable parameters.
C  Evaluation is based on the equations of Rasmussen and Pederson (1979) with
C    special cases (ie. when on or within the polygonal body) properly handled
C    in a manner similar to that found in Won and Bevis (1987).
C
      PARAMETER (L=100)
```

Appendix A2.2

```
      INTEGER NS, N, M, I
      REAL Z(NS+4), DG(N), X(L), C(L), GC(L), GO(L), Y(L)
      COMMON /VARS/ GK, ZTT, X, C, GC, GO
      COMMON /VARS2/ Y, YA, YB

      RT = 1.0
      IF (ZTT.LT.0.0) RT = -1.0
      ZT = RT*ZTT
      GRT = GK*RT
      DO 10 I=1,NS
        IF (Z(I).LT.0.0) Z(I) = 0.0
        IF (RT*Z(I).LT.ZTT) Z(I) = ZT
   10 CONTINUE
      Z(NS+1) = Z(NS)
      Z(NS+2) = ZT
      Z(NS+3) = ZT
      Z(NS+4) = Z(1)
C
      DO 40 M=1,N
        CM = C(M)
        S1 = 0.0
        Y1 = Y(M) - YA
        Y2 = YB - Y(M)
        Y1SQ = Y1*Y1
        Y2SQ = Y2*Y2
        AY1 = ABS(Y1)
        AY2 = ABS(Y2)
        X1 = X(NS+4) - CM
        Z1 = Z(NS+4)
        DO 30 I=1,NS+4
          X2 = X(I) - CM
          Z2 = Z(I)
          IF (X2.EQ.X1 .AND. Z2.EQ.Z1) GOTO 30
          IF (X1.EQ.0.0 .AND. Z1.EQ.0.0) THEN
            RR = X2*X2 + Z2*Z2
            RR2 = SQRT(RR)
            IF (Y1 .NE. 0.0) B1 = ALOG((SQRT(RR+Y1SQ)+RR2)/AY1)
            IF (Y2 .NE. 0.0) B2 = ALOG((SQRT(RR+Y2SQ)+RR2)/AY2)
            S1 = S1 + X2*(Y1*B1+Y2*B2)/RR2
            GOTO 20
          ELSEIF (X2.EQ.0.0 .AND. Z2.EQ.0.0) THEN
            RR = X1*X1 + Z1*Z1
            RR2 = SQRT(RR)
            IF (Y1 .NE. 0.0) B1 = ALOG((SQRT(RR+Y1SQ)-RR2)/AY1)
            IF (Y2 .NE. 0.0) B2 = ALOG((SQRT(RR+Y2SQ)-RR2)/AY2)
            S1 = S1 + X1*(Y1*B1+Y2*B2)/RR2
            GOTO 20
          ENDIF
          X21 = X2 - X1
          Z21 = Z2 - Z1
          IF (X21.EQ.0.0 .OR. Z21.EQ.0.0) THEN
            R1SQ = X1*X1 + Z1*Z1
```

Appendix A2.2

```
      R2SQ = X2*X2 + Z2*Z2
      BR11 = SQRT(R1SQ+Y1SQ)
      BR21 = SQRT(R2SQ+Y1SQ)
      BR12 = SQRT(R1SQ+Y2SQ)
      BR22 = SQRT(R2SQ+Y2SQ)
      IF (X21.EQ.0.0) THEN
        S1 = S1 + X1*ALOG((R2SQ*(Y1+BR11)*
     +            (Y2+BR12))/(R1SQ*(Y1+BR21)*(Y2+BR22)))
      ELSE                  ! Case where Z21 = 0.0
        CPHI = SIGN(1.0,X21)
        U1 = X1*CPHI
        U2 = X2*CPHI
        B1 = ALOG((U2+BR21)/(U1+BR11))
        B2 = ALOG((U2+BR22)/(U1+BR12))
        E1 = ATAN2(Z1*Y1*(X2*BR11-X1*BR21),
     +             Z1*Z1*BR21*BR11+X1*X2*Y1SQ)
     +        + ATAN2(Z1*Y2*(X2*BR12-X1*BR22),
     +             Z1*Z1*BR22*BR12+X1*X2*Y2SQ)
        S1 = S1 - Z1*E1 + CPHI*(Y1*B1+Y2*B2)
      ENDIF
      GOTO 20
    ENDIF
    RR = X21*X21 + Z21*Z21
    RR2 = SQRT(RR)
    CPHI = X21/RR2
    SPHI = Z21/RR2
    ZN = -CPHI
    U1 = X1*CPHI + Z1*SPHI
    U2 = X2*CPHI + Z2*SPHI
    WX = Z1*CPHI - X1*SPHI
    R1SQ = U1*U1 + WX*WX
    R2SQ = U2*U2 + WX*WX
    BR11 = SQRT(R1SQ+Y1SQ)
    BR21 = SQRT(R2SQ+Y1SQ)
    BR12 = SQRT(R1SQ+Y2SQ)
    BR22 = SQRT(R2SQ+Y2SQ)
    A = (X1*Z2-Z1*X2)/RR
    B1 = ALOG((U2+BR21)/(U1+BR11))
    B2 = ALOG((U2+BR22)/(U1+BR12))
    D1 = ALOG((R2SQ*(Y1+BR11)*(Y2+BR12))
     +         /(R1SQ*(Y1+BR21)*(Y2+BR22)))
    E1 = ATAN2(WX*Y1*(U2*BR11-U1*BR21),
     +          WX*WX*BR21*BR11+U1*U2*Y1SQ)
     +     + ATAN2(WX*Y2*(U2*BR12-U1*BR22),
     +          WX*WX*BR22*BR12+U1*U2*Y2SQ)
    S1 = S1 + A*(Z21*D1+X21*E1) - ZN*(Y1*B1+Y2*B2)
20   X1 = X2
    Z1 = Z2
30  CONTINUE
   GC(M) = GRT*S1
   DG(M) = GO(M) - GC(M)
40 CONTINUE
```

Appendix A2.2

```
      RETURN
      END

C -------------------------------------------------------------
      SUBROUTINE HEADER(NF,CPROG,CTYPE)
C -------------------------------------------------------------
C  Routine prints program header, opens input file.
C
      CHARACTER*20 CFILE
      CHARACTER*7 CPROG
      CHARACTER*8 CTYPE

      WRITE(6,901) CPROG, CTYPE
      READ(5,902) CFILE
      OPEN(NF,NAME=CFILE,TYPE='OLD')

  901 FORMAT(//8X,'+',22('-'),'+'/8X,'|',3X,'PROGRAM: ',A7,3X,'|'
     +       /8X,'|',2X,'2-D/2.5-D ',A8,2X,
     +       '|'/8X,'|',2X,'INVERSION PROGRAM',3X,'|'/8X,'+',22('-'),
     +       '+'//2X,'Enter name of input data file: ')
  902 FORMAT(A20)
      RETURN
      END

C -------------------------------------------------------------
      SUBROUTINE READER(NF,NS,EP,DEL,MAX,IOPT,IFG,N,GO,C,Y,P)
C -------------------------------------------------------------
C  Routine reads observed data, convergence criteria, and starting model
C    parameters from an input file.
C
      INTEGER NF, N, IOPT
      REAL GO(N), C(N), Y(N), P(4)

      READ(NF,901) NS, EP, DEL, MAX, IOPT, IFG
      WRITE(6,901) NS, EP, DEL, MAX, IOPT, IFG
      DO 10 I=1,N
        READ(NF,902) GO(I), C(I), Y(I)
        WRITE(6,902) GO(I), C(I), Y(I)
   10 CONTINUE
      IF (IOPT.EQ.2) THEN
        READ(NF,902) (P(I),I=1,4)
        WRITE(6,902) (P(I),I=1,4)
      ENDIF

  901 FORMAT(I5,2F10.5,3I5)
  902 FORMAT(8F10.3)
      RETURN
      END

C -------------------------------------------------------------
      SUBROUTINE CHOOSE(II)
C -------------------------------------------------------------
```

Appendix A2.2

```
C  Subroutine allows interactive choice between 2-D and 2.5-D inversion schemes.
C
      WRITE(6,901)
      READ(5,*) II

  901 FORMAT(X/' Indicate whether a 2-D (1) or 2.5-D (2) inversion',
     +         ' is desired (0 to quit). ')
      RETURN
      END

C -------------------------------------------------------------
      SUBROUTINE RITE(N,X,Z,RHO)
C -------------------------------------------------------------
C  Routine echos the input parameters.
C
      REAL X(N), Z(N), RHO
      WRITE(6,901)
      WRITE(6,902) 1, RHO
      DO 10 I=1,N
        WRITE(6,903) 1, I, X(I), Z(I)
   10 CONTINUE

  901 FORMAT(2X,'Parameters input:')
  902 FORMAT(X/2X,'Block number',I5,' of Density Contrast',F7.3,
     +       ' gm/cm3.'/4X,'Coordinates',6X,'X(L,I)',5X,'Z(L,I)')
  903 FORMAT(4X,2I4,4X,4(2X,F9.3))
      RETURN
      END

C -------------------------------------------------------------
      SUBROUTINE RITE1(NF,IER,INFER,NW,WK,N,DG)
C -------------------------------------------------------------
C  Routine outputs convergence criteria, error code parameters and values of
C    the minimized functional DG(*) at program termination.
C
      REAL WK(NW), DG(N)
      WRITE(NF,901) INFER, IER
      WRITE(NF,902) (WK(I),I=1,NW)
      WRITE(NF,*) ' DG(I) = ', (DG(I),I=1,N)

  901 FORMAT(' INFER = ',I1,';  IER = ',I3)
  902 FORMAT(' WORK(I) = ',F10.6,F7.0,F10.6,F10.5,F7.0)
      RETURN
      END

C -------------------------------------------------------------
      SUBROUTINE RITE3(N,NS,IFG,NF1,NF2,GO,C,GC,Y,RHO,X,Z,ZZ,ZT)
C -------------------------------------------------------------
C  Routine outputs parameters of the inverted body at termination in a form
C    suited for subsequent plotting.
C
      REAL GO(N), C(N), GC(N), Y(N), X(NS), Z(NS), ZZ(NS)
```

Appendix A2.2

```
      WRITE(NF2,901) N, 1+IFG
      DO 10 M=1,N
        WRITE(NF2,902) GO(M), C(M), GC(M), Y(M)
   10 CONTINUE
      WRITE(NF2,903) RHO, NS
      DO 20 I=1,NS
        WRITE(NF2,902) X(I), Z(I)
   20 CONTINUE
      WRITE(NF2,903) RHO, NS
      DO 30 I=1,NS
        WRITE(NF2,902) X(I), ZZ(I)
   30 CONTINUE
      IF (IFG.EQ.1) THEN
        READ(NF1,901) NN
        WRITE(NF2,903) RHO, NN
        DO 40 I=1,NN
          READ(NF1,902) X(I), Z(I)
          WRITE(NF2,902) X(I), Z(I)
   40   CONTINUE
      ENDIF

  901 FORMAT(2I5)
  902 FORMAT(8F10.3)
  903 FORMAT(F10.3,I5)
      RETURN
      END
```

Appendix B1

Appendix B1.1

Magnetic Filter

Aeromagnetic data for onshore regions were digitized on a 0.8 km (0.5 mi) square grid centered on the basal latitudes and central meridians of Geological Survey of Canada contoured data mapsheets. Data were then filtered by application of a $\frac{1}{r}$ distance weighted filter at the same grid interval, r, defining the distance from the central grid point in grid interval units. A 5×5 grid was used in filtering the data, giving an effective filter width of 4.0 km. Elements of the 25 point grid are listed below:

$$\begin{bmatrix} \frac{1}{4\sqrt{2}} & \frac{1}{2\sqrt{5}} & \frac{1}{4} & \frac{1}{2\sqrt{5}} & \frac{1}{4\sqrt{2}} \\ \frac{1}{2\sqrt{5}} & \frac{1}{2\sqrt{2}} & \frac{1}{2} & \frac{1}{2\sqrt{2}} & \frac{1}{2\sqrt{5}} \\ \frac{1}{4} & \frac{1}{2} & 1 & \frac{1}{2} & \frac{1}{4} \\ \frac{1}{2\sqrt{5}} & \frac{1}{2\sqrt{2}} & \frac{1}{2} & \frac{1}{2\sqrt{2}} & \frac{1}{2\sqrt{5}} \\ \frac{1}{4\sqrt{2}} & \frac{1}{2\sqrt{5}} & \frac{1}{4} & \frac{1}{2\sqrt{5}} & \frac{1}{4\sqrt{2}} \end{bmatrix}$$

Appendix B.2

The following describes the method adapted from Mittal (1984) and employed to adjust traverses of sea magnetometer data for offsets observed at points of intersection. The data made available by Bedford Institute were previously uncorrected for diurnal variations or for cross-over offsets.

Interpolated values, m_i, may be found from digital values along traverse at points of intersection, and offset magnitudes obtained as

$$\Delta m_{ij} = m_i - m_j \qquad \text{(B2.1)}$$

where Δm_{ij} is the offset at the intersection of the ith with the jth lines. Mittal (1984) describes a weighting scheme based on the inverse of the sum of squared offsets observed along each line:

$$W_i = \frac{K_i}{\sum_{l=1}^{K_i} [\Delta m_i^{(l)}]^2} \tag{B2.2}$$

where W_i is the unnormallized weighting for line i, and K_i is the number of intersections along line i. Weights may be normallized to values (W_i^*) near unity by

$$W_i^* = W_i \frac{N}{\sum_{i=1}^{N} W_i} \tag{B2.3}$$

where N is the total number of intersecting traverse lines.

Adjusted values at points of intersection may be calculated as

$$m_{ij} = \frac{m_i W_i^* + m_j W_j^*}{W_i^* + W_j^*}, \tag{B2.4}$$

from which the correction to line i at the cross-over with line j, C_{ij}, is then defined as

$$C_{ij} = \frac{\Delta m_{ij} W_j^*}{W_i^* + W_j^*}. \tag{B2.5}$$

The method eliminates all offsets existing between intersecting lines.

The above correction method does not discriminate between traverses showing constant levels of offset at intersections from those having offsets which alternate in sign. In the Bedford data, several east-west traverses show a constant level of offset, while north-south oriented tie lines tend to have alternating offset values as lines surveyed in opposite directions and at varying times are intersected. For the present study, the weighting of Equation (B2.2) was changed to one proportional to the inverse sum of absolute offsets, rather than that proportional to the inverse sum of squared offsets, for correction:

$$W_i = \frac{K_i}{\sum_{l=1}^{K_i} \sqrt{[\Delta m_i^{(l)}]^2}}. \qquad \text{(B2.6)}$$

Equation (B2.6) awards highest weighting to lines having total offsets near zero. The modified method was used successfully in the present study, but problems are foreseeable in the event that the denominator of Equation (B2.6) approached zero for a particular survey line. An alternative method might employ a weighting based on the magnitude of the sum of signed squares of offsets.

Discrete points were corrected along each line by applying a linear distance-weighted interpolation or correction gradient between correction values evaluated at points of intersection and as constant offset levels beyond points of intersection to either end of profile. The final data presentation on Figure 3.2 was produced after iterations of the sequence:

- visual inspection of intermediate maps;
- generation of ficticious tie line offsets (Haworth, 1974) along the western data boundary;
- correction of the longer and untied traverses.

The above method of correction should serve to remove much of any remaining diurnal variation, assuming that such variation is randomly expressed in the data and varies about a zero level over the period of measurement. Excellent positional control (Haworth and Watts, 1974) and generally low magnetic gradients in the Gulf of St. Lawrence region combine to allow offsets to be accurately determined.

Appendix B-3

Correction offsets for the Spector (1969) data were evaluated relative to respective GSC. aeromagnetic data values at selected UTM coordinates along the coastline of St. George's Bay. Offsets magnitudes were subsequently fitted to a least-squares planar surface having the form:

$$Correction = C_0 + C_1 \cdot (X - X_0) + C_2 \cdot (Y - Y_0) \qquad \text{(B3.1)}$$

where: X, Y are the UTM easting and northing of the point requiring correction

X_0, Y_0 is the UTM position central to the data

C_i, $i = 0,2$ are the coefficients of a first order least-squares fit.

Values of correction coefficients to be applied to the Spector dataset are:

X_0, Y_0 = 363.E, 5356.N
C_0 = 162.113 nT
C_1 = 4.41116 nT/km
C_2 = -6.38439 nT/km

Appendix C

This Appendix contains line drawing interpretations of reflection seismic sections from St. George's Bay (Mobil 1971, 1973) with Bouguer anomaly profiles added for ease of comparison. See Figure 3.4 for line locations. It is noted that the Bouguer anomaly values within 5 km of the seismic lines oriented parallel to the subbasin axis exhibit scattering about the profile extracted from contoured anomaly data. This local discrepency is a function of the local variability in the gravity field and the proximity of individual gravity stations to the seismic lines. Figure labelling and structural interpretation are discussed in the text body.

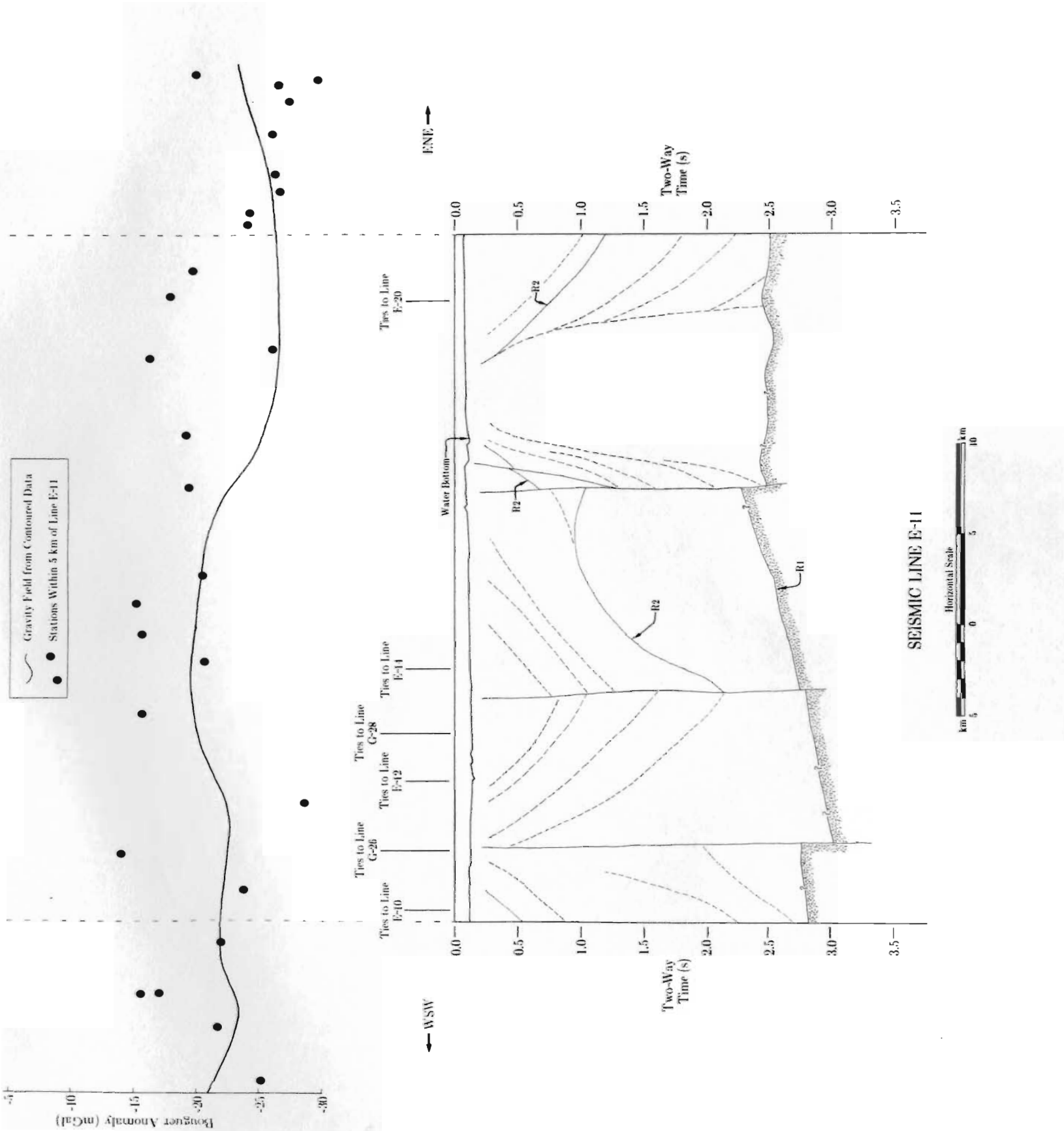

Figure C.1. Line drawing interpretation and gravity anomaly along seismic line E-11.

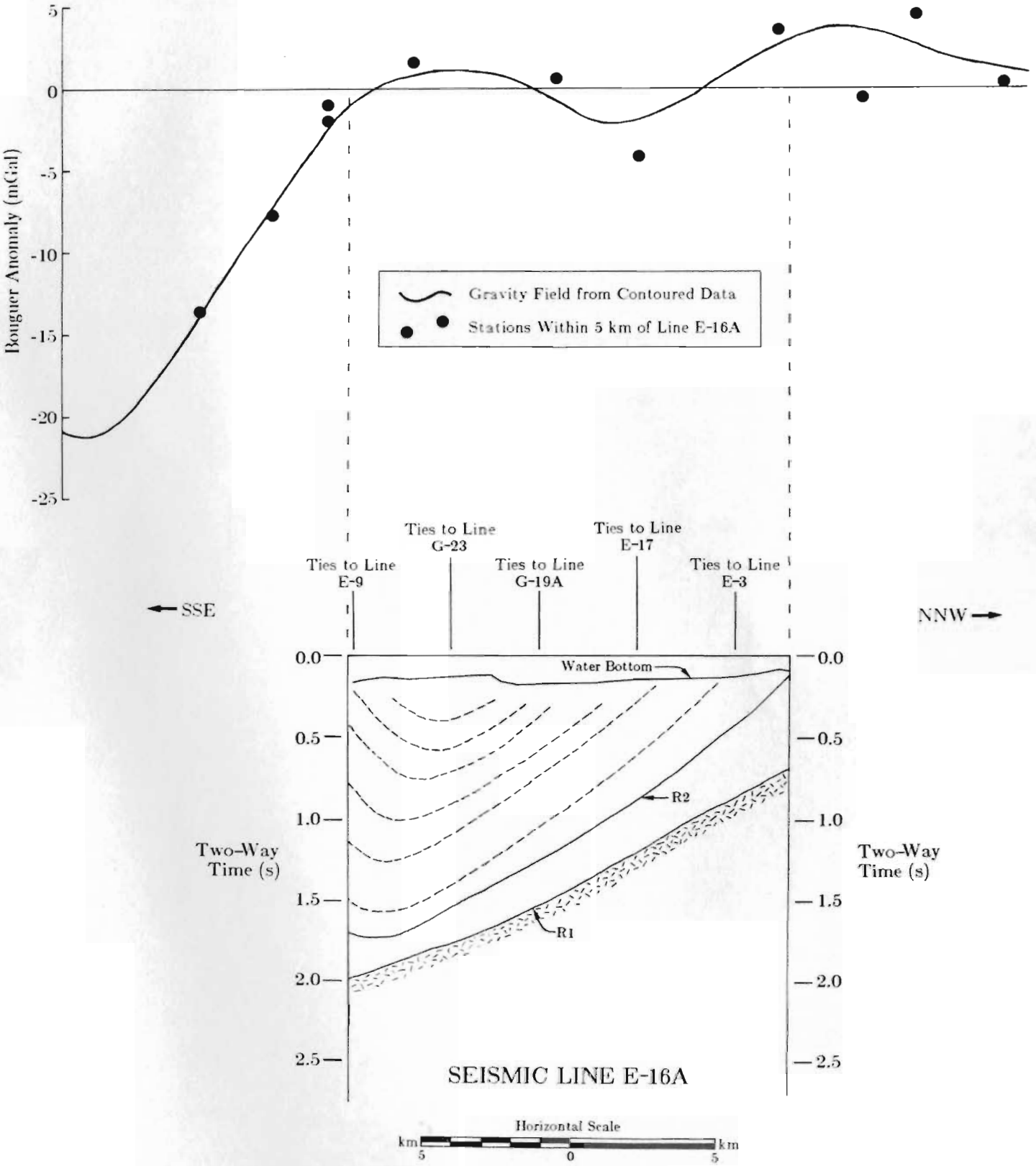

Figure C.2. Line drawing interpretation and gravity anomaly along seismic line E-16A.

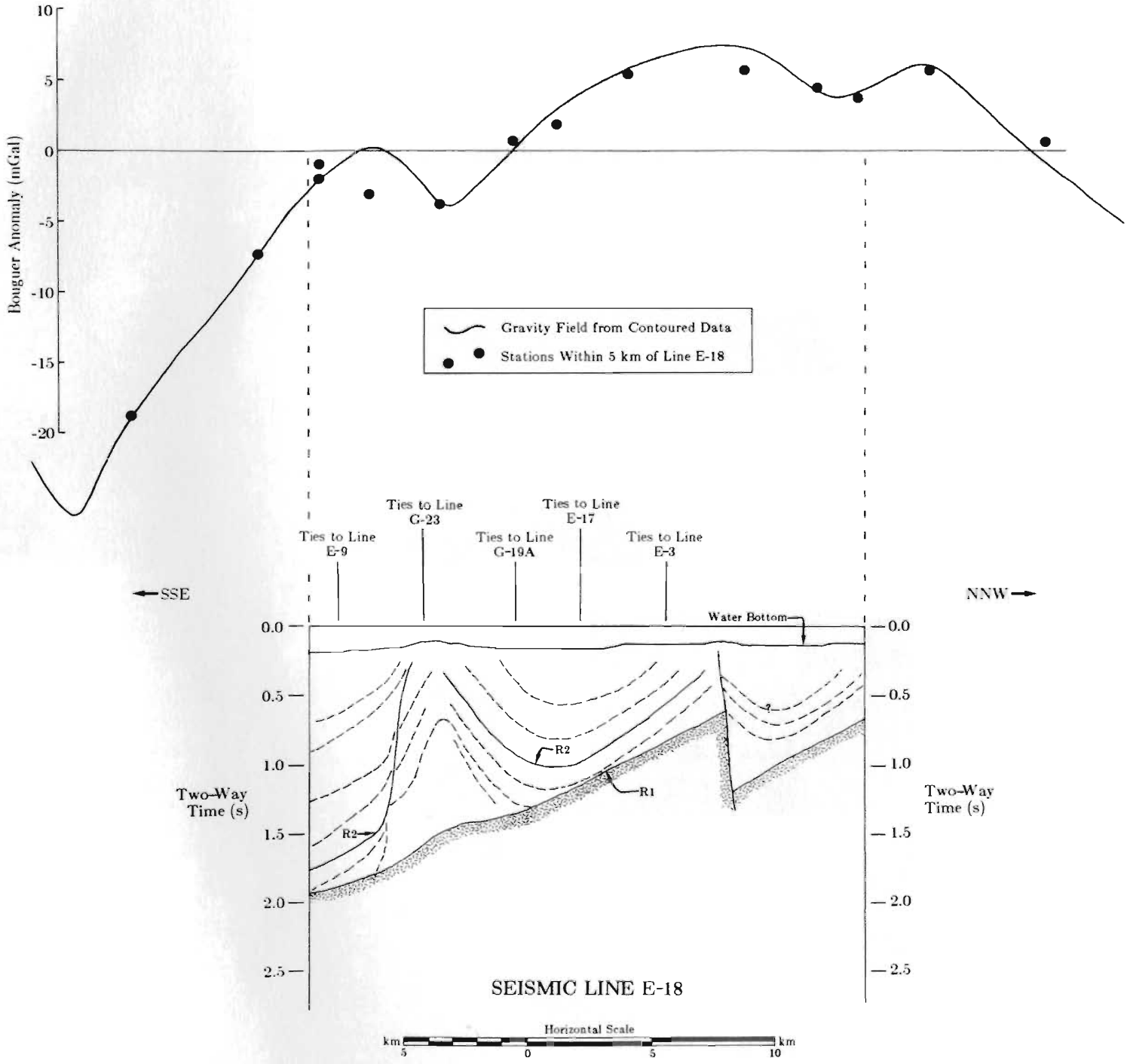

Figure C.3. Line drawing interpretation and gravity anomaly along seismic line E-18.

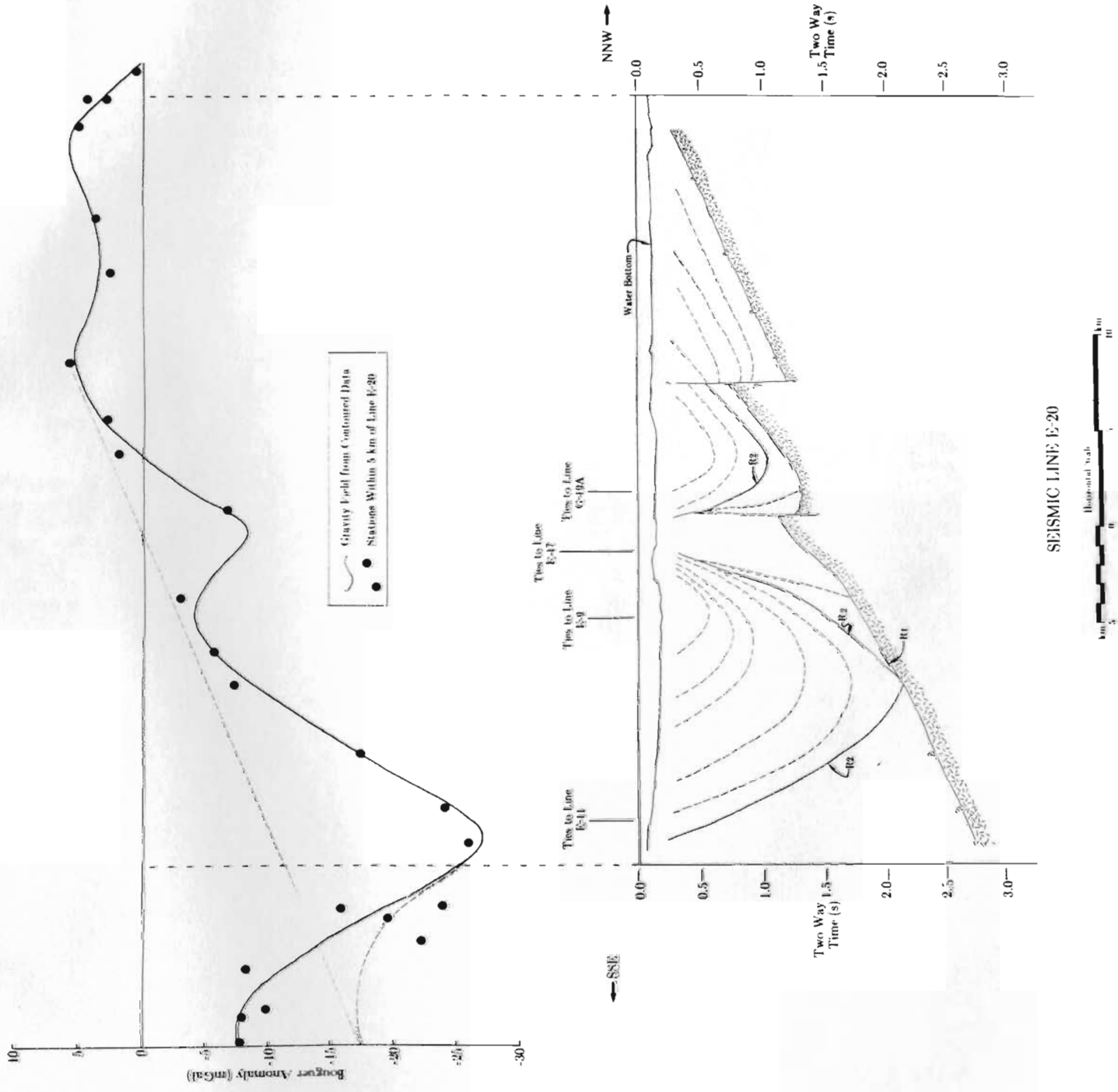

Figure C.4. Line drawing interpretation and gravity anomaly along seismic line E-20.

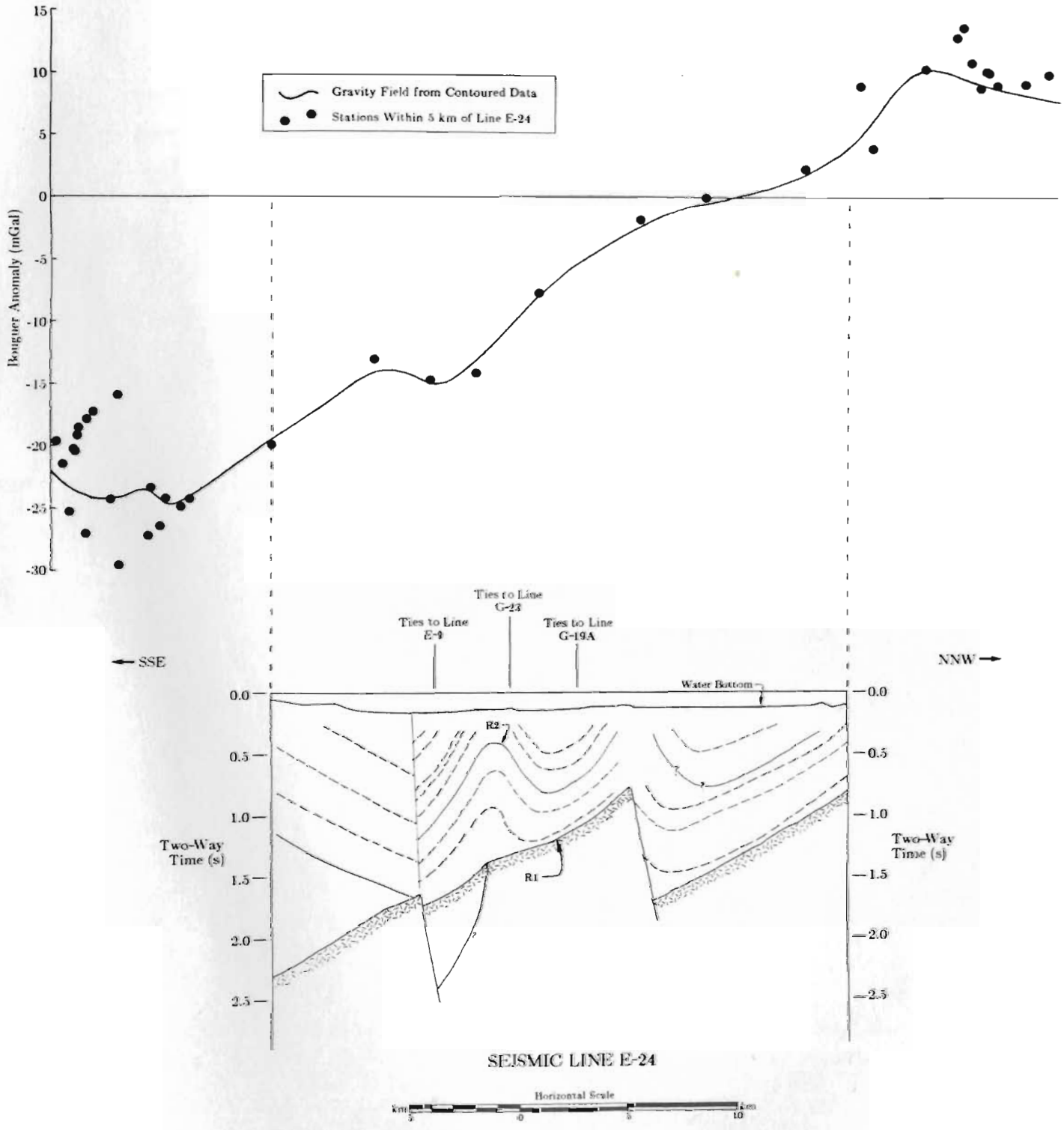

Figure C.5. Line drawing interpretation and gravity anomaly along seismic line E-24.

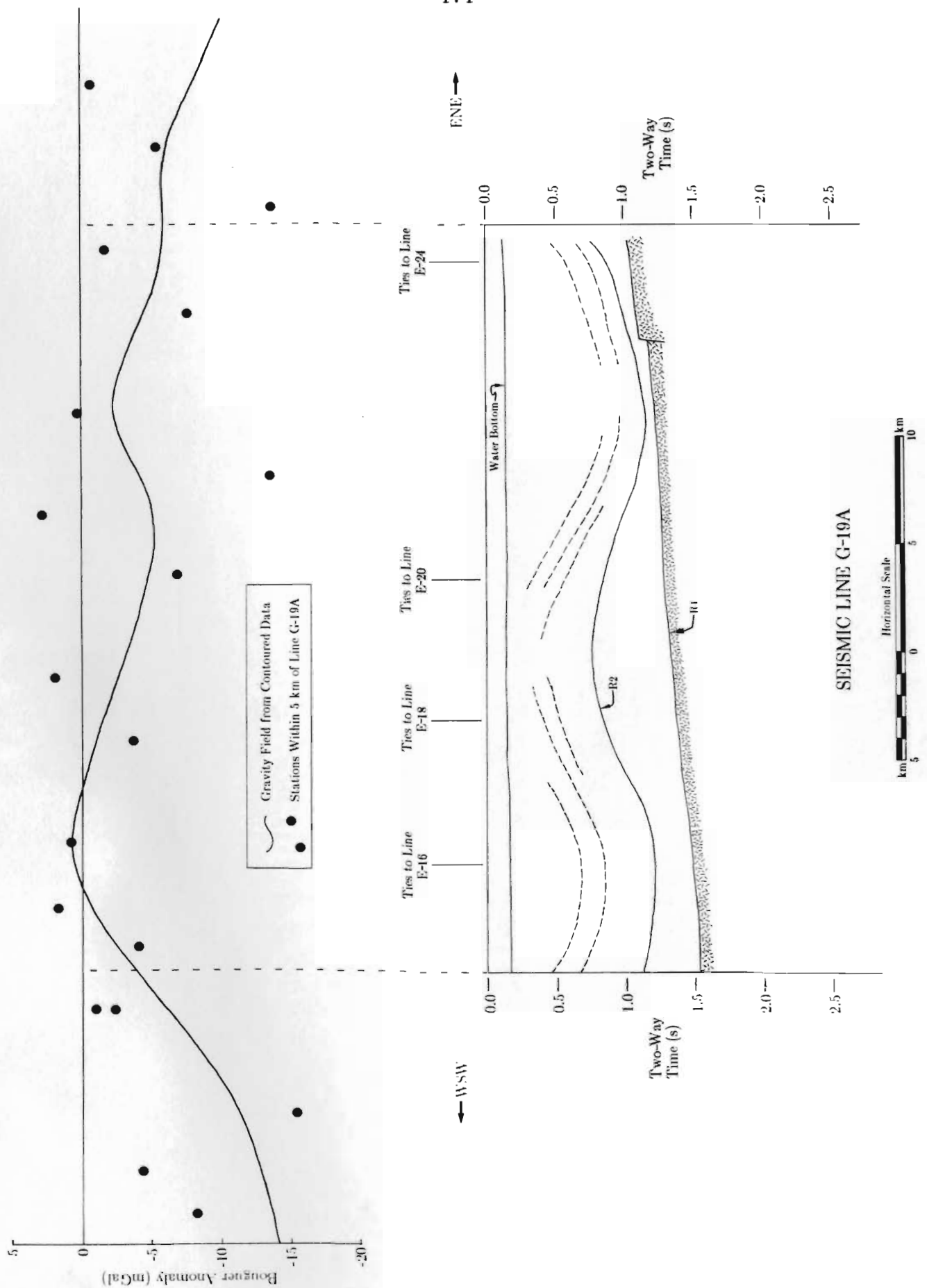

Figure C.6. Line drawing interpretation and gravity anomaly along seismic line G-19A.

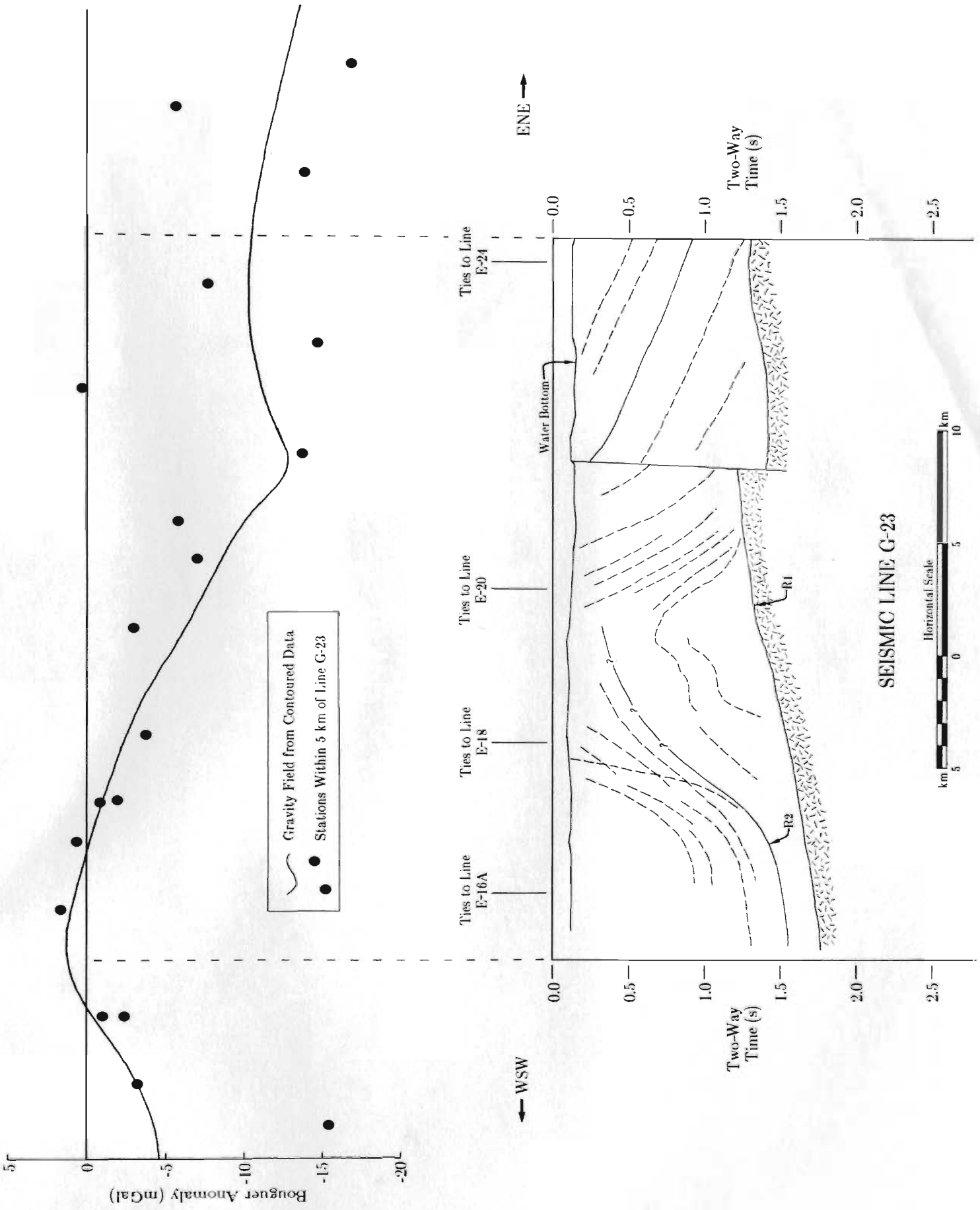

Figure C.7. Line drawing interpretation and gravity anomaly along seismic line G-23.